

# A new reference catalogue for the very metal-poor Universe: +150 OB stars in Sextans A

M. Lorenzo,<sup>1,2</sup>★ M. Garcia,<sup>1</sup> F. Najarro,<sup>1</sup> A. Herrero,<sup>3,4</sup> M. Cerviño,<sup>1</sup> N. Castro,<sup>5</sup>

<sup>1</sup>*Centro de Astrobiología (CAB), CSIC-INTA, Carretera de Ajalvir km 4, 28850 Torrejón de Ardoz, Madrid, Spain*

<sup>2</sup>*Departamento de Física Teórica, Universidad Autónoma de Madrid (UAM), Campus de Cantoblanco, E-28049 Madrid, Spain*

<sup>3</sup>*Instituto de Astrofísica de Canarias, La Laguna, Tenerife, Spain*

<sup>4</sup>*Departamento de Astrofísica, Universidad de La Laguna, Tenerife, Spain*

<sup>5</sup>*Leibniz-Institut für Astrophysik Potsdam (AIP), An der Sternwarte 16, 14482, Potsdam, Germany*

Accepted XXX. Received YYY; in original form ZZZ

## ABSTRACT

Local Group (LG) very metal-poor massive stars are the best proxy for the First Stars of the Universe and fundamental to modelling the evolution of early galaxies. These stars may follow new evolutionary pathways restricted to very low metallicities, such as chemically homogeneous evolution (CHE). However, given the great distance leap needed to reach very metal-poor galaxies of the LG and vicinity, no comprehensive spectroscopic studies have been carried out at metallicities lower than the Small Magellanic Cloud (SMC,  $Z = 1/5 Z_{\odot}$ ) until now. After five observing campaigns at the 10.4-m Gran Telescopio Canarias, we have assembled a low-resolution ( $R \sim 1000$ ) spectroscopic collection of more than 150 OB stars in the  $1/10 Z_{\odot}$  galaxy Sextans A, increasing by an order of magnitude the number of massive stars known in this galaxy. The catalogue includes 38 BA-type supergiants, 4 red supergiants, and the first candidate  $1/10 Z_{\odot}$  binary systems, CHE sources and systems hosting stripped stars. The sample massive stars mainly overlap the higher concentrations of neutral gas of Sextans A. However, we find some sources in low H I column-density regions. The colour-magnitude diagram of the galaxy presents large dispersion, which suggests uneven, internal extinction in Sextans A. This is the largest catalogue of OB-type stars ever produced at sub-SMC metallicities. This sample constitutes a fundamental first step to unveiling the evolutionary pathways and fates of very metal-poor massive stars, analyzing the dependence of radiation-driven winds with metallicity, and studying binary systems in an environment analogue to the early Universe.

**Key words:** stars: massive – stars: early-type – stars: Population III – galaxies: stellar content – galaxies: individual: Sextans A

## 1 INTRODUCTION

Massive stars ( $M > 8 M_{\odot}$ ) are powerful drivers of galaxy evolution. Their stellar winds, supernova explosions and mighty production of ionizing radiation stir and impact the surrounding interstellar medium to such an extent that they dominate the integrated light of star-forming regions. Massive star properties and spectra are thus essential to interpret evidence from galaxies at all redshifts, while they are also pivotal ingredients to model the chemodynamical evolution of galaxies with time.

Yet, very little is known about the evolution of very metal-poor massive stars ( $Z \leq 1/10 Z_{\odot}$ ), key to interpreting the processes and events of the early epochs of the Universe. The increasing number of open questions in the field is demanding a large census of resolved massive stars in environments with very low metallicity. Such a sample can be used, after quantitative spectroscopic analysis, to study galaxies at the peak of the cosmic star formation ( $z \sim 2$ , Madau & Dickinson 2014) or earlier. Among these questions are the evolutionary pathways of massive stars at metallicities lower than the Small Magellanic Cloud (Groh et al. 2019; Szécsi et al. 2022),

the incidence of chemically homogeneous evolution (CHE, Szécsi et al. 2015), CHE stars as possible ionizing sources of the extreme He II 4686 nebular lines detected in some very metal-poor galaxies (Kehrig et al. 2015; Sobral et al. 2019; Wofford et al. 2021), and the relative role of radiation driven winds and binary mass exchange in shaping the evolution of very metal-poor massive stars (Shenar et al. 2020). In addition, the evolutionary channels that lead to  $\sim 30 M_{\odot}$  stellar-size black holes are also most likely related to the extremely low metallicity regimes (Mandel & de Mink 2016; Marchant et al. 2016; van Son et al. 2020).

The spectroscopic studies of very metal-poor massive stars are greatly hampered by sensitivity issues. For decades, the Small Magellanic Cloud (SMC,  $Z = 1/5 Z_{\odot}$ ) has represented both a metallicity and a distance frontier since metal-poorer environments are usually found in galaxies at the outer rims of the Local Group (García et al. 2021). This situation is about to change with the advent of the Extremely Large Telescope (ELT) and its multi-object spectrographs HARMONI (Thatte et al. 2016, 2020) and MOSAIC (Hammer et al. 2014; Evans et al. 2015). They will enable exquisite quantitative spectroscopic analyses of extragalactic massive stars that so far have been reserved to the Magellanic Clouds (e.g. Mokiem et al. 2007; Ramírez-Agudelo et al. 2017; Sabín-Sanjulián et al. 2017). However,

★ E-mail: mlorenzo@cab.inta-csic.es

the design of both instruments hinders their use as discoverers of massive stars in nearby very metal-poor galaxies. The typical diameter of these galaxies is a few arcminutes, while the field of view of HAR-MONI is very limited ( $9'' \times 6''$  at most) and MOSAIC's spacing of the robot positioners is too broad ( $23''$  diameter). As a consequence, the construction of catalogues of very metal-poor massive stars is still restricted to contemporary observing facilities.

In this work, we present the first major effort to mine the population of massive stars in the galaxy Sextans A ( $10^{\text{h}}11^{\text{m}}00.^{\text{s}}8 - 04^{\circ}41'34''$ , dIrr, *aka* DDO 75, McConnachie 2012). Located in the outer edge of the Local Group (LG), 1.34 Mpc away, and presenting low foreground extinction ( $E(B - V)_{\text{fg}} = 0.044$ , Tammann et al. 2011), Sextans A is a contender to become the next benchmark for low metallicity regimes. Its oxygen abundance derived from H II regions ranges  $12 + \log(\text{O}/\text{H}) = 7.49\text{--}7.71$  ( $1/15\text{--}1/10 \text{ O}_{\odot}$ , Skillman et al. 1989; Pilyugin 2001; Kniazev et al. 2005; Berg et al. 2012) and the analysis of blue supergiant revealed the lowest abundance of Fe-group elements in the LG ( $[(\text{Fe II}, \text{Cr II})/\text{H}] = -0.99 \pm 0.06$ , Kaufer et al. 2004, K04). Its poor Fe content has been confirmed by Garcia et al. (2017) with HST-COS spectroscopy of a selection of O stars. In addition, Kaufer et al. (2004) found that the  $[\alpha/\text{Fe}]$  abundance ratio of Sextans A is consistent with the solar ratio.

With such promising low values for metallicity, this galaxy has sparked the interest of the community. Camacho et al. (2016, C16) were the first to confirm the presence of OB-type stars in Sextans A. Garcia et al. (2019, G19) reported four young O stars on its outskirts, signalling massive star formation in low-density environments. In addition, Britavskiy et al. (2014, 2015) unveiled the first red supergiants in the galaxy with optical spectroscopy of *Spitzer*/IRAC candidates. Nevertheless, these works provide a deficient coverage of the most prominent star-forming regions of Sextans A.

In this work, we present the results of four new observing campaigns at the 10.4-m Gran Telescopio Canarias (GTC) designed to cover all the UV bright sources of the galaxy and the massive stellar content of its H II shells. Together with the sources from our first observing run (Camacho et al. 2016), the resulting sample will yield first-order information on the evolution of massive stars with sub-SMC metallicity and provide an extensive collection of spectra to characterise the physical properties of massive star populations at these low- $Z$  regimes.

The paper is structured as follows. The spectroscopic observations and adopted target selection criteria are presented in Sect. 2. In Sect. 3, we describe the data reduction process. The spectral classification, membership assessment and radial velocity measurement are described in Sect. 4, along with an evaluation of the  $Q$  pseudo-colour as a photometric method to select OB candidates. In Sect. 5, we offer an overview of the entire sample and discuss the colour-magnitude diagram of Sextans A, exploring the implications for its recent star formation history and stellar evolution at very low metallicity regimes. Finally, a summary and general conclusions are provided in Sect. 6.

## 2 DESCRIPTION OF OBSERVATIONS

Observations consisted of two mask multi-object spectroscopy (MOS) observing runs, GTC3-14AGOS (MOS1, PI A. Herrero) and GTC118-17B (MOS2, PI M. Garcia), and two long-slit (LSS) observations, GTC43-19B (LSS2, PI M. Garcia) and GTC58-20B (LSS3, PI M. Lorenzo). All of them were obtained with the Optical System for Imaging and low-Intermediate-Resolution Integrated Spectroscopy (OSIRIS) installed at the 10.4-m Gran Telescopio Canarias

(GTC). Our data were complemented with long-slit spectroscopy published in Camacho et al. (2016), denoted as LSS1. The observing logs are provided in Appendix A.

The MOS1 programme consisted of 13 hours of dark and grey sky and seeing lower than  $1.2''$ . It was broken into one-hour-long observing blocks distributed in 2014 and 2015, and taken in service mode (see Table A1). In this data set, targets were selected from Massey et al. (2007)'s photometric catalogue, with  $19.0 \leq V \leq 21.0$  and a reddening-free pseudo-colour  $Q = (U - B) - 0.72(B - V) \leq -0.8$  (see Section 4.4), following the criteria described in Garcia & Herrero (2013) and Camacho et al. (2016). The observations of MOS2 consisted of 7 hours divided into two dark nights carried out in visitor mode (see Table A2). The primary targets of this proposal were UV sources from Bianchi et al. (2012) with  $m_{\text{F170W}} \leq 17.6$  (HST-WFPC2's filter F170W,  $\lambda_c = 1730 \text{ \AA}$ ) and without previous optical coverage. The long-slit LSS2 observations were designed to collect all the UV bright sources not covered by the MOS2 run. A total of 4 hours in 2020 *via* service mode was devoted to the run. Lastly, the LSS3 programme was granted 42 hours of dark sky in visitor mode to mine the population of massive stars in the giant H II shells of the southeast of the galaxy. However, due to bad weather conditions, only 26.2 hours were observed over the first semester of 2021. Targets with  $18.0 \leq V \leq 21.4$  and  $Q \leq -0.6$  were included.

Both the MOS and the LSS2 runs used the R2000B VPH filter,  $2 \times 2$  binning and  $1.2''$  slits, which granted a resolving power of  $R = \lambda/\Delta\lambda \sim 1000$  in the  $4000 - 5500 \text{ \AA}$  range. For MOS data sets, the exact wavelength coverage depends on the position of the slit in the mask. Some slits (5, 8 and 13 from MOS1, and 2, 20 and 24 from MOS2) were tilted ( $80^\circ$ ,  $49^\circ$ ,  $-25^\circ$ ,  $5^\circ$ ,  $7.1^\circ$  and  $8^\circ$  from the North-South axis, respectively) in order to accommodate a larger amount of stars in the sample. This inclination decreased the spatial and spectral resolution of their corresponding spectra. Observing run LSS3 was carried out in remote-visitor mode, and different slit widths could be used to match the seeing conditions, ranging from  $0.8''$  to  $1.5''$ . This resulted in different spectral resolutions within the sample. Both the tilt and the width of the slits are noted for the corresponding stars in Tables 1-3.

## 3 DATA REDUCTION

The MOS and the LSS data sets were reduced using different procedures. For the long-slit observations, we followed the routine described in Garcia & Herrero (2013). The reduction of the two MOS data sets was carried out using the *gtcmos* package, an IRAF<sup>1</sup> pipeline developed by Dr. Divakara Mayya to reduce OSIRIS-MOS spectra (Gómez-González et al. 2016). The pipeline delivers a 2D wavelength calibrated image where we applied IRAF's *apall* task to extract the spectra and perform background subtraction. Finally, we used our own IDL routines to perform heliocentric correction, align the spectra in velocity space, coadd the selected observing blocks, and generate the final spectrum. The spectra were then normalized with IRAF's *continuum* task. Further details on relevant aspects of the reduction steps are given below.

In order to maximise the final quality of the spectra obtained with MOS observations and to define a reduction protocol for future MOS runs, we tested three different approaches in the MOS1 run: (i) reducing the data sets obtained in each observing block (OB) individually;

<sup>1</sup> IRAF is distributed by the National Optical Astronomy Observatory, operated by the Association of Universities for Research in Astronomy (AURA) under agreement with the National Science Foundation.

(ii) creating super-observing blocks (sOB), i.e. combining exposures that were carried out the same night and shared the calibration images (sOB03 = OB03 + OB04 and sOB13 = OB12 + OB13 + OB14); and (iii) coadding all raw images prior to reduction. The latter idea was dismissed due to the spatial shift between the location of the stars in the data sets of OBs taken in different years, hence coadding all data would result in severely decreased spatial resolution. A similar shift between OBs can be detected within the same night if the mask is not frequently re-aligned. In Table A5, we list the OBs and sOBs used to generate the final spectrum of each star observed in MOS1. We find that both procedures return very similar results, although reducing the spectra individually prior to coaddition provided slightly better results for most of the stars. For the MOS2 data set, we coadded all exposures of Night-1 and Night-2 separately.

We did not apply Flat Field correction to MOS runs since the corresponding *gTCMOS* routine would only offer a solution in the common wavelength intervals covered by all the slits of a given MOS data set. Hence its implementation would lead to losing the extremes of the spectral range. Our tests showed little signal-to-noise ratio (S/N) improvement if the Flat Field correction was applied.

For the reduction of all the observing runs, sky subtraction was carried out at the step of *apall* spectral extraction. In this step, we tried to minimize the nebular contribution in the extracted stellar spectrum to avoid compromising the spectral classification. To this end, we estimated the background level from regions as close as possible to the source. This method was preferred since it preserves spatial information of the nebular emission at the vicinity of the stars. Yet, nebular subtraction is not always complete as evinced by the presence of  $H\beta$  and  $[O\ III]$  lines in emission in the final spectra of the sample stars (Figs. B1-B26). In other cases, the nebular contribution is overcorrected, and the spectra show these lines in absorption, or in some rare occasions,  $H\beta$  in strong absorption and  $[O\ III]$  in emission. We note that it is not possible to perform a complete correction of the nebular emission since it would require to model the variation of the nebular emissivity along the slit in each case. Moreover, the spatial resolution of our observations is likely insufficient to adequately sample the ionization structure of the  $H\ II$  shells, which translates into an incomplete nebular subtraction. During the reduction of the long-slit runs, we tried to improve the sky subtraction by selecting the sky boxes at different distances from the targets at *apall*, but the results were again unsatisfactory.

In MOS observations, we detected dark columns on the right part of some slits after applying the *gTCMOS omreduce* task. *Omreduce* trims the portions of the image corresponding to individual slits, applies the wavelength calibration and finally returns a reconstructed MOS image with the slits aligned in wavelength. The dark columns arise when the slits are too close to each other and the extraction regions assigned by the pipeline overlap. The overlap can sometimes create an artificial emission that may be mistaken for a stellar source. At the step of *apall* extraction, we selected the stellar apertures and defined their sky boxes avoiding these artefacts. A future recommendation to prevent this issue is designing the MOS masks with enough space between slits. We recommend leaving a projected distance larger than  $5''$  in the horizontal direction if *gTCMOS* will be used for reduction. We also suggest using slits with a length seven times greater than the expected seeing in the observations to allow a proper selection of the sky boxes during sky subtraction.

Once the data of all individual observing blocks or super-observing blocks had been reduced and extracted with *apall*, all the spectra extracted for a given star were co-added with a semi-automatic IDL script. This script sets the spectra to the heliocentric standard of rest

and combines the exposures weighing by their standard deviation. Observing blocks with too poor spectral quality were discarded.

Some stars were observed in more than one programme and even more than once within an LSS programme. To improve the S/N of the data, we combined the observations after matching their spectral resolution and correcting for radial velocity variations when necessary. Those stars suffering from radial velocity shifts between exposures are marked in Tables 1-3 as "SB1", as they suggest a possible binary nature.

The final reduced spectra are shown in Figs. B1-B26 in Appendix B, arranged by spectral type. Identification numbers, coordinates and photometric measurements are collected in Tables 1-3, along with the spectral types and radial velocities derived in this work.

## 4 ANALYSIS

### 4.1 Spectral classification

The spectral classification of the OB-type stars was carried out following the criteria outlined in Castro et al. (2008) for metal-poor regimes ( $Z \sim 0.5 Z_{\odot}$ ), adapted to the metallicity of Sextans A by Camacho (2017). We also used the guidelines given by Sota et al. (2011) for late O-types and the ones from Walborn et al. (2002) for stars earlier than O5. The main diagnostics for O stars are based on the relative intensity of  $He\ I$  and  $He\ II$  lines. The luminosity class of O-type stars was assigned based on the width of the Balmer lines and on whether the  $He\ II\ 4686$  line was in absorption or emission. We note the latter diagnostic may be affected by the weak winds of the targets. The spectral types of B stars are indicated by the presence and strength of Si transitions in different ionization stages,  $Mg\ II\ 4481$  and  $He\ I$  lines. Their luminosity class was assigned from the width of the Balmer lines.

We also used the absolute magnitude  $M_V$  as an additional indicator of luminosity class for some sources. We estimated  $M_V$  using the distance modulus of the galaxy ( $\mu_0 = 25.63$ , Tammann et al. 2011) and the intrinsic colour  $(B - V)_0$  calculated from the pseudo-colour  $Q$  ( $(B - V)_0 = -0.005 + 0.317Q$ , Massey et al. 2000).

Later spectral types (A-types and later) were classified following Gray & Corbally (2009). The spectral classification of these late stars may be affected by the low metallicity of the environment since metallic lines and molecular bands are the main diagnostics.

Spectral types are compiled in Tables 1-3. In addition, we provide brief notes on the spectral classification of targets in Appendix C.

**Table 1.** Blue type stars (from O to F types) confirmed by spectroscopy in this work. Identification codes (ID), spectral types (SpT), radial velocities ( $v_{\text{rad}}$ ) and signal-to-noise ratio per element of resolution (S/N, calculated in a region free of spectral lines around 4800 Å) are provided. Stars whose radial velocity was determined manually are marked with <sup>(\*)</sup>. Identification numbers, coordinates and photometry by Massey et al. (2007) are also included when available, otherwise we provide the ones from Bianchi et al. (2012)'s or Holtzman et al. (2006)'s catalogues, and mark the sources with <sup>(†)</sup> or <sup>(‡)</sup>, respectively. We include additional information in column *Notes*.

ID	Alt. ID	RA (J2000.0)	DEC (J2000.0)	SpT	V	B – V	Q	$v_{\text{rad}}$ (km s <sup>-1</sup> )	S/N	Notes
s001 <sup>‡</sup>	-	10:11:05.29	-04:42:41.7	O3.5 V	F555W = 21.851	-	-	460 ± 100	55	1.0'' slit. SB2?
s002	J101105.28-044238.3	10:11:05.28	-04:42:38.3	O4 Vz	20.369	-0.279	-0.937	275 ± 30	111	1.0'' slit.
s003*	J101058.59-044328.9	10:10:58.59	-04:43:28.9	O3-O5 Vz	20.804	-0.095	-1.120	425 ± 60	83	G19-s2
s004	J101057.89-044310.2	10:10:57.89	-04:43:10.2	O5 III	20.917	-0.277	-1.006	310 ± 30	91	G19-s4. Bin?
s005	J101053.95-044057.4	10:10:53.95	-04:40:57.4	O5 V((fc))	21.751	-0.364	-0.800	375 ± 40	30	0.8'' slit.
s006*	J101104.74-044206.1	10:11:04.74	-04:42:06.1	O6 I	20.721	-0.068	-0.416	500 ± 50	29	
s007	J101106.48-044237.1	10:11:06.48	-04:42:37.1	O6 V	20.515	-0.280	-0.965	395 ± 35	105	SB2?
s008*	J101106.65-044213.0	10:11:06.65	-04:42:13.0	O6.5 V	21.071	-0.199	-0.985	300 ± 50	71	1.2'' slit. Blend.
s009	J101108.48-044149.2	10:11:08.48	-04:41:49.2	O7 V	20.659	-0.285	-0.948	320 ± 35	66	
s010*	J101059.19-044308.2	10:10:59.19	-04:43:08.2	O7 V	21.003	-0.134	-0.549	250 ± 50	30	1.5'' slit.
s011	J101103.70-044234.2	10:11:03.70	-04:42:34.2	O7.5 III + B0 I	20.191	-0.220	-1.019	315 ± 30	80	1.0'' slit. Blend.
s012	J101054.23-044115.3	10:10:54.23	-04:41:15.3	O7.5 III	20.115	-0.181	-0.835	290 ± 155	52	SB2 or blend?
s013*	J101100.09-044336.0	10:11:00.09	-04:43:36.0	O7.5 III	21.532	-0.295	-0.914	370 ± 50	43	
s014	J101053.81-044113.0	10:10:53.81	-04:41:13.0	O7.5 III((f))	20.688	-0.265	-1.015	330 ± 35	49	C16-OB326. Off-slit.
s015*	J101105.47-044236.8	10:11:05.47	-04:42:36.8	O7.5 V + B?	22.259	-0.410	-1.010	225 ± 50	35	1.0'' slit. SB2?
s016	J101056.28-044253.0	10:10:56.28	-04:42:53.0	O8 II	20.639	-0.192	-1.065	285 ± 95	72	
s017*	J101106.50-044139.0	10:11:06.50	-04:41:39.0	O8 II	21.399	0.198	-1.281	330 ± 50	18	Off-slit.
s018*	J101053.61-044246.3	10:10:53.61	-04:42:46.3	O8 III	21.092	-0.321	-0.894	210 ± 50	41	
s019 <sup>†</sup>	3485	10:11:05.84	-04:42:12.3	O8 III	21.930	-0.250	-0.850	270 ± 35	32	0.8'' slit. Blend.
s020	J101107.33-044205.6	10:11:07.33	-04:42:05.6	O8 V	20.544	-0.196	-0.968	315 ± 35	125	1.5'' slit. SB2 or blend?
s021	J101104.79-044220.9	10:11:04.79	-04:42:20.9	O8 V	20.598	-0.468	-0.616	335 ± 35	95	0.63'' slit. Tilted 3°. Blend.
s022	J101105.38-044240.1	10:11:05.38	-04:42:40.1	O8 V	19.459	-0.259	-0.950	370 ± 30	95	C16-OB521. Blend.
s023	J101105.21-044240.5	10:11:05.21	-04:42:40.5	O8 V	20.288	-0.299	-0.927	235 ± 35	82	1.0'' slit.
s024	J101105.90-044210.3	10:11:05.90	-04:42:10.3	O8 V	20.810	-0.162	-1.044	280 ± 35	77	
s025	J101110.14-044129.7	10:11:10.14	-04:41:29.7	O8 V	21.060	-0.265	-0.976	350 ± 45	52	
s026 <sup>†</sup>	3935	10:11:07.43	-04:42:04.5	O8 V	22.500	-0.060	-1.007	325 ± 110	51	0.8'' slit. Blend.
s027 <sup>†</sup>	2398	10:11:03.39	-04:42:37.1	O8 V	21.960	-0.220	-0.852	280 ± 35	20	1.5'' slit.
s028	J101107.34-044231.7	10:11:07.34	-04:42:31.7	O8.5 III	20.568	-0.228	-1.033	300 ± 35	83	
s029	J101058.19-044318.4	10:10:58.19	-04:43:18.4	O8.5 III	20.803	-0.247	-1.005	285 ± 35	74	G19-s3. SB1.
s030	J101109.39-044055.5	10:11:09.39	-04:40:55.5	O8.5 III	21.008	-0.322	-0.848	380 ± 35	56	Tilted 7.1°.
s031*	J101057.33-044016.6	10:10:57.33	-04:40:16.6	O8.5 V	21.229	-0.181	-1.069	475 ± 50	115	Tilted 8°.
s032	J101109.35-044057.8	10:11:09.35	-04:40:57.8	O8.5 V	21.216	-0.326	-0.776	365 ± 30	67	Tilted 7.1°. Blend.
s033	J101105.64-044215.6	10:11:05.64	-04:42:15.6	O8.5 V	21.654	-0.271	-0.960	295 ± 75	40	0.8'' slit.
s034	J101058.05-044021.8	10:10:58.05	-04:40:21.8	O8.5 V	20.923	-0.168	-0.548	250 ± 30	26	1.5'' slit.
s035*	J101106.50-044212.4	10:11:06.50	-04:42:12.4	O8.5 V	20.683	-0.089	-0.498	170 ± 100	24	Blend.
s036	J101105.07-044214.6	10:11:05.07	-04:42:14.6	O9 I	19.738	-0.237	-0.931	360 ± 30	200	
s037	J101104.78-044224.1	10:11:04.78	-04:42:24.1	O9 I	20.681	-0.234	-1.001	345 ± 30	110	C16-OB623.
s038	J101106.05-044211.4	10:11:06.05	-04:42:11.4	O9 I((f))	19.492	-0.231	-1.013	450 ± 35	91	C16-OB523.
s039	J101059.96-044332.9	10:10:59.96	-04:43:32.9	O9 III	21.084	-0.171	-0.502	340 ± 35	49	1.0'' slit.
s040*	J101106.56-044217.1	10:11:06.56	-04:42:17.1	O9 III + mid-B?	21.285	-0.311	-0.900	250 ± 30	29	SB2?
s041	J101058.53-044414.4	10:10:58.53	-04:44:14.4	O9.5 II	20.877	-0.029	-1.071	290 ± 30	73	G19-s1
s042	J101105.44-044221.4	10:11:05.44	-04:42:21.4	O9.5 III	20.642	-0.226	-0.939	275 ± 30	108	Blend.

continued on next page



Table 1. continued.

ID	Alt. ID	RA (J2000.0)	DEC (J2000.0)	SpT	V	B - V	Q	$v_{\text{rad}}$ (km s <sup>-1</sup> )	S/N	Notes
s043	J101105.03-044224.8	10:11:05.03	-04:42:24.8	O9.5 V	20.863	0.250	-0.607	305 ± 30	92	1.5'' slit. Blend.
s044	J101110.45-044132.9	10:11:10.45	-04:41:32.9	O9.5 V	20.800	-0.255	-0.966	270 ± 95	60	SB2?
s045	J101105.93-044208.0	10:11:05.93	-04:42:08.0	O9.5 V	20.511	-0.169	-0.430	250 ± 35	60	0.8'' slit.
s046*	J101104.87-044216.0	10:11:04.87	-04:42:16.0	O9.5 V	20.748	-0.214	-0.872	325 ± 30	45	0.8'' slit. Blend.
s047	J101104.58-044213.0	10:11:04.58	-04:42:13.0	O9.5 V	20.668	0.267	-0.274	335 ± 100	31	C16-OB625.
s048* <sup>†</sup>	3691	10:11:06.34	-04:42:28.2	O9.5 Vn	22.180	-0.240	-0.797	200 ± 60	20	1.0'' slit.
s049	J101105.30-044210.1	10:11:05.30	-04:42:10.1	O9.7 I	19.976	-0.268	-0.929	350 ± 30	91	SB1? Blend.
s050	J101100.66-044044.3	10:11:00.66	-04:40:44.3	O9.7 I	19.609	-0.248	-0.960	295 ± 30	90	C16-OB321. 0.63'' slit.
s051	J101058.27-044230.6	10:10:58.27	-04:42:30.6	O9.7 I	20.774	-0.277	-0.875	335 ± 30	70	
s052	J101106.46-044207.3	10:11:06.46	-04:42:07.3	O9.7 I	20.320	-0.166	-0.690	345 ± 30	62	SB2?
s053*	J101106.13-044208.3	10:11:06.13	-04:42:08.3	O9.7 I	21.255	-0.269	-0.904	325 ± 50	60	
s054	J101104.53-044219.3	10:11:04.53	-04:42:19.3	O9.7 III	20.511	-0.202	-0.951	330 ± 30	125	
s055	J101053.90-044111.0	10:10:53.90	-04:41:11.0	O9.7 III	20.323	-0.103	-0.920	300 ± 30	103	Blend.
s056	J101100.94-044003.2	10:11:00.94	-04:40:03.2	O9.7 V	20.914	-0.147	-0.922	335 ± 30	98	Oe?
s057	J101059.58-044135.4	10:10:59.58	-04:41:35.4	O9.7 V	20.697	-0.110	-0.393	355 ± 35	59	
s058*	J101104.05-044226.1	10:11:04.05	-04:42:26.1	O9.7 V + B?	20.957	-0.204	-0.932	350 ± 50	40	SB2?
s059	-	10:10:57.09	-04:44:46.3	O9.7 Vn	-	-	-	355 ± 30	36	
s060*	J101107.27-044032.4	10:11:07.27	-04:40:32.4	O9.7 V	21.222	-0.065	-1.121	400 ± 100	26	Blend or bin? Broad He I.
s061	J101057.32-044055.4	10:10:57.32	-04:40:55.4	B0 I	19.915	-0.247	-0.899	290 ± 30	159	
s062	J101103.80-044212.8	10:11:03.80	-04:42:12.8	B0 I	20.358	-0.269	-0.872	315 ± 30	76	
s063	J101107.43-044025.4	10:11:07.43	-04:40:25.4	B0 III	20.727	-0.295	-0.885	305 ± 35	133	
s064*	J101108.49-043905.9	10:11:08.49	-04:39:05.9	B0 III	21.223	-0.268	-0.879	325 ± 50	44	SB2?
s065*	J101107.31-044205.3	10:11:07.31	-04:42:05.3	B0 V	20.889	-0.601	-0.595	100 ± 50	63	SB2? Be?
s066	J101058.01-044027.8	10:10:58.01	-04:40:27.8	B0.5 I	20.041	-0.225	-0.837	310 ± 40	124	
s067	J101059.29-044343.8	10:10:59.29	-04:43:43.8	B0.5 I	20.342	-0.137	-0.464	360 ± 40	82	
s068*	J101106.48-044210.5	10:11:06.48	-04:42:10.5	B0.5 I	20.521	0.272	-0.344	0 ± 50	69	= s093. 0.8'' slit. Bin. Blend.
s069	J101107.59-044159.9	10:11:07.59	-04:41:59.9	B0.5 II + O?	19.977	-0.214	-0.941	390 ± 40	109	SB2?
s070	J101106.03-044209.1	10:11:06.03	-04:42:09.1	B0.5 III	20.834	-0.272	-0.907	270 ± 45	82	C16-OB524
s071	J101105.69-044213.6	10:11:05.69	-04:42:13.6	B1 I	19.699	-0.236	-0.903	265 ± 35	256	Tilted 49°. SB1?
s072	J101059.21-043948.1	10:10:59.21	-04:39:48.1	B1 I	19.329	-0.192	-0.880	340 ± 30	211	C16-OB421. SB1?
s073	J101103.98-044232.5	10:11:03.98	-04:42:32.5	B1 I	20.069	-0.199	-0.790	285 ± 30	101	1.5'' slit.
s074	J101054.62-044103.0	10:10:54.62	-04:41:03.0	B1 I	19.739	-0.218	-0.942	330 ± 30	42	C16-OB422.
s075*	J101104.02-044222.9	10:11:04.02	-04:42:22.9	B1 I + O?	21.220	-0.023	-0.107	200 ± 50	34	0.8'' slit. SB2?
s076 <sup>†</sup>	2990	10:11:04.66	-04:42:23.6	B1 I	21.940	-0.070	-0.920	335 ± 40	29	
s077	J101054.08-044111.5	10:10:54.08	-04:41:11.5	B1 III	19.487	-0.217	-0.875	340 ± 30	92	C16-OB323. SB1. Blend.
s078	J101102.18-044315.4	10:11:02.18	-04:43:15.4	B1 III	21.290	-0.137	-0.915	290 ± 30	54	
s079*	J101105.82-044213.0	10:11:05.82	-04:42:13.0	B1 III	21.774	-0.163	-0.984	325 ± 50	50	Blend.
s080*	J101054.97-044116.2	10:10:54.97	-04:41:16.2	B1 III	21.471	-0.292	-0.983	250 ± 50	34	
s081 <sup>†</sup>	3646	10:11:06.21	-04:42:25.7	B1 V	23.250	0.000	-1.260	320 ± 40	44	Blend.
s082	J101105.65-044038.9	10:11:05.65	-04:40:38.9	B1.5 I	19.896	-0.186	-0.822	400 ± 30	160	
s083	J101055.35-044106.1	10:10:55.35	-04:41:06.1	B2 I	19.067	-0.171	-1.007	280 ± 30	183	C16-OB222. SB1.
s084	J101104.33-044220.8	10:11:04.33	-04:42:20.8	B2 I	20.552	0.061	-1.017	265 ± 35	72	0.8'' slit.
s085	J101104.69-044228.8	10:11:04.69	-04:42:28.8	B2 I	20.850	0.254	-	320 ± 30	62	1.5'' slit. SB1?
s086*	J101104.97-044218.9	10:11:04.97	-04:42:18.9	B2 III	20.509	0.107	0.014	100 ± 50	126	SB1?
s087	J101053.94-044110.1	10:10:53.94	-04:41:10.1	B2 III + O?	20.526	-0.230	-0.921	255 ± 35	79	Blend.

continued on next page

Table 1. continued.

ID	Alt. ID	RA (J2000.0)	DEC (J2000.0)	SpT	V	B – V	Q	$v_{\text{rad}}$ (km s <sup>-1</sup> )	S/N	Notes
s088*	J101110.46-044131.5	10:11:10.46	-04:41:31.5	B2 III + O?	21.265	-0.265	-0.435	325 ± 50	29	0.8'' slit. SB2?
s089	J101102.38-044014.6	10:11:02.38	-04:40:14.6	B2.5 I	19.581	-0.099	-0.683	340 ± 30	150	C16-OB622. Tilted -25°. Bin?.
s090	J101106.11-044229.8	10:11:06.11	-04:42:29.8	B2.5 I	20.358	-0.133	-0.507	295 ± 30	87	1.0'' slit. Blend.
s091	J101058.27-044257.8	10:10:58.27	-04:42:57.8	B2.5 I	19.176	-0.074	-0.706	330 ± 30	83	C16-OB221.
s092	J101105.50-044128.8	10:11:05.50	-04:41:28.8	B2.5 I	20.155	-0.141	-0.671	325 ± 30	77	
s093*	J101106.48-044210.5	10:11:06.48	-04:42:10.5	B2.5 I	20.521	0.272	-0.344	450 ± 50	51	= s068. 0.8'' slit. Bin. Blend.
s094*	J101058.58-044423.5	10:10:58.58	-04:44:23.5	B2.5 I + O?	21.621	0.205	-0.966	335 ± 50	37	Off-slit. Tilted 5°. SB2?
s095	J101105.96-044221.4	10:11:05.96	-04:42:21.4	B2.5 III	21.672	-0.188	-0.730	320 ± 30	47	
s096*	J101056.64-044102.1	10:10:56.64	-04:41:02.1	B2.5 III	21.062	0.263	-0.056	200 ± 50	34	0.8'' slit.
s097	J101107.62-044203.6	10:11:07.62	-04:42:03.6	B3 I	20.085	-0.175	-0.662	300 ± 30	158	0.8'' slit.
s098	J101106.12-044219.9	10:11:06.12	-04:42:19.9	B3 I	19.782	-0.163	-0.789	335 ± 30	136	
s099	J101102.75-044047.6	10:11:02.75	-04:40:47.6	B3 I	20.201	-0.141	-0.657	275 ± 40	121	
s100	J101051.62-044326.4	10:10:51.62	-04:43:26.4	B3 III	20.997	-0.263	-0.966	320 ± 35	62	
s101	J101054.45-044114.1	10:10:54.45	-04:41:14.1	B3 III	21.254	-0.328	-0.897	255 ± 35	43	
s102	J101104.59-044222.2	10:11:04.59	-04:42:22.2	B7 I	20.189	-0.074	-0.463	280 ± 35	94	
s103*	J101103.93-044214.0	10:11:03.93	-04:42:14.0	B7 I	20.437	-0.069	-0.386	400 ± 40	93	Blend.
s104	J101105.41-044210.9	10:11:05.41	-04:42:10.9	B7 I + O?	21.153	-0.206	-0.751	250 ± 40	90	1.5'' slit. Blend?
s105	J101104.42-044232.4	10:11:04.42	-04:42:32.4	B7 I	19.227	-0.075	-0.554	270 ± 35	86	
s106	J101106.02-044214.2	10:11:06.02	-04:42:14.2	B7 II	18.771	0.054	-0.277	250 ± 30	102	C16-OB121. SB1. Blend.
s107*	J101059.81-044305.5	10:10:59.81	-04:43:05.5	B7 III	20.575	0.126	-0.011	200 ± 100	77	1.5'' slit.
s108	J101105.86-044232.0	10:11:05.86	-04:42:32.0	B7 III + B?	21.560	-0.119	-0.464	320 ± 55	44	1.0'' slit. SB2?
s109*	J101107.14-044131.4	10:11:07.14	-04:41:31.4	B7 III + O?	21.538	-0.268	-0.873	350 ± 50	28	SB2?
s110	J101105.98-044217.9	10:11:05.98	-04:42:17.9	B8 I	20.008	-0.048	-0.358	260 ± 55	111	1.5'' slit.
s111	J101059.13-044051.0	10:10:59.13	-04:40:51.0	B8 II	20.486	-0.069	-0.412	340 ± 35	54	C16-OB324. Off-slit.
s112*	J101104.08-044224.2	10:11:04.08	-04:42:24.2	B8 III	21.104	0.038	-0.144	270 ± 30	67	0.8'' slit.
s113	J101059.15-044215.1	10:10:59.15	-04:42:15.1	B8 III	21.514	-0.111	-0.281	265 ± 35	38	1.0'' slit.
s114	J101056.30-044105.7	10:10:56.30	-04:41:5.70	B8 III	21.478	-0.228	-0.719	340 ± 50	23	Blend.
s115	J101105.17-044236.0	10:11:05.17	-04:42:36.0	B9 I	19.360	-0.044	-0.427	295 ± 250	95	0.8'' slit.
s116	J101054.89-044112.1	10:10:54.89	-04:41:12.1	B9 I	18.480	-0.010	-0.529	375 ± 30	75	C16-OB122. Blend.
s117	J101058.86-044126.2	10:10:58.86	-04:41:26.2	B9 III	20.169	0.020	-0.040	325 ± 45	46	0.8'' slit.
s118* <sup>†</sup>	3713	10:11:06.39	-04:42:16.4	B9 V	21.980	-0.120	-0.184	300 ± 100	35	
s119*	J101106.38-044155.9	10:11:06.38	-04:41:55.9	A0 II	20.519	-0.043	-0.155	350 ± 40	41	C16-OB525.
s120	J101107.24-044219.7	10:11:07.24	-04:42:19.7	A2 I	18.873	0.081	-0.009	370 ± 30	114	
s121*	J101054.71-044115.6	10:10:54.71	-04:41:15.6	A2 I	19.211	0.129	-0.019	270 ± 30	83	
s122	J101057.50-044208.9	10:10:57.50	-04:42:08.9	A2 I	19.499	-0.011	-0.259	275 ± 40	60	1.0'' slit.
s123	J101056.97-044206.6	10:10:56.97	-04:42:06.6	A2 III	20.449	0.172	-0.017	320 ± 40	32	1.0'' slit.
s124*	J101104.97-044233.8	10:11:04.97	-04:42:33.8	F5 I	17.477	0.174	-0.188	350 ± 40	132	C16-OB621. K04-SexA-513.
s125* <sup>†</sup>	J10111837-0440480	10:11:18.37	-04:40:48.1	F8 V	-	-	-	0 ± 30	74	Foreground.

**Table 2.** Blue type stars for which a spectral subtype could not be assigned. The description of columns is the same as Table 1.

ID	Alt. ID	RA (J2000.0)	DEC (J2000.0)	SpT	V	B − V	Q	$v_{\text{rad}}$ (km s <sup>−1</sup> )	S/N	Notes
s126* <sup>†</sup>	3545	10:11:06.00	-04:42:28.4	O V	B = 23.04	-	-	230 ± 50	48	Blend.
s127*	J101100.30-044330.7	10:11:00.30	-04:43:30.7	O V + gal	21.398	-0.071	-0.263	250 ± 100	84	
s128*	-	10:11:06.64	-04:41:33.5	O V	-	-	-	235 ± 100	8	
s129	J101104.28-044238.2	10:11:04.28	-04:42:38.2	O V + neb	21.237	-0.310	-1.000	330 ± 30	15	
s130	J101106.30-044140.8	10:11:06.30	-04:41:40.8	O	20.934	-0.075	-0.473	380 ± 45	15	Off-slit.
s131	J101106.32-043914.0	10:11:06.32	-04:39:14.0	O + neb	21.277	-0.140	-1.003	390 ± 35	31	
s132*	J101101.33-044150.9	10:11:01.33	-04:41:50.9	O V + neb	21.347	-0.093	-1.017	490 ± 70	23	Off-slit.
s133	J101100.17-043939.2	10:11:00.17	-04:39:39.2	O + neb	21.219	-0.098	-1.038	225 ± 30	74	
s134*	J101101.20-044337.2	10:11:01.20	-04:43:37.2	O V	21.097	-0.056	-0.447	325 ± 50	33	
s135*	J101105.28-044223.4	10:11:05.28	-04:42:23.4	O V	20.689	0.011	-0.239	325 ± 50	50	1.5'' slit.
s136	J101109.27-044147.7	10:11:09.27	-04:41:47.7	O + neb	20.639	-0.062	-1.111	435 ± 80	31	
s137*	J101108.58-044125.7	10:11:08.58	-04:41:25.7	Be + O?	21.007	-0.096	-1.108	325 ± 50	63	SB2?
s138*	J101100.56-044327.6	10:11:00.56	-04:43:27.6	B III + gal	20.406	0.026	-0.513	175 ± 50	69	1.0'' slit. SB1?
s139* <sup>†</sup>	3988	10:11:07.24	-04:41:50.3	B + O?	22.190	-0.180	-0.820	200 ± 50	18	SB2?
s140*	J101105.48-044202.9	10:11:05.48	-04:42:2.90	B III	20.907	-0.266	-0.837	250 ± 50	15	Off-slit.
s141	J101059.21-044348.8	10:10:59.21	-04:43:48.8	B	21.159	-0.138	-0.576	255 ± 85	16	Off-slit.
s142	J101055.14-044117.0	10:10:55.14	-04:41:17.0	B	21.422	0.230	-0.914	315 ± 50	26	Blend.
s143	-	10:11:06.17	-04:42:13.7	B	-	-	-	270 ± 40	27	0.8'' slit.
s144	J101105.90-044155.8	10:11:05.90	-04:41:55.8	B	21.535	0.043	0.069	305 ± 40	14	Off-slit.
s145* <sup>†</sup>	2432	10:11:03.50	-04:42:27.4	B	22.380	1.020	-	325 ± 50	24	0.8'' slit.
s146	J101101.76-044314.0	10:11:01.76	-04:43:14.0	B	21.678	-0.006	-0.306	345 ± 35	18	
s147*	J101101.90-044241.1	10:11:01.90	-04:42:41.1	B	21.001	-0.095	-0.393	150 ± 50	23	0.8'' slit.
s148*	J101101.93-044147.1	10:11:01.93	-04:41:47.1	OB	20.904	0.338	-0.216	325 ± 100	40	0.8'' slit.
s149*	J101103.95-044225.0	10:11:03.95	-04:42:25.0	OB	21.163	0.684	-	325 ± 100	36	0.8'' slit.
s150* <sup>†</sup>	3416	10:11:05.71	-04:42:10.6	OB	22.190	-0.260	-0.793	400 ± 100	32	0.8'' slit.
s151	J101105.55-044221.9	10:11:05.55	-04:42:21.9	OB	20.376	-0.002	-0.062	405 ± 85	29	Blend.
s152* <sup>†</sup>	2392	10:11:03.37	-04:42:28.9	OB	21.590	1.190	-	325 ± 50	28	0.8'' slit.
s153*	J101103.34-044156.2	10:11:03.34	-04:41:56.2	OB	21.589	-0.164	-0.440	245 ± 100	26	0.8'' slit.
s154*	J101100.55-044352.8	10:11:00.55	-04:43:52.8	OB	21.314	-0.115	-0.234	450 ± 50	22	
s155*	J101104.54-044229.7	10:11:04.54	-04:42:29.7	OB	22.006	-0.212	-0.142	325 ± 50	22	0.8'' slit.
s156* <sup>†</sup>	3509	10:11:05.95	-04:41:54.0	OB	22.180	-0.170	-0.848	205 ± 50	16	
s157*	-	10:11:07.12	-04:42:09.6	OB	-	-	-	260 ± 100	13	1.5'' slit.
s158*	J101057.38-044019.0	10:10:57.38	-04:40:19.0	OBA	21.217	-0.075	-0.284	460 ± 50	34	Tilted 8°.
s159*	J101105.64-044224.0	10:11:05.64	-04:42:24.0	OBA	21.023	-0.204	-0.528	325 ± 100	32	Blend.
s160*	J101101.83-044117.6	10:11:01.83	-04:41:17.6	OBA	20.706	-0.032	0.039	160 ± 50	27	1.5'' slit.
s161	J101108.21-044153.5	10:11:08.21	-04:41:53.5	OBA	21.899	-0.153	-1.048	440 ± 55	25	
s162	J101105.15-044212.8	10:11:05.15	-04:42:12.8	OBA	21.676	-0.080	-0.357	475 ± 230	24	
s163*	J101103.49-044157.2	10:11:03.49	-04:41:57.2	OBA	21.063	0.263	-0.123	290 ± 100	20	0.8'' slit.
s164*	J101106.92-044217.8	10:11:06.92	-04:42:17.8	OBA	22.253	-0.436	-0.616	325 ± 150	19	
s165*	J101057.66-044130.2	10:10:57.66	-04:41:30.2	OBA	21.497	-0.107	-0.130	325 ± 100	19	
s166*	J101104.51-044225.9	10:11:04.51	-04:42:25.9	OBA	20.934	-0.201	-0.925	350 ± 100	17	

**Table 3.** Late type stars observed in this work. Identification codes (ID), spectral types (SpT) and radial velocities ( $v_{\text{rad}}$ ) are included. Stars whose radial velocity was determined manually are marked with <sup>(\*)</sup>. Identifications numbers and coordinates by [Massey et al. \(2007\)](#) are provided when available, otherwise we give the ones from the 2MASS catalogue ([Cutri et al. 2003](#)) and mark the sources with <sup>(†)</sup>. Column *Memb.* flags the membership to Sextans A.

ID	Alt. ID	RA (J2000.0)	DEC (J2000.0)	SpT	<i>V</i>	<i>B</i> – <i>V</i>	$v_{\text{rad}}$ (km s <sup>−1</sup> )	Memb.	Notes
s167*	J101106.39-044218.1	10:11:06.39	-04:42:18.1	G5 I	19.588	1.446	300 ± 30	yes	<a href="#">BR19</a> -Sextans A 6.
s168*	J101106.00-044212.5	10:11:06.00	-04:42:12.5	G8 I + B7 I	19.453	1.689	350 ± 30	yes	0.8'' slit. Blend.
s169*	J101103.95-044228.3	10:11:03.95	-04:42:28.3	G8 I	20.031	1.768	250 ± 30	yes	<a href="#">BR19</a> -Sextans A 4.
s170*	J101102.21-044149.4	10:11:02.21	-04:41:49.4	K0 V	16.785	0.747	40 ± 30	no	0.8'' slit.
s171*	J101116.62-044014.4	10:11:11.78	-04:41:18.6	K2 V	20.144	1.349	0 ± 30	no	
s172*	J101104.78-044238.8	10:11:04.78	-04:42:38.8	K5 III	20.266	1.423	300 ± 40	yes	1.0'' slit.
s173* <sup>†</sup>	J10110861-0440473	10:11:08.60	-04:40:47.0	K7 V	-	-	0 ± 30	no	Off-slit.
s174*	J101115.72-044441.0	10:11:15.72	-04:44:41.0	M3 V	19.797	1.714	0 ± 30	no	1.5'' slit.



#### 4.1.1 Spectral content of the catalogue

Although our observations were designed to find OB stars in Sextans A, we also observed other types of sources. Here we briefly describe the objects classes unveiled by our observations.

**O stars.** There are 71 O-type stars in the sample. Among them, we find the stars with the earliest spectral types observed at metallicities lower than  $1/5 Z_{\odot}$ . Some of the sources classified as O-types are candidates to undergo chemically homogeneous evolution or to host a stripped star. This will be discussed in more detail in Section 5.2.

**BA supergiants.** Our sample contains 38 B- and A-type supergiants. This collection will allow us to better constrain the current chemical composition of Sextans A and to study the  $[\alpha/\text{Fe}]$  abundance ratio. The quantitative analysis of the spectra of 22 early-B supergiants will yield the abundances of C, N, O and Si. Strikingly, the silicon lines in the observed spectra appear weaker than predicted for their corresponding types and the metallicity of the galaxy. The abundance of magnesium and iron-group elements, can be derived from analyses of late-B and A supergiants. These analyses will be carried out as future work.

**Red stars.** There are 4 evolved stars from Sextans A in our catalogue, two of them already reported by Britavskiy et al. (2019, B19). These two are reclassified from K1-3 to G types. This update reinforces the observed trend of the average spectral types of red supergiants (RSGs) shifting towards earlier types at lower host galaxy metallicity (Elias et al. 1985; Massey & Olsen 2003; Levesque & Massey 2012). A plausible explanation for this observed pattern is the dependence of the molecular bands, main indicators of spectral type in evolved stars, on the metallicity of the environment. However, this trend may also reflect the shift of the Hayashi limit to higher effective temperatures as the metallicity decreases (Elias et al. 1985).

**Foreground stars.** 5 foreground stars landed in our programmed slits. Their identification as non-members of Sextans A is justified in Section 4.2.

**Binary candidates.** A total of 33 stars show some signatures of binarity in their spectra. Some targets present radial velocity variations between different observations. These are marked as "SB1" in the *Notes* column of Tables 1-3, along with a question mark when the variation was smaller than  $50 \text{ km s}^{-1}$  or the S/N of the data was poor. Those sources whose spectra show doubled-peaked lines or exhibit lines of a second component are marked as "SB2". The ones that met other binary diagnostics, such as variation in their spectral features, are labelled as "Bin". All of these cases are discussed individually in Appendix C. We note that this constitutes the first sample of candidate binary systems ever reported in Sextans A.

#### 4.2 Membership

To assess the membership of the targets to Sextans A, we inspect whether they have registered parallaxes or proper motions in the Gaia Early Data Release 3 (Gaia EDR3, Gaia Collaboration et al. 2021). Given the distance to the galaxy, the majority of the catalogue stars are too faint to have an entry in Gaia. For those that are included, we expect null proper motions and parallaxes. Most of our sample stars follow this trend.

We find 12 stars that deviate from the expected parameters. Two of them had already been identified as foreground based on their radial velocity (Sect. 4.3). The rest of the sources lie within  $2\sigma$  of the mean of the weighted normal distribution of the Gaia entries for Sextans A, for both parallax and proper motions. We thus consider that they follow the general trend observed in the galaxy and discard them as outliers.

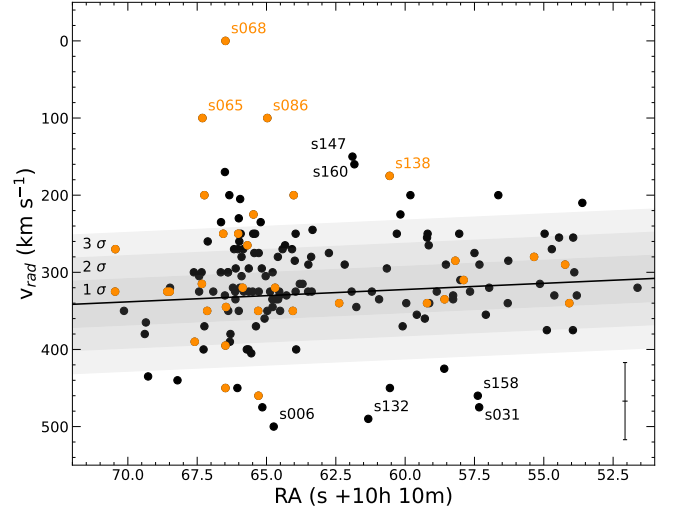


**Figure 1.** Comparison of the radial velocities obtained for the sample stars and the H I rotation curve of Sextans A derived by Skillman et al. (1989). We excluded from the figure stars identified as foreground. The shaded area represents the  $1\sigma$ ,  $2\sigma$  and  $3\sigma$  uncertainty of the measured rotation curve, being  $\sigma = 30 \text{ km s}^{-1}$ . Stars whose IDs are provided depart more than  $3\sigma$  from the radial velocity curve, after error bars have been considered. We also highlight in orange our list of binary candidates identified from spectral features. In the lower-right corner of the figure, we draw a representative error bar illustrating the average radial velocity error of  $\pm 50 \text{ km s}^{-1}$  for a star observed with resolution  $R = 1000$ .

We also checked that the absolute magnitudes  $M_V$  of all catalogue stars (calculated as described in Section 4.1) are consistent with their spectral type at the distance of Sextans A. There are only small discrepancies with respect to the calibrated values, which are discussed in Sect. 5.2.

Finally, we used radial velocity ( $v_{\text{rad}}$ ) as an additional membership check for all of our sample stars. A group of 5 late type stars with  $v_{\text{rad}} \leq 40 \text{ km s}^{-1}$  was identified as foreground. For the rest of our survey, the majority presents radial velocities consistent with the systemic velocity and radial velocity curve of Sextans A, as discussed in Section 4.3, which further supports their membership to the galaxy.

#### 4.3 Radial velocity

We estimated the radial velocity of each star by measuring the Doppler shift experienced by the hydrogen and helium lines. Using an automatic procedure, we determined the centroid of the lines by fitting their profile to a Gaussian function. To avoid biases introduced by nebular oversubtraction that may affect the core and introduce profile asymmetries, we imposed a higher weight on the line wings, defined as the points located between the continuum and a value set by the program. The height of this threshold was selected according to the strength of the lines compared to the local continuum. We calculated the depth of the lines as the difference between the flux of their cores ( $f_{\text{min}}$ ) and the continuum, and positioned the threshold at 15% and 30% of the estimated depth for strong ( $1 - f_{\text{min}} > 0.4$ ) and weak ( $1 - f_{\text{min}} \leq 0.4$ ) Balmer lines, respectively. These values stem from the fact that contrasts higher than  $1 - f_{\text{min}} > 0.4$  are likely caused by nebular oversubtraction. For He lines, where nebular oversubtraction is less prominent, we set the threshold at 50% of the line depth for weak ( $1 - f_{\text{min}} < 0.1$ ) lines and 80% for strong ( $1 - f_{\text{min}} \geq 0.1$ ) lines.

After the program fits all lines automatically to Gaussian profiles,

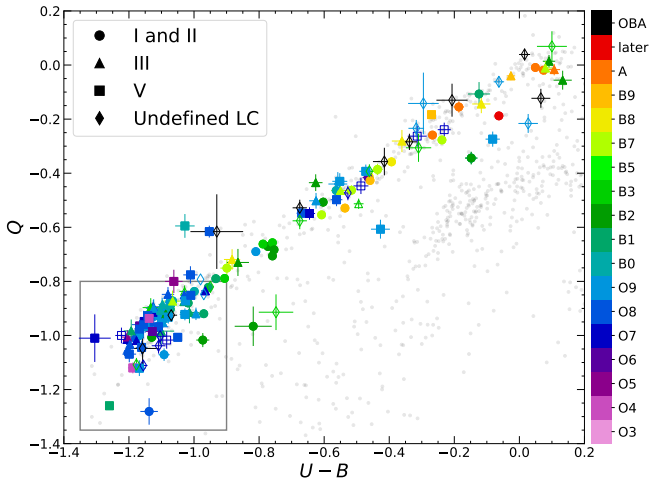


**Figure 2.**  $U - B$  vs  $Q$  diagram of Sextans A, showing Massey et al. (2007)’s catalogue in grey. The main criterion to select candidate O- and early B-type stars for our observing runs was  $Q \leq -0.8$ . The observed stars, excluding foreground sources, are colour-coded by spectral type and marked based on their luminosity classes (see legend). Stars without a defined spectral subtype are drawn with empty symbols. Most of the O-type stars confirmed by this work are found within the black box, which further supports the efficiency of the  $Q$  pseudo-colour as a selection criterion of massive stars.

it then rejects results from some lines in two steps according to: (i) their depth with respect to the noise of the spectrum (S/N values are compiled in Tables 1-3), and (ii) their line width, rejecting lines when the width exceeded twice the median of all fitted lines of the spectrum. We also imposed a limit of  $1000 \text{ km s}^{-1}$  to the resulting values of the radial velocity for individual lines and applied a  $\sigma$ -clipping algorithm using the median as a reference and rejecting by  $2\sigma$ . Finally, we calculated the weighted average of the estimated  $v_{\text{rad}}$  of the selected lines.

The uncertainty was calculated by averaging the error of the Gaussian fit to the selected lines and then dividing by the square root of the number of used lines. This result depends not only on the spectral S/N, but also on the number of lines suitable to measure the radial velocity.

The radial velocity of some stars in the sample could not be determined by our automatic measurement due to poor spectral S/N. In such cases, we defined the central wavelength of lines manually and estimated their corresponding Doppler shift. The assigned uncertainty was also determined manually. These stars are marked with (\*) in Tables 1-3.

In Fig. 1, we compare our results with the rotation curve of Sextans A, derived by Skillman et al. (1989), to assess the membership of our sample stars to the galaxy. Overall, our targets are consistent with Sextans A’s radial velocity. However, there are ten sources (identified in the Figure) whose radial velocity (and error bars) departs from the H I rotation curve by more than  $3\sigma$ , being  $\sigma$  the estimated error of the curve ( $\sigma = 30 \text{ km s}^{-1}$ ). The  $v_{\text{rad}}$  departures of the ten outliers could be explained by a possible runaway nature or their belonging to a multiple system. Yet, spectroscopic follow-up will be needed to confirm any of these hypotheses. We highlight in orange the stars identified as binary candidates from their spectra in Figure 1.

#### 4.4 The $Q$ pseudo-colour as an indicator of OB type stars

Due to their degenerate colours in the optical range and the effect of extinction, O- and early B-type stars cannot be identified using photometry only. However, Garcia et al. (2009) found that the OB stars of the galaxy IC 1613 lied in a particular locus of the  $U - B$  vs.  $Q$  diagram (see their Fig. 5). This is a consequence of the biunivocal relation between the reddening-free pseudo-colour  $Q = (U - B) - 0.72(B - V)$  and spectral type that holds down to A0 types. We have used this as the main criterion to select OB candidates in our subsequent discovery spectroscopic runs. Garcia & Herrero (2013) used  $Q < -0.8$  together with UV photometry, achieving a success rate of 70% in the detection of O-type stars in IC 1613. With the same criteria, Camacho et al. (2016) had a 50% rate in Sextans A.

The stars in our more extended catalogue are distributed throughout a broad range of  $Q$  values, which enables us to reassess the efficiency of this candidate selection criterion.

Roughly half of our catalogue, 79 stars, are found in the  $Q < -0.8$  box (see Figure 2). Of these, we find 50 O-type stars, including the earliest of the sample, 26 B stars, the majority earlier than B1.5, and 3 OB stars. The latter are not considered in the forthcoming statistics since their poor spectral S/N prevented us from assigning more definite spectral types. The ratio of confirmed O-type stars and total observed stars within the  $Q < -0.8$  box is 66%. However, if we push this criterion further and reduce the candidate box to values of  $Q < -1.0$ , the number increases to 84%, with 21 O stars out of the 25 stars with confirmed spectral type below this limit. Therefore, in the hunt for the high-mass stars in Sextans A and other galaxies, we advise selecting candidates with very low  $Q$  values.

Outside the  $Q < -0.8$  box, we found 17 O stars. The reason for their locus in the  $U - B$  vs.  $Q$  diagram is unclear. For instance, in the case of the O star s127, its colours are unreliable as the star overlaps with a foreground galaxy (see individual notes in Appendix C). Therefore, if we aim to seek completeness in the O star population of the galaxy, we must observe beyond the  $Q < -0.8$  box. This highlights the importance of untargted surveys of galaxies to fully account for their population of massive stars.

## 5 DISCUSSION

We have obtained spectroscopy of 174 sources, of which 159 are OB stars (including 41 whose spectral subtype could not be assigned due to poor spectral S/N), 6 are A- and F-type stars, 4 are red giants/supergiants members of Sextans A, and 5 are identified as foreground stars. In addition, we provide the first list of binary candidates with metallicities of  $1/10 Z_{\odot}$  and a list of candidates experiencing chemically homogeneous evolution or systems hosting a stripped star (see Sect. 5.2).

Few massive stars were previously known in very low metallicity environments, as they are located at far distances (Garcia et al. 2021). The existing catalogues in IC 1613, WLM and NGC 3109, with  $1/7 O_{\odot}$  and  $1/5 \text{ Fe}_{\odot}$ , do not exceed seventy stars (e.g. Bresolin et al. 2006, 2007; Evans et al. 2007; Garcia & Herrero 2013). In our target galaxy Sextans A, with  $1/10 Z_{\odot}$ , only 19 massive stars had been confirmed so far (Camacho et al. 2016; Garcia et al. 2019). At lower metallicities, only 2 OB stars in SagDIG ( $\sim 1/20 O_{\odot}$ , Garcia 2018) and one confirmed O-type star in Leo P ( $\sim 1/30 O_{\odot}$ , Evans et al. 2019) are known.

The sample of 159 OB stars assembled in this work constitutes the largest census of massive stars at sub-SMC metallicities to date. This catalogue also enables us to study the recent star formation

history of Sextans A and provides a first glimpse into the evolution of  $1/10 Z_{\odot}$  massive stars. We discuss the two topics in this section.

### 5.1 The recent star formation history of Sextans A

After a quiescent period of 7.5 Gyr, star formation resumed 2.5 Gyr ago in Sextans A and has been growing continuously, with an increase in the last 0.6 Gyr (Dolphin et al. 2003). The galaxy hosts three major regions with confirmed ongoing star formation, qualitatively defined by Dohm-Palmer et al. (2002) and named region-A, -B and -C by Camacho et al. (2016, see also Fig. 3). Region-A (in the north) has been forming stars for the past 400 Myr and it is about to exhaust its local gas content. The other two, regions-B (in the southeast) and -C (in the northwest), have been active for 200 Myr and 20 Myr, respectively, and overlap with the higher concentrations of ionized and neutral hydrogen that frame the visually bright part of the galaxy (van Dyk et al. 1998; Dohm-Palmer et al. 2002). Recently, Garcia et al. (2019) found young massive stars in the southern tip of Sextans A and coined this area as region-D.

With typical ages under 50 Myr, massive stars signal ongoing star formation. In Fig. 3, we show the location of the sample stars in Sextans A and use our 159 OB sources as star formation tracers.

Most of the OB stars are located in regions-B and -C, overlapping with the high column density areas of neutral gas and producing large structures and shells of ionized hydrogen. Other preferred locations for hot stars are the northeastern and southern edges of the galaxy, where they ionize small H II bubbles and arcs.

The stars holding the earliest types (see Fig. 3) are located independently of the stellar density and star-forming rate of their host areas. Regions-B, -C, and -D correspond to regions-1, -3, and -4 from Shi et al. (2014), who inferred star formation rates using FUV photometry from GALEX of  $-2.66$ ,  $-2.32$  and  $-3.19 \log M_{\odot} \text{yr}^{-1} \text{kpc}^{-2}$ , respectively. Finding such early types in these three areas indicates that star formation has been active until at least 5 Myr ago (Massey 2003). No supernova remnant that could help us further trace star formation is known.

Region-B presents more dispersion in spectral types, and we have found more early-type stars than in the other star-forming regions of the galaxy. This is in line with Camacho et al. (2016)'s suggestion that, although activated longer ago, region-B is still undergoing star formation.

The distribution of massive stars in region-B appears to be layered by spectral type and correlated with the column density of the neutral gas (see Fig. 4). The early O-type stars overlap with the highest density of H I (left panel of Fig. 4), while the later types are located at the inner edges of the H I cloud where the column density is lower (middle and right panels of Fig. 4). The stratification might indicate a temporal sequence of star formation, which would proceed from the inner rim outwards, following the H I column-density gradient. Region-C could show a similar layered pattern, although the catalogue coverage is more sparse in this area due to the way the observing runs were planned.

A significant fraction of OB stars in our census are found on the outskirts of Sextans A, at the edges of the neutral gas reservoir and with no associated H II structures (see left panel of Fig. 5). Garcia et al. (2019) already pointed out these unexpected star-forming sites with the detection of star s041 (their s1) in the southern region of the galaxy. Similar examples exist in other galaxies near and far. Garcia et al. (2010) spotted OB associations and UV sources outside the brightest centre of IC 1613. The detection of extended UV-disc galaxies (Gil de Paz et al. 2005) already suggested the existence of star formation in low-gas density environments on the galactic

outskirts. Only the spectroscopic confirmation of OB stars at these sites has allowed us to directly associate some of the UV sources with massive stars. In addition, we also find OB stars in the central part of the galaxy, where star formation was considered already finished. This recalls the massive star V39 detected by Herrero et al. (2010) in an inconspicuous region of IC 1613, and resembles the observed star formation in the outer fringes of the galaxy. Examples of star formation at low H I column density also occur in low-mass dwarf galaxies outside the Local Group (e.g. Teich et al. 2016).

The existence of an underlying population supporting these apparently isolated stars cannot be discarded since no sufficiently deep IR observations of the galaxy exist. Yet, Garcia et al. (2019) examined archival WFC3-IR observations of region-D and found no additional stars around s1. Moreover, *Herschel* observations do not support the existence of large masses of dust at the location of most of these isolated stars.

Could these isolated stars be runaways? Given the distance to Sextans A, we cannot infer any information from proper motions. A star crossing the entire galaxy in 10 Myr would exhibit proper motions of  $\sim 0.01 \text{ mas/yr}$ , significantly lower than the typical uncertainties of Gaia for the proper motions of stars with  $G = 20 \text{ mag}$  ( $0.5 \text{ mas/yr}$ , Lindegren et al. 2021).

We have manually selected sources that are far from region-A, -B, -C and -D and highlighted them in Fig. 5. The distances between the isolated sources and the approximate centre of their nearest star-forming regions (see right panel of Fig. 5) range between 250 and 825 pc. Assuming lifetimes of 10 Myr and ejection at early stages of evolution, covering these distances would correspond to projected velocities of  $25\text{--}80 \text{ km s}^{-1}$ . These values could be consistent with the high-end tail of the probability distribution of runaway stars produced by binary interaction found by Renzo et al. (2019). At the metallicity of Sextans A, their calculations suggest that the velocity of the ejected stars would be  $\sim 10 \text{ km s}^{-1}$  higher on average. This is still significantly lower than the velocity of the alleged runaways. Moreover, the fraction of expected unbound binaries would be lower at low metallicity. Given the low expected probability of these cases ( $< 0.01\%$ , Renzo et al. 2019), we consider unlikely that these are runaway stars.

We therefore conclude that these sources were likely formed in situ, perhaps supported by compact, CO-dark gas clouds not signalled by H I maps. An alternative explanation would be that they are the products of mergers of two or more lower-mass sources, although this possibility does not solve the conundrum of the missing underlying population.

### 5.2 Evolutionary status

Fig. 6 shows Sextans A's colour-magnitude diagram (CMD) built with Massey et al. (2007)'s photometric catalogue, highlighting our sample stars. We also incorporate blue and red supergiants from previous studies by Kaufer et al. (2004) and Britavskiy et al. (2019).

We include evolutionary tracks by Szécsi et al. (2022) with Sextans A's metallicity ( $Z = 0.10 Z_{\odot} = 0.00105$ ) and an initial rotational velocity of  $v \sin i = 100 \text{ km s}^{-1}$ , consistent with the average rotational velocity of OB stars in other low metallicity regimes (e.g. Sabín-Sanjulián et al. 2017; Ramírez-Agudelo et al. 2017; Ramachandran et al. 2019). To compare observations with the evolutionary predictions, we computed the synthetic photometry of the evolutionary tracks using a grid of TLUSTY atmosphere models with an iron abundance of  $[\text{Fe}/\text{H}] = -1.0 \text{ dex}$ . For each point of the tracks, defined by effective temperature ( $T_{\text{eff}}$ ) and surface gravity ( $\log g$ ), we assigned an atmosphere model by using a four-point lin-



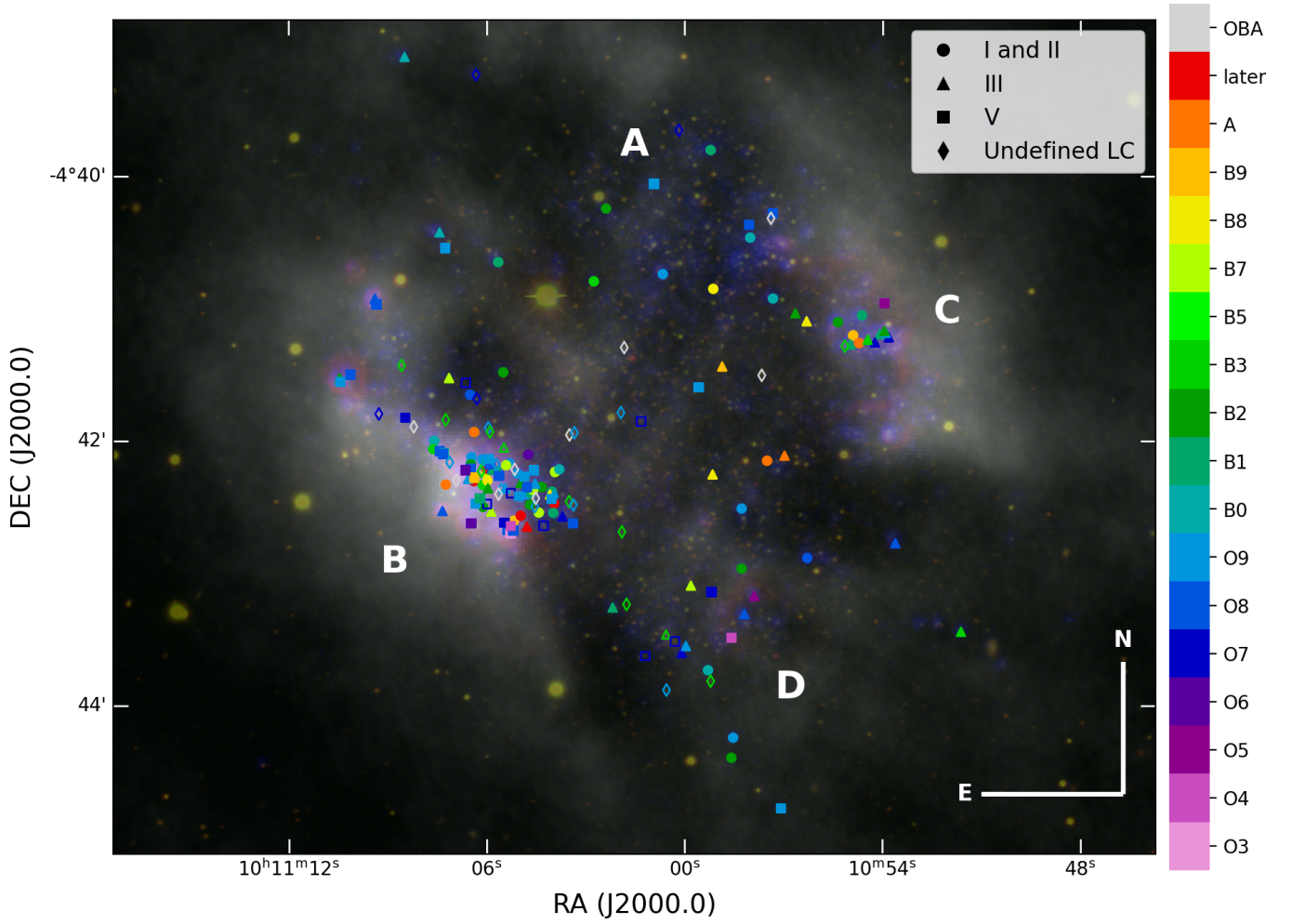


**Figure 3.** Sextans A RGB composite image made with H $\alpha$ – (red) and V–bands (green) from Massey et al. (2007), and GALEX FUV (blue). The *LITTLE THINGS* neutral hydrogen map (Hunter et al. 2012) is overlaid in white. Regions with confirmed ongoing star formation are marked in the figure. We show the catalogue stars, excluding identified foreground stars, colour-coded according to their spectral type and with different symbols based on their luminosity class. Stars with an undefined spectral subtype are drawn with empty markers.

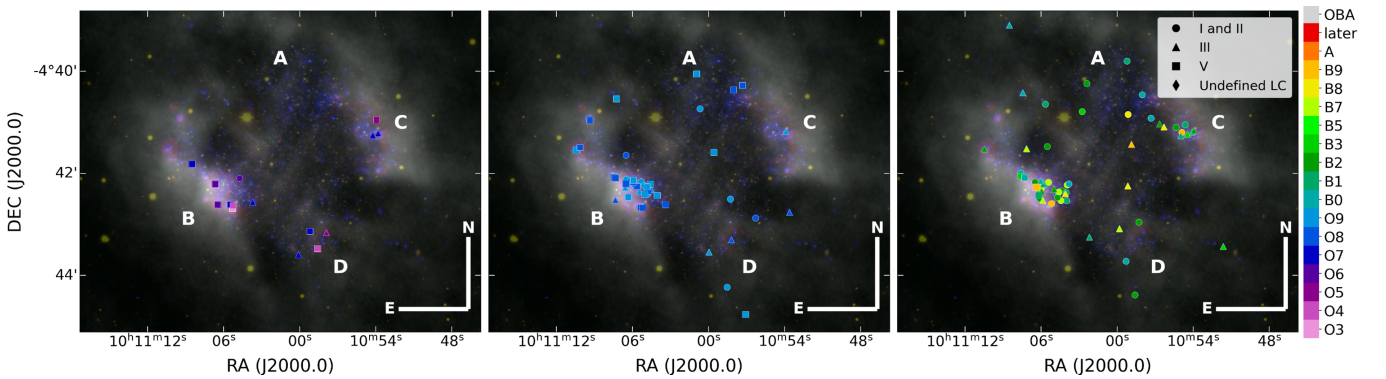


**Figure 4.** Same as Fig. 3. Each panel shows the sample OB stars in different intervals of spectral type. From left to right, we plotted targets with spectral types earlier than O8, stars with types between O8 and O9.7 (both included), and sources classified as B-type stars. There is an apparent stratified pattern of spectral type in region–B, where the early O-type stars overlap with the high gas density areas, and later types are located at the inner rims of the H I cloud.



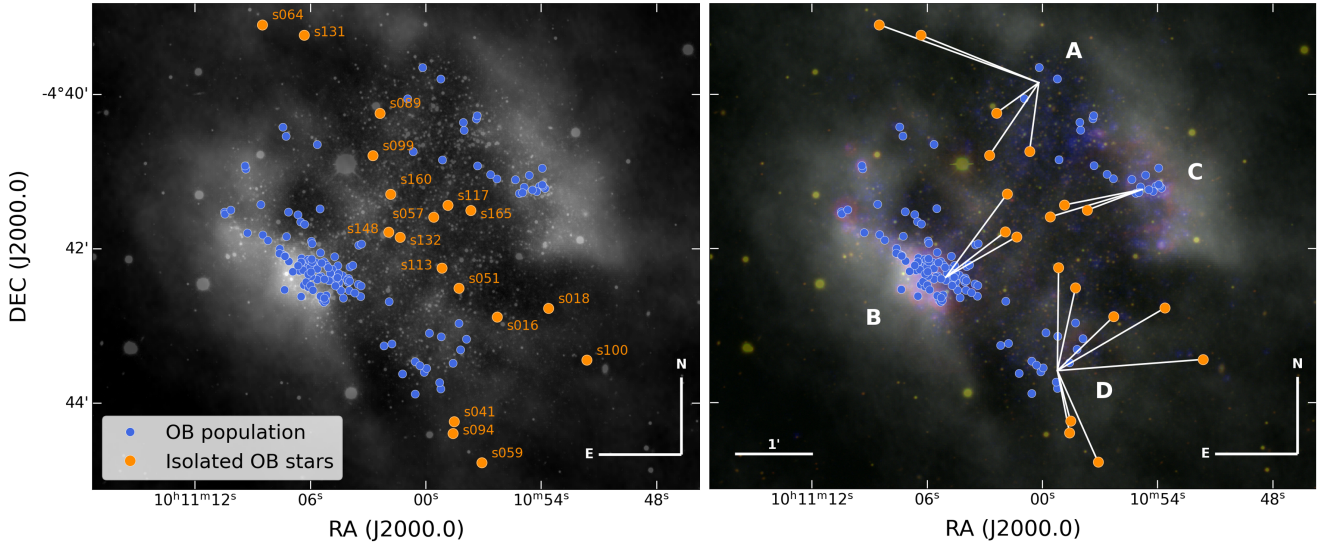


**Figure 5.** Left: *LITTLE THINGS* neutral hydrogen map (Hunter et al. 2012) overlaid on a V-band image of Sextans A (Massey et al. 2007). We show the population of OB stars in blue, and identify and highlight in orange the isolated OB stars. Right: Same RGB image as Fig. 3. We again highlight the isolated OB stars in orange and show the distance these stars would have travelled from their nearest OB population if they were runaway stars (white lines). A projected angle of 1' corresponding to a distance of 390 pc in Sextans A is plotted as reference.

ear interpolation. Some regions of the evolutionary paths lay outside the *TLUSTY* grid coverage, and only 2 or 3 points could be used to interpolate, leading to perhaps non-realistic atmospheres. These regions are shown as dashed lines in Fig. 6. Finally, the tracks are shifted to account for the distance modulus ( $\mu_0 = 25.63$ , Tammann et al. 2011) and foreground extinction ( $E(B - V)_{fg} = 0.044$ , Skillman et al. 1989) of Sextans A. No correction is applied to the photometry of the catalogue stars.

The OB stars of our catalogue are spread across the blue plume. The observed dispersion in both spectral types and luminosity classes impact the masses and ages that can be derived from the evolutionary tracks. Although most of the earliest stars concentrate in the bluest regions of the plume, others overlap with stars of later spectral types. The spread can be partly explained by the intrinsic errors of the assigned spectral type, but it is mostly caused by internal interstellar extinction. The same effect has been observed in other LG dIrr galaxies like IC 1613 (Garcia et al. 2009) and SagDIG (Garcia 2018). A thorough characterisation of the internal extinction of Sextans A will be published in a subsequent paper of this series.

The late-type stars of Sextans A are mainly found at the red ends of the evolutionary tracks. They are concentrated in two different groups, a less massive one between 12 and 19  $M_{\odot}$  and a second population with higher initial evolutionary masses ranging between 30 and 40  $M_{\odot}$ . Recent works (Beasor et al. 2019; Britavskiy et al. 2019) speculate that the more luminous and massive group of RSGs are the evolved analogues of the massive blue straggler stars and might be products of mergers or binary mass transfer.

We detect that 18 OB-type stars exhibit bluer colours than the evolutionary tracks (shaded region in Fig. 7). This number may increase after internal reddening is corrected. Slowly rotating single-star evolutionary tracks do not predict OB stars in this locus, as shown in Fig. 6. We imposed a lower limit on  $B - V$  of  $-0.36$  mag corresponding to the colour of a blackbody with  $T_{\text{eff}} = 200$  kK (the highest effective temperature observed in Wolf-Rayet stars, Sander et al. 2012; Trammer et al. 2015). Photometric measurements bluer than this value are discarded as spurious. They might be due to strong

emission lines contributing to the total spectral energy distribution and thus the measured colours.

A star might reach extreme hot temperatures, hence blue colours, if it evolves chemically homogeneously. Rapid rotation may lead a massive star to efficient mixing, dragging helium into its envelope as it is produced, and thus never establishing a chemical gradient (Maeder & Meynet 2000). With hydrogen still burning in its core, the star will evolve to colours and effective temperatures hotter than the ZAMS, entering a Wolf-Rayet-like stage and remaining extremely hot throughout its lifetime (Yoon & Langer 2005). This evolutionary path is more expected among very low- $Z$  massive stars (Brott et al. 2011), since the reduced mass- and angular momentum-loss *via* winds may allow for rapid rotation rates. However, there is still no observational confirmation for the existence of CHE stars.

The photometry and the assigned spectral types of some of the stars in the blue locus are consistent with them following chemically homogeneous evolution. However, this needs to be confirmed with measurements of high helium surface abundances and large rotational velocities ( $v \sin i > 250 \text{ km s}^{-1}$ ). Unfortunately, the S/N and the resolution ( $\sim 300 \text{ km s}^{-1}$ ) of the current data set do not allow such analysis.

Alternatively, these sources could be post-binary interaction products, in particular, binary systems whose primary star has been removed of its hydrogen-rich envelope through the interaction with its companion. This loss produces very compact, hot helium stars (e.g. Kippenhahn 1969; Podsiadlowski et al. 1992), known as stripped stars. Theoretical atmosphere models predict that the spectra of these objects at their high-mass end show He and N lines (Götberg et al. 2017), similar to the observed in nitrogen-rich Wolf-Rayet stars. Such spectral features have not been detected within our sample. However, at  $Z = 1/5 Z_{\odot}$  and intermediate or low mass values, their spectra present typical features of early O-type stars with nitrogen enrichment (Götberg et al. 2018). Some of our blue outliers exhibit this spectral morphology. On the other hand, if the companion of the stripped star were to dominate the optical part of the spectrum, we would observe a typical OB spectrum, possible signals of multiplicity and UV and blue photometric excess. The star would also experience

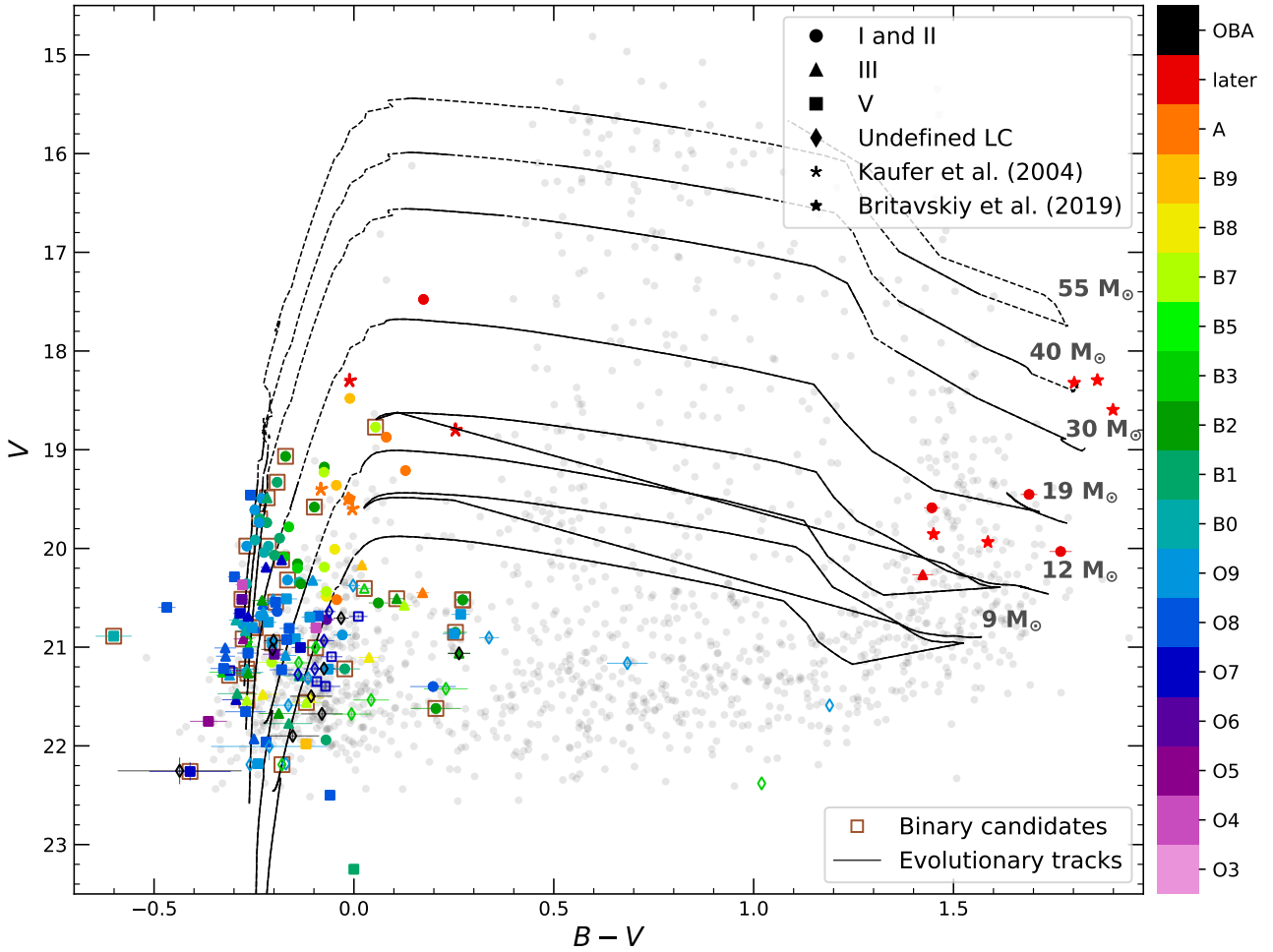


**Figure 6.** CMD of Sextans A, showing Massey et al. (2007)’s catalogue in grey and our sample sources, excluding foreground stars, colour-coded according to their spectral type. Those without a defined spectral subtype are drawn as empty symbols. Their luminosity classes are indicated by different symbols (see legends), and binary candidates are marked with empty brown squares. We include Kaufer et al. (2004) and Britavskiy et al. (2019) supergiants, labelled with distinct markers. Error bars for the photometry are shown; we note that errors for the  $V$ -band magnitudes are usually smaller than the symbol size. The computed photometry for  $Z = 0.10 Z_{\odot}$ ,  $v \sin i = 100 \text{ km s}^{-1}$  evolutionary tracks by Szécsi et al. (2022) are also provided (see Sect. 5.2). Dashed lines mark the points where the interpolation of the theoretical atmosphere models to calculate the photometric magnitudes was incomplete. The tracks have been shifted to account for Sextans A’s distance modulus and foreground extinction.

higher rotational velocities after the mass and angular momentum transfer. We detect 4 binary candidates within the 18 sources found at bluer colours than the evolutionary tracks.

We have assessed the different features that both CHE stars and systems hosting a stripped star would exhibit. According to the theoretical predictions, CHE stars are hot and underluminous for their spectral type (Kubátová et al. 2019). They also hold high projected rotational velocities and helium abundances. On the other hand, systems hosting a stripped star would show signs of multiplicity and UV excess. If the stripped star dominates the optical spectrum, it would present a lower luminosity than a star with the same spectral classification (Götberg et al. 2018).

With this in mind, we have compiled a selection of properties for the list of blue outliers in Table 4. We have analysed the location of these stars in the ultraviolet CMD using photometry by Bianchi et al. (2012) (see Fig. 8), noting whether or not they are also blue outliers in this diagram, which would flag the existence of a UV excess. In addition, we have derived the luminosity of these objects using Sextans A’s distance modulus  $\mu_0 = 25.63$  (Tammann et al.

2011),  $(B-V)_0$  colours estimated from the pseudo-colour  $Q$  (Massey et al. 2000) and calibrations to estimate effective temperatures and bolometric corrections (Balona 1994; Martins et al. 2005; Markova & Puls 2008). A luminosity lower than the calibrated values by Martins et al. (2005); Ramachandran et al. (2019) for their spectral type would qualify the objects as candidates for CHE or stripped stars. Nine blue outliers are underluminous compared to the calibrations by a difference of  $\geq 0.2$  dex.

Finally, we have also studied whether the spectra are consistent with high projected rotational velocities to support their designation as CHE candidates or companions to stripped stars. We have used FASTWIND models compatible with the assigned spectral classification of the candidates (Lorenzo et al. in prep.) and helium abundance of  $\epsilon = 0.09$ , and convolved to the resolution of the respective observations. Since the S/N and  $R \sim 1000$  of our observations prevent us from discerning  $v \sin i$  in the range of  $75\text{--}300 \text{ km s}^{-1}$ , we have checked whether the line profiles of the observed spectra were broader than the synthetic lines with  $v \sin i = 300 \text{ km s}^{-1}$  (see Fig. 9 for an example of the followed procedure). Results of the evaluation

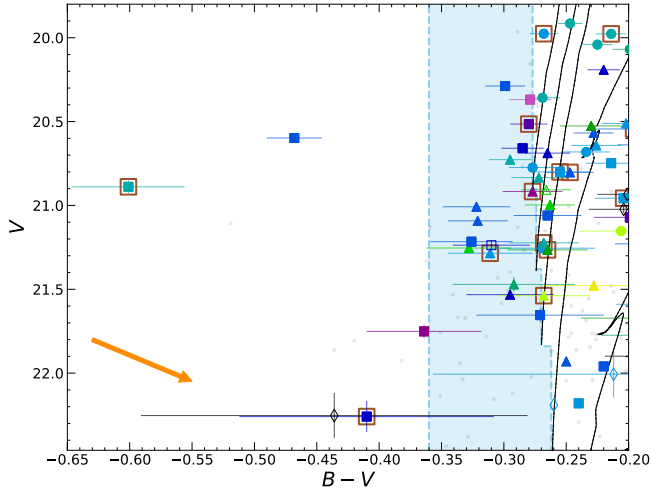


**Figure 7.** Same as Fig. 6, zooming into the main sequence and blue colours. We shade in blue the area of blue colours than the evolutionary tracks, with a lower boundary in  $B - V$  defined by the intrinsic colour of a blackbody at 200 kK. This region contains the list of blue outliers listed in Table 4. In the lower-left corner, we provide the reddening vector, adopting  $R_V = 3.1$ .

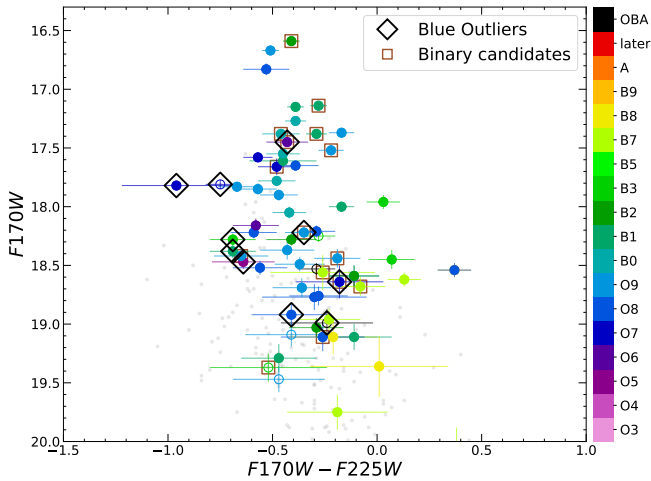


**Figure 8.** UV CMD of Sextans A, displaying [Bianchi et al. \(2012\)](#)’s catalogue in grey and our sample OB stars colour-coded according to their spectral type. Binary candidates are marked with brown squares and the blue outliers with black diamonds.

are collected in Table 4. Six objects in our list of blue outliers present line profiles broader than fast-rotating models. We caution, however, that the broadening may also be due to blends or unresolved binary systems.

We venture a classification for the blue outliers in Table 4, based on their spectral type, luminosity, UV excess, tentative  $v \sin i$  and possible companion. Nonetheless, we remark that follow-up observations with higher resolution and S/N are strongly needed to measure rotational velocities and He abundances that may support any of these scenarios.

## 6 SUMMARY AND CONCLUSIONS

Very low metallicity massive stars hold the key to interpreting processes from the earliest times of the Universe, such as the re-

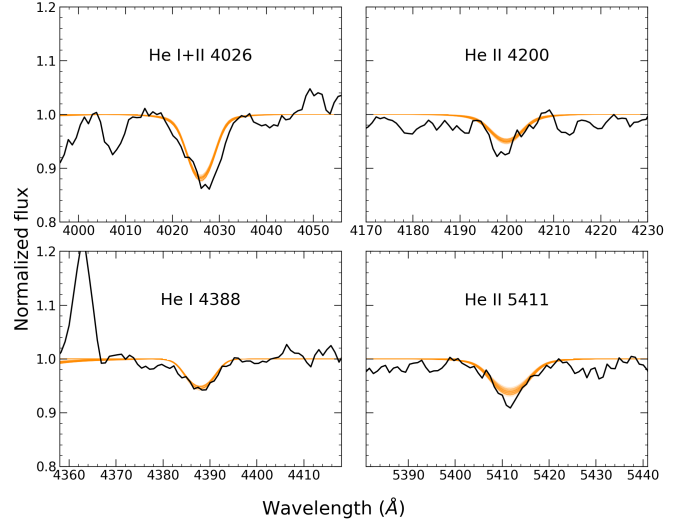


**Figure 9.** Comparison of the spectrum of the blue outlier s023 (O8 Vz), in black and smoothed for clarity, with FASTWIND models compatible with O8-type dwarfs (Lorenzo in prep.), convolved to the resolution of the spectrum ( $R \sim 1300$ ) and with the projected rotational velocity  $v \sin i = 300 \text{ km s}^{-1}$  (in orange).

ionization epoch and early cosmic chemical enrichment. Their low metal content may lead to significant changes in their evolution, some of them with an extreme impact on their ionizing fluxes like the chemically homogeneous evolution channel. In contrast with the extensive studies in the Magellanic Clouds (e.g. [Ramírez-Agudelo et al. 2017](#); [Sabín-Sanjulián et al. 2017](#); [Ramachandran et al. 2019](#)), current references for the metal-poor Universe, massive stars at sub-SMC metallicities were very poorly studied. Building an extensive census was a fundamental first step to understanding the physics and evolution of these objects, and to ultimately extrapolating the properties of the first, metal-free stars.

In this work, we present the results of a spectroscopic survey of massive stars in the  $1/10 Z_{\odot}$  galaxy Sextans A built with observations from the 10.4-m telescope GTC. Our 159 OB star catalogue is the largest census of massive stars at metallicities lower than the SMC to date. We also provide the first list of candidate stars undergoing chemically homogeneous evolution or systems hosting a stripped star. Confirming even one single case of these scenarios will have critical implications for the stellar evolution theories and the interpretation of high-redshift galaxies. In addition, we identify 33 sources within the sample displaying signs of multiplicity in their spectra.

Most of the sample OB stars are located in rich H I density regions producing large or small bubbles of ionized gas. However, we also find massive stars in inconspicuous areas of the galaxy where the column density of the neutral gas is low. This was already pointed out by [García et al. \(2019\)](#) in the south of Sextans A, but we also detect them in the gas-void galactic centre and other external areas of the galaxy. Our extensive spectroscopic sample and future detailed maps of gas will enable disentangling the roles of neutral and molecular gas in star formation at very low metallicity and identify the mechanisms that have triggered star formation in unexpected regions.

We find high scatter in the colour-magnitude diagram, hinting that the internal extinction of Sextans A is significant and non-uniform. Mapping the local reddening and estimating the stellar parameters and abundances of the massive stars of our catalogue by quantitative spectroscopic analyses is left for future work.

We have also assembled a sample of 38 BA supergiants that, with

**Table 4.** List of blue outliers in the CMD of Sextans A. Identification codes (ID), spectral types (SpT) and optical photometry from Massey et al. (2007) are provided. We also include the UV photometry from Bianchi et al. (2012) when available and flag the objects that are outliers in the UV CMD. The derived luminosities (calculated as indicated in the text) and the calibrated values for the corresponding spectral type are included. We also mark whether or not the source presents signatures of multiplicity in its spectra and if its line profiles are broader than models with  $v \sin i > 300 \text{ km s}^{-1}$ . Armed with this information, we tentatively assign the objects into a category in column *Suggested type*.

ID	SpT	Optical phot.		UV phot.			log ( $L/L_{\odot}$ ) This work	log ( $L/L_{\odot}$ ) Calibrated	Binary cand.	Broad lines	Suggested type
		V	B - V	UV detection	F170W	F170W - F225W					
s002	O4 Vz	20.369	-0.279	no info	-	-	5.60	5.67	no	no	?
s004	O5 III	20.917	-0.277	no info	-	-	5.34	5.73	yes	no	Stripped star
s005	O5 V((fc))	21.751	-0.364	yes	18.47	-0.64	4.83	5.49	no	no	Stripped star
s007	O6 V	20.515	-0.280	yes	17.45	-0.43	5.44	5.32	yes	yes	CHE or OB + stripped star
s009	O7 V	20.659	-0.285	yes	17.82	-0.96	5.30	5.14	no	no	OB + stripped star
s013	O7.5 III	21.532	-0.295	no info	-	-	4.87	5.42	no	yes	CHE
s015	O7.5 V + B?	22.259	-0.410	yes	18.64	-0.18	4.50	5.05	yes	no	Stripped star
s018	O8 III	21.092	-0.321	no info	-	-	4.97	5.35	no	yes	CHE
s023	O8 V	20.288	-0.299	no info	-	-	5.36	4.96	no	yes	OB + stripped star
s030	O8.5 III	21.008	-0.322	no info	-	-	4.94	5.28	no	yes	CHE
s032	O8.5 V	21.216	-0.326	no info	-	-	4.86	4.86	no	yes	CHE
s033	O8.5 V	21.654	-0.271	yes	18.92	-0.41	4.83	4.86	no	no	?
s040	O9 III + mid-B?	21.285	-0.311	yes	18.22	-0.35	4.83	5.21	yes	?	?
s063	B0 III	20.727	-0.295	yes	-	-	4.95	4.98	no	no	?
s080	B1 III	21.471	-0.292	yes	18.38	-0.69	4.50	4.72	no	no	?
s101	B3 III	21.254	-0.328	yes	18.28	-0.69	4.18	3.90	no	no	?
s129	O V + neb	21.237	-0.310	yes	17.81	-0.75	3.85	4.68	no	?	Stripped star
s164	OBA	22.253	-0.436	yes	18.99	-0.24	3.13	-	no	?	?

further quantitative analyses, will yield the abundances of  $\alpha$ - and Fe-group elements. Studying the chemical composition of blue stars will help us investigate the possible existence of chemical abundance variations across the galaxy and will shed light on the chemodynamical evolution of Sextans A.

In addition, we observed 4 late-type stars in the galaxy. Enhancing the statistics of evolved massive stars in LG galaxies allows us to quantify the role of metallicity in evolution.

This work presents the first extensive sample of sub-SMC metallicity massive stars. This catalogue is a fundamental first step for high-quality, high-resolution spectroscopic observations that will enable a thorough characterisation of stellar and wind properties of very metal-poor massive stars. These, in turn, will constrain stellar evolutionary models leading to more realistic predictions of stellar feedback for these stars, which is fundamental to interpreting observations of high-redshift galaxies.

## ACKNOWLEDGEMENTS

M. Lorenzo, M. Garcia and F. Najarro gratefully acknowledge support by grants PID2019-105552RB-C41 and MDM-2017-0737 Unidad de Excelencia "María de Maeztu"-Centro de Astrobiología (CSIC-INTA), funded by MCIN/AEI/10.13039/501100011033. M. Lorenzo acknowledges funding from grant PRE2019-087988 under project MDM-2017-0737-19-3, and by "ESF Investing in your future". A. Herrero acknowledges support by the Spanish MCI through grant PGC-2018-0913741-B-C22 and the Severo Ochoa Program through CEX2019-000920-S. M. Cerviño acknowledges financial support from the Spanish MCI through grant PID2019-107408GB-C41. N. Castro gratefully acknowledges funding from the Deutsche Forschungsgemeinschaft (DFG) – CA 2551/1-1.

The work has made use of the GTCMOS pipeline for the reduction of the GTC/OSIRIS spectroscopic data for which we thank its author Divakara Mayya. It also has made use of "Aladin sky atlas" developed at CDS, Strasbourg Observatory, France (Bonnarel et al. 2000; Boch & Fernique 2014); SIMBAD database, operated at CDS, Strasbourg, France (Wenger et al. 2000); and NASA's Astrophysics Data System Bibliographic Services.

Finally, we want to thank our colleagues at the *IAU Symposium 361: Massive Stars Near and Far* for their insightful questions and comments.

## DATA AVAILABILITY

The data underlying this article will be shared on reasonable request to the corresponding author.

## REFERENCES

- Balona L. A., 1994, *MNRAS*, **268**, 119  
 Beasor E. R., Davies B., Smith N., Bastian N., 2019, *MNRAS*, **486**, 266  
 Berg D. A., et al., 2012, *ApJ*, **754**, 98  
 Bianchi L., Efremova B., Hodge P., Massey P., Olsen K. A. G., 2012, *AJ*, **143**, 74  
 Boch T., Fernique P., 2014, in Manset N., Forshay P., eds, *Astronomical Society of the Pacific Conference Series* Vol. 485, *Astronomical Data Analysis Software and Systems XXIII*. p. 277  
 Bonnarel F., et al., 2000, *A&AS*, **143**, 33  
 Bresolin F., Pietrzyński G., Urbaneja M. A., Gieren W., Kudritzki R.-P., Venn K. A., 2006, *ApJ*, **648**, 1007  
 Bresolin F., Urbaneja M. A., Gieren W., Pietrzyński G., Kudritzki R.-P., 2007, *ApJ*, **671**, 2028  
 Britavskiy N. E., Bonanos A. Z., Mehner A., García-Álvarez D., Prieto J. L., Morrell N. I., 2014, *A&A*, **562**, A75  
 Britavskiy N. E., Bonanos A. Z., Mehner A., Boyer M. L., McQuinn K. B. W., 2015, *A&A*, **584**, A33  
 Britavskiy N. E., et al., 2019, *A&A*, **631**, A95  
 Brott I., et al., 2011, *A&A*, **530**, A115  
 Camacho I., 2017, PhD thesis, Departamento de Astrofísica, Instituto de Astrofísica de Canarias  
 Camacho I., Garcia M., Herrero A., Simón-Díaz S., 2016, *A&A*, **585**, A82  
 Castro N., et al., 2008, *A&A*, **485**, 41  
 Cutri R. M., et al., 2003, *VizieR Online Data Catalog*, **p. II/246**  
 Dohm-Palmer R. C., Skillman E. D., Mateo M., Saha A., Dolphin A., Tolstoy E., Gallagher J. S., Cole A. A., 2002, *AJ*, **123**, 813  
 Dolphin A. E., et al., 2003, *AJ*, **126**, 187  
 Elias J. H., Frogel J. A., Humphreys R. M., 1985, *ApJS*, **57**, 91



- Evans C. J., Bresolin F., Urbaneja M. A., Pietrzyński G., Gieren W., Kudritzki R. P., 2007, *ApJ*, **659**, 1198
- Evans C., et al., 2015, arXiv e-prints, p. arXiv:1501.04726
- Evans C. J., et al., 2019, *A&A*, **622**, A129
- Gaia Collaboration et al., 2021, *A&A*, **649**, A1
- García M., 2018, *MNRAS*, **474**, L66
- García M., Herrero A., 2013, *A&A*, **551**, A74
- García M., Herrero A., Vicente B., Castro N., Corral L. J., Rosenberg A., Monelli M., 2009, *A&A*, **502**, 1015
- García M., Herrero A., Castro N., Corral L., Rosenberg A., 2010, *A&A*, **523**, A23
- García M., Herrero A., Najarro F., Camacho I., Lennon D. J., Urbaneja M. A., Castro N., 2017, in Eldridge J. J., Bray J. C., McClelland L. A. S., Xiao L., eds, Vol. 329, The Lives and Death-Throes of Massive Stars. pp 313–321 (arXiv:1703.00218), doi:10.1017/S1743921317003088
- García M., Herrero A., Najarro F., Camacho I., Lorenzo M., 2019, *MNRAS*, **484**, 422
- García M., et al., 2021, *Experimental Astronomy*, **51**, 887
- Gil de Paz A., et al., 2005, *ApJ*, **619**, L115
- Gómez-González V. M. A., Mayya Y. D., Rosa-González D., 2016, *MNRAS*, **460**, 1555
- Götberg Y., de Mink S. E., Groh J. H., 2017, *A&A*, **608**, A11
- Götberg Y., de Mink S. E., Groh J. H., Kupfer T., Crowther P. A., Zapartas E., Renzo M., 2018, *A&A*, **615**, A78
- Gray R. O., Corbally Christopher J., 2009, *Stellar Spectral Classification*
- Groh J. H., et al., 2019, *A&A*, **627**, A24
- Hammer F., et al., 2014, in Ramsay S. K., McLean I. S., Takami H., eds, Society of Photo-Optical Instrumentation Engineers (SPIE) Conference Series Vol. 9147, Ground-based and Airborne Instrumentation for Astronomy V. p. 914727, doi:10.1117/12.2055148
- Herrero A., García M., Uytterhoeven K., Najarro F., Lennon D. J., Vink J. S., Castro N., 2010, *A&A*, **513**, A70
- Holtzman J. A., Afonso C., Dolphin A., 2006, *ApJS*, **166**, 534
- Hosek Matthew W. J., et al., 2014, *ApJ*, **785**, 151
- Hunter D. A., et al., 2012, *AJ*, **144**, 134
- Kaufer A., Venn K. A., Tolstoy E., Pinte C., Kudritzki R.-P., 2004, *AJ*, **127**, 2723
- Kehrig C., Vilchez J. M., Pérez-Montero E., Iglesias-Páramo J., Brinchmann J., Kunth D., Durret F., Bayo F. M., 2015, *ApJ*, **801**, L28
- Kippenhahn R., 1969, *A&A*, **3**, 83
- Kniazev A. Y., Grebel E. K., Pustilnik S. A., Pramskij A. G., Zucker D. B., 2005, *AJ*, **130**, 1558
- Kubátová B., et al., 2019, *A&A*, **623**, A8
- Levesque E. M., Massey P., 2012, *AJ*, **144**, 2
- Lindgren L., et al., 2021, *A&A*, **649**, A2
- Madau P., Dickinson M., 2014, *ARA&A*, **52**, 415
- Maeder A., Meynet G., 2000, *A&A*, **361**, 159
- Mandel I., de Mink S. E., 2016, *MNRAS*, **458**, 2634
- Marchant P., Langer N., Podsiadlowski P., Tauris T. M., Moriya T. J., 2016, *A&A*, **588**, A50
- Markova N., Puls J., 2008, *A&A*, **478**, 823
- Martins F., Schaerer D., Hillier D. J., 2005, *A&A*, **436**, 1049
- Massey P., 2003, arXiv e-prints, pp astro-ph/0307531
- Massey P., Olsen K. A. G., 2003, *AJ*, **126**, 2867
- Massey P., Hodge P. W., Jacoby G. H., King N. L., Olson K. A. G., Saha A., Smith C., 2000, in American Astronomical Society Meeting Abstracts. p. 113.02
- Massey P., McNeill R. T., Olsen K. A. G., Hodge P. W., Blaha C., Jacoby G. H., Smith R. C., Strong S. B., 2007, *AJ*, **134**, 2474
- McConnachie A. W., 2012, *AJ*, **144**, 4
- Mokiem M. R., et al., 2007, *A&A*, **465**, 1003
- Pilyugin L. S., 2001, *A&A*, **369**, 594
- Podsiadlowski P., Joss P. C., Hsu J. J. L., 1992, *ApJ*, **391**, 246
- Ramachandran V., et al., 2019, *A&A*, **625**, A104
- Ramírez-Agudelo O. H., et al., 2017, *A&A*, **600**, A81
- Renzo M., et al., 2019, *A&A*, **624**, A66
- Sabín-Sanjulián C., et al., 2017, *A&A*, **601**, A79
- Sander A., Hamann W. R., Todt H., 2012, *A&A*, **540**, A144
- Shenar T., et al., 2020, *A&A*, **641**, C2
- Shi Y., Armus L., Helou G., Stierwalt S., Gao Y., Wang J., Zhang Z.-Y., Gu Q., 2014, *Nature*, **514**, 335
- Skillman E. D., Terlevich R., Melnick J., 1989, *MNRAS*, **240**, 563
- Sobral D., et al., 2019, *MNRAS*, **482**, 2422
- Sota A., Maíz Apellániz J., Walborn N. R., Alfaro E. J., Barbá R. H., Morrell N. I., Gamen R. C., Arias J. I., 2011, *ApJS*, **193**, 24
- Szécsi D., Langer N., Yoon S.-C., Sanyal D., de Mink S., Evans C. J., Dermine T., 2015, *A&A*, **581**, A15
- Szécsi D., Agrawal P., Wunsch R., Langer N., 2022, *A&A*, **658**, A125
- Tammann G. A., Reindl B., Sandage A., 2011, *A&A*, **531**, A134
- Teich Y. G., et al., 2016, *ApJ*, **832**, 85
- Thatte N. A., et al., 2016, in Evans C. J., Simard L., Takami H., eds, Society of Photo-Optical Instrumentation Engineers (SPIE) Conference Series Vol. 9908, Ground-based and Airborne Instrumentation for Astronomy VI. p. 99081X, doi:10.1117/12.2230629
- Thatte N. A., et al., 2020, in Society of Photo-Optical Instrumentation Engineers (SPIE) Conference Series. p. 114471W, doi:10.1117/12.2562144
- Tramper F., et al., 2015, *A&A*, **581**, A110
- Walborn N. R., et al., 2002, *AJ*, **123**, 2754
- Wenger M., et al., 2000, *A&AS*, **143**, 9
- Wofford A., Vidal-García A., Feltre A., Chevallard J., Charlot S., Stark D. P., Herenz E. C., Hayes M., 2021, *MNRAS*, **500**, 2908
- Yoon S. C., Langer N., 2005, *A&A*, **443**, 643
- van Dyk S. D., Puche D., Wong T., 1998, *AJ*, **116**, 2341
- van Son L. A. C., et al., 2020, *ApJ*, **897**, 100

## APPENDIX

### APPENDIX A: OBSERVATION LOGS

This section collects the logs of our four observation campaigns, including the date and weather conditions and total exposure times (Tables [A1-A4](#)). In addition, we provide a list of the observing blocks and super-observing blocks coadded to generate the final spectrum of the stars observed in the MOS1 run (Table [A5](#)).

### APPENDIX B: SPECTRA

In this section, we provide the GTC-OSIRIS spectra of all our targets. We first show the spectra for the blue massive stars with a full classification (corresponding to Table [1](#)), then for the blue massive stars with no defined spectral subtype (Table [2](#)) and finally for the late type stars (Table [3](#)).

**Table A1.** MOS1 observing log.

Observing block	Date	Seeing (")	Transparency	Moon	Airmass	Exposure time (s)
OB01 (pre-image)	2 Apr 2014	0.8 - 1.0	Clear	Grey	1.29	-
OB02	16 Jan 2015	1.2	Clear	Dark	1.20	2950
OB03	3 May 2014	1.1	Photometric	Dark	1.24	2950
OB04	3 May 2014	1.2	Photometric	Dark	1.37	2950
OB05	4 May 2014	0.9	Clear	Grey	1.57	2950
OB06	5 May 2014	1.0	Clear	Grey	1.27	2950
OB07	5 May 2014	1.0	Clear	Grey	1.42	2950
OB08	5 May 2014	0.9	Clouds	Grey	1.72	2950
OB09	6 May 2014	1.0	Clear	Grey	1.29	2950
OB10	16 Jan 2015	1.0	Clear	Dark	1.26	2950
OB11	16 Jan 2015	0.9	Clear	Dark	1.39	2950
OB12	18 Jan 2015	1.1	Clear	Dark	1.20	2950
OB13	18 Jan 2015	0.8	Clear	Dark	1.25	2950
OB14	18 Jan 2015	0.8	Clear	Dark	1.39	2950

**Table A2.** MOS2 observing log.

Observing block	Date	Seeing (")	Transparency	Moon	Airmass	Exposure time (s)
Night-1	16 Feb 2018	0.9	Clear	Dark	1.20	12600
Night-2	17 Feb 2018	1.2	Clear	Dark	1.20	9000

**Table A3.** LSS2 observing log.

Observing block	Date	Seeing (")	Slit-width (")	Transparency	Moon	Airmass	Exposure time (s)
OB01	18 Feb 2020	1.0	1.2	Clear	Dark	1.23	2806
OB02	18 Feb 2020	1.0	1.2	Clear	Dark	1.20	2806
OB03	18 Feb 2020	1.3	1.2	Clear	Dark	1.28	2806
OB04	18 Mar 2020	0.9	1.2	Phot.	Dark	1.68	2806

**Table A4.** LSS3 observing log.

Observing block	Date	Seeing (")	Slit-width (")	Transparency	Moon	Airmass	Exposure time (s)
OB01	16 Jan 2021	1.0 - 1.2	1.2	Photometric	Dark	1.25	3600
OB06	16 Jan 2021	1.0 - 1.2	1.2	Photometric	Dark	1.20	3600
OB04	16 Jan 2021	1.3	1.2	Photometric	Dark	1.25	3600
OB05	16 Jan 2021	1.4	1.5	Photometric	Dark	1.41	3600
OB03	17 Jan 2021	0.8	0.8	Photometric	Dark	1.30	3788
OB02	17 Jan 2021	0.75	0.8	Photometric	Dark	1.20	3788
OB13	17 Jan 2021	0.8	1.0	Photometric	Dark	1.25	6846
OB17	17 Jan 2021	0.8	0.8	Photometric	Dark	1.75	5055
OB18	18 Jan 2021	0.8	0.8	Photometric	Dark	1.48	3804
OB15	18 Jan 2021	0.8	0.8	Photometric	Dark	1.21	6846
OB11	18 Jan 2021	0.8-1.0	1.0	Photometric	Dark	1.29	6846
OB44	19 Jan 2021	1.2-1.5	1.5	Photometric	Dark	1.25	4388
OB31	19 Jan 2021	1.5	1.2	Photometric	Dark	1.20	6225
OB45*	9 Mar 2021	1.3-1.4	1.2	Photometric	Dark	1.22	7125
OB46*	10 Mar 2021	1.3-1.5	1.2	Photometric	Dark	1.50	7125
OB47*	9 Mar 2021	1.3-1.5	1.2	Photometric	Dark	1.30	2883
OB49*	10 Mar 2021	1.3-1.5	1.2	Photometric	Dark	1.21	7125
OB50*	10 Mar 2021	1.3-1.5	1.2	Photometric	Dark	1.35	3704

**Notes.** (\*) observing blocks performed in service mode.

**Table A5.** List of the observing blocks and super-observing blocks coadded to generate the final spectrum of each star observed in the MOS1 run.

ID	Exposure time (s)	Exposures
s003	26550	OB02, sOB03(=OB03+OB04), OB05, OB06, OB10, sOB13(= OB12+OB13+OB14)
s004	26550	OB02, OB03, OB04, OB05, OB06, OB07, OB10, OB12, OB13
s028	26550	OB02, OB03, OB05, OB06, OB07, OB10, OB12, OB13, OB14
s029	26550	OB02, OB03, OB04, OB05, OB06, OB07, OB10, OB12, OB13
s041	26550	OB02, OB03, OB04, OB05, OB06, OB07, OB10, OB12, OB13
s042	23600	OB02, OB03, OB04, OB06, OB10, OB12, OB13, OB14
s061	32450	OB02, OB03, OB04, OB05, OB06, OB07, OB10, OB11, OB12, OB13, OB14
s063	20650	OB02, OB03, OB04, OB10, OB11, OB12, OB13
s071	29500	OB02, OB03, OB04, OB05, OB06, OB07, OB10, OB12, OB13, OB14
s089	29500	OB02, OB03, OB04, OB06, OB07, OB10, OB11, OB12, OB13, OB14
s092	32450	OB02, OB03, OB04, OB05, OB06, OB07, OB09, OB10, OB12, OB13, OB14
s099	26650	OB02, sOB03(= OB03+OB04), OB05, OB06, OB10, sOB13(= OB12+OB13+OB14)



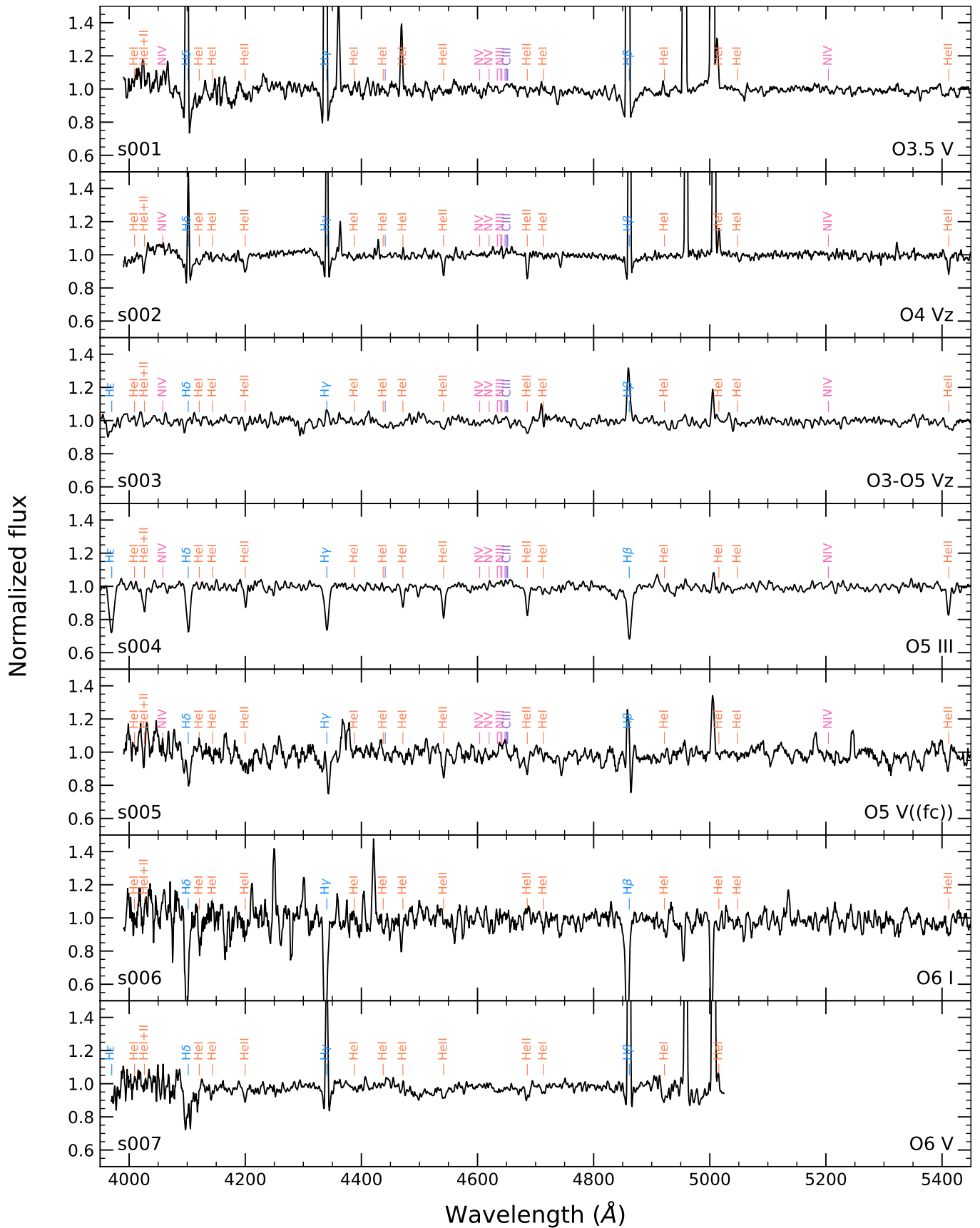


**Figure B1.** GTC–OSIRIS spectra of the blue massive stars of our catalogue with complete spectral classification. The data have been corrected by heliocentric and radial velocity, and smoothed for clarity based on the S/N of the spectrum.

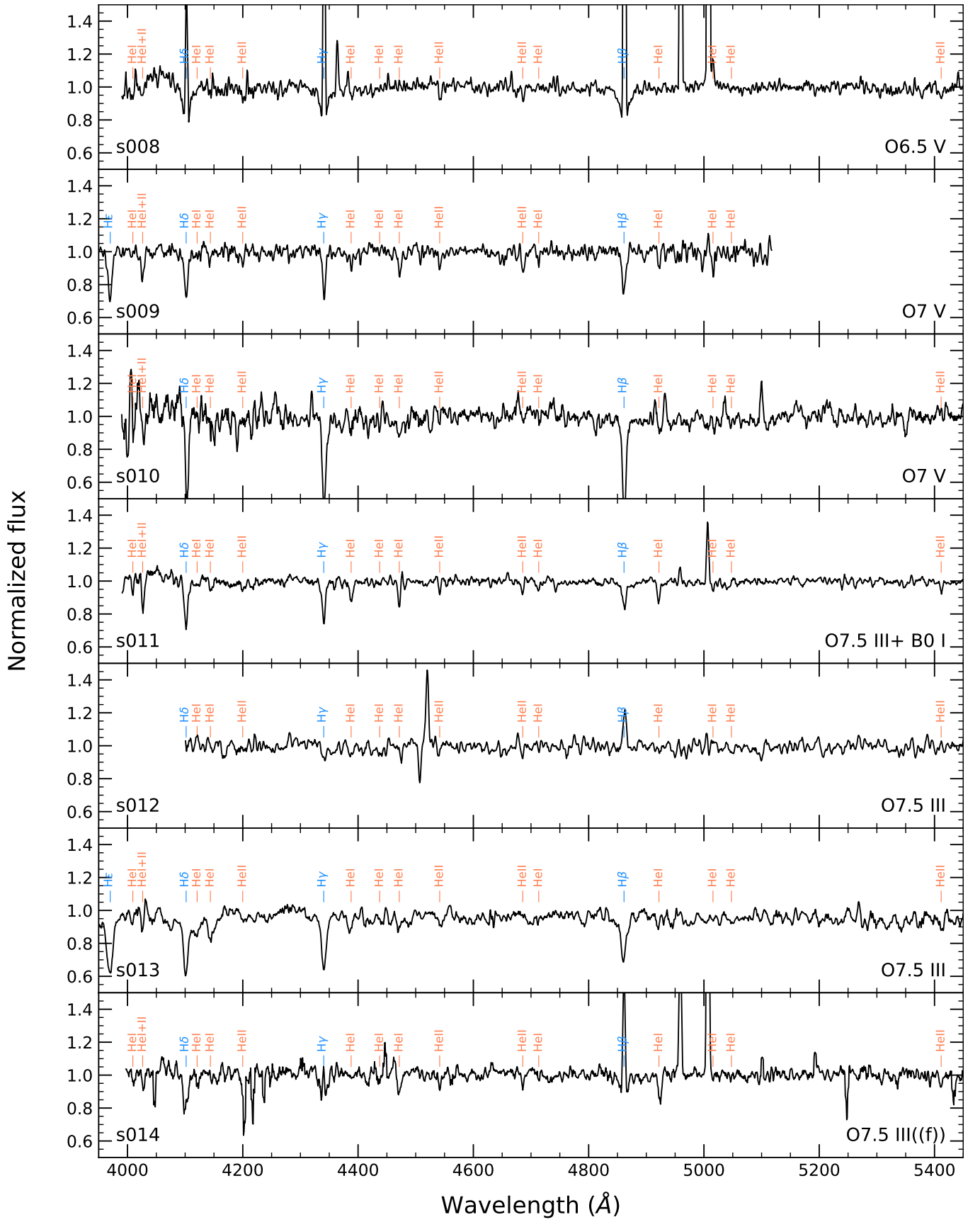


Figure B2. Same as Figure B1, continued.

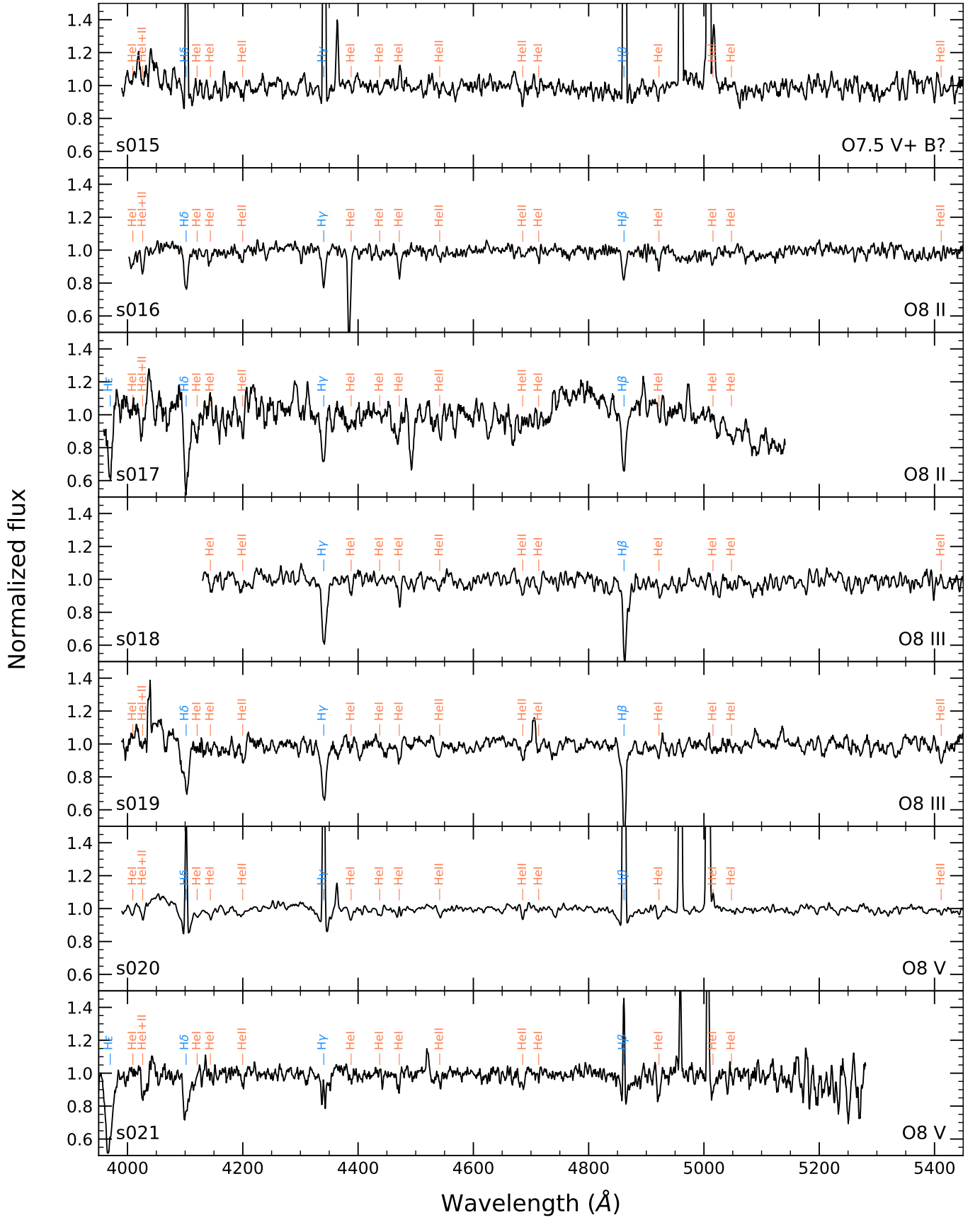


Figure B3. Same as Figure B1, continued.

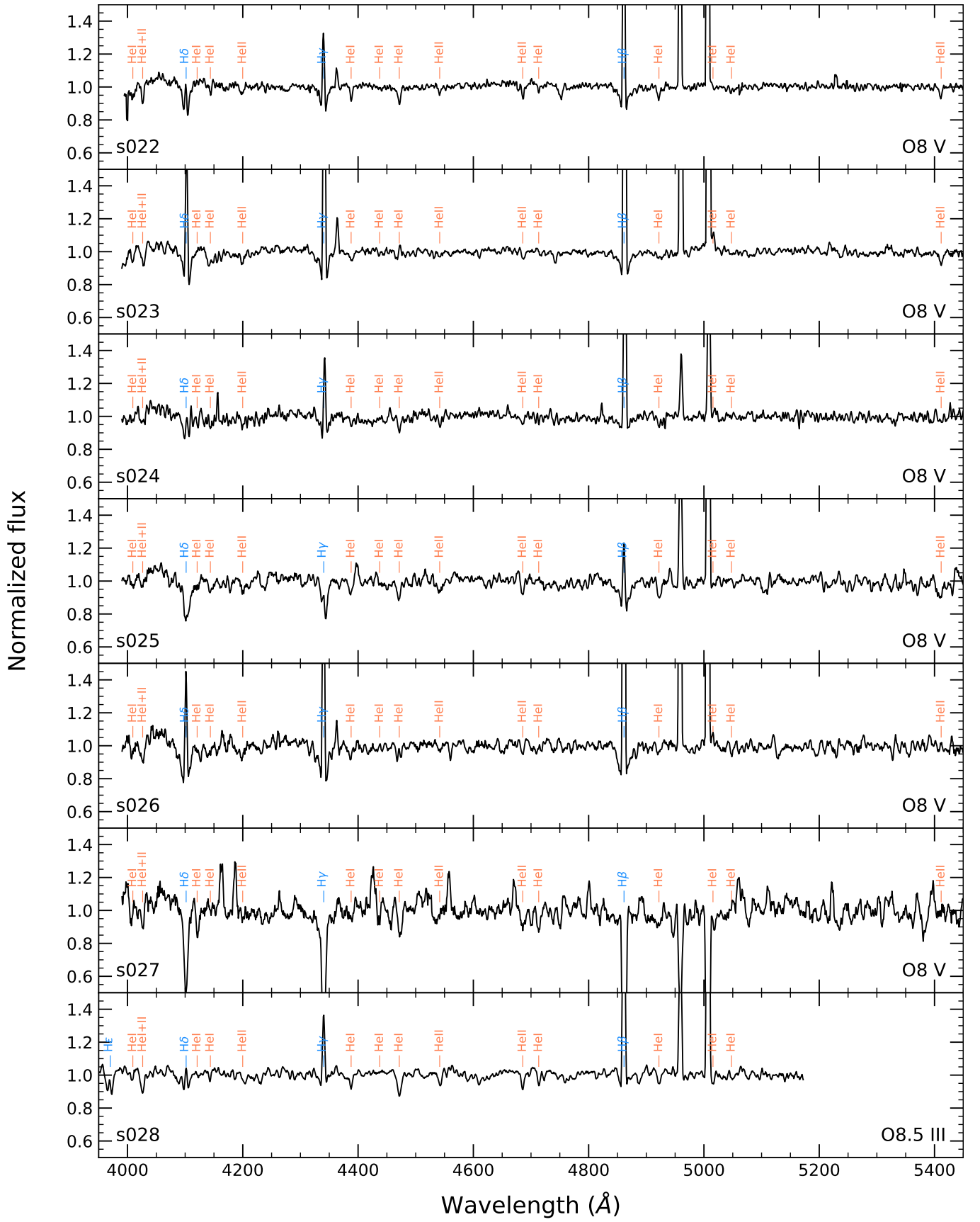


Figure B4. Same as Figure B1, continued.

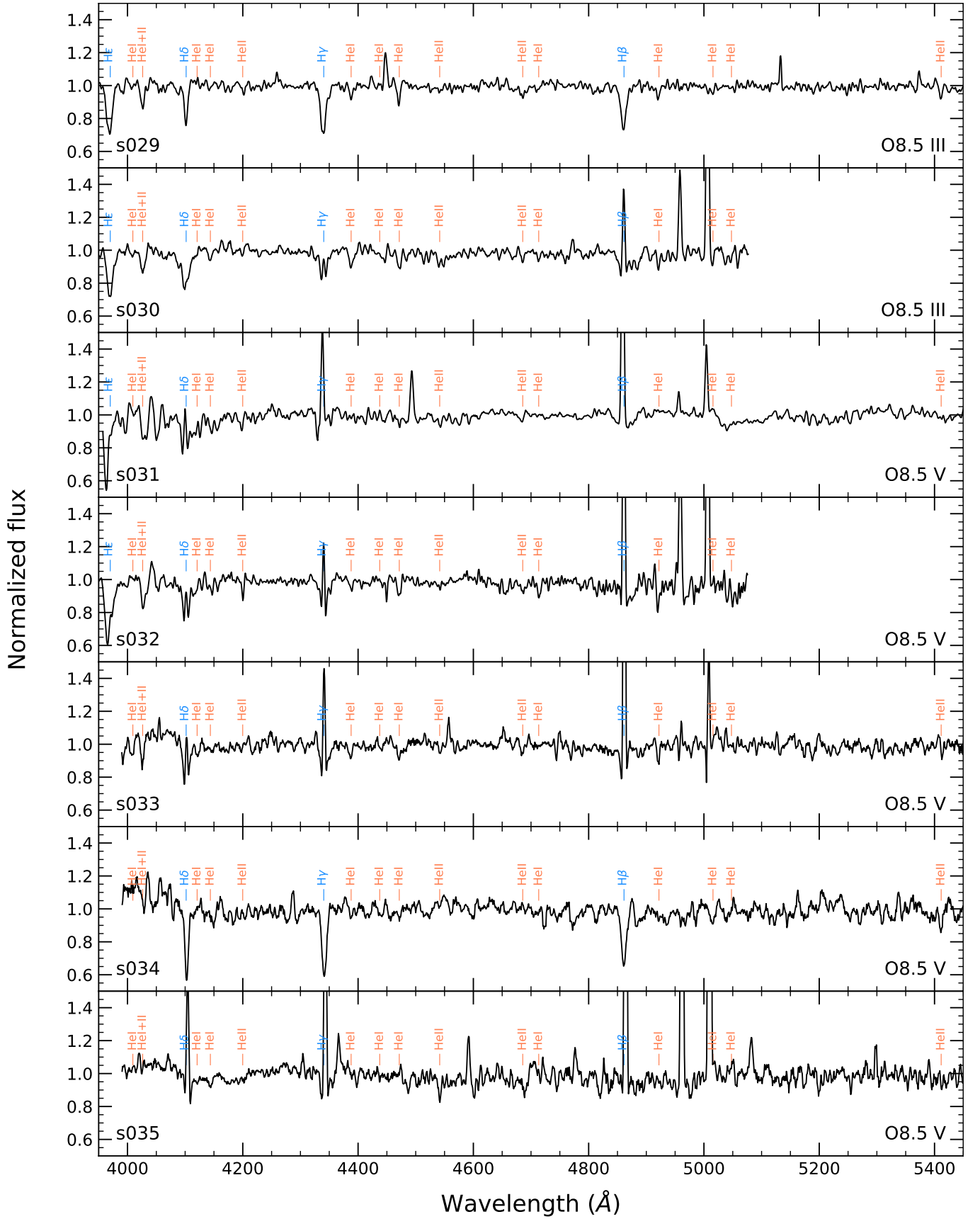
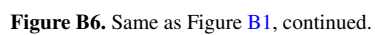
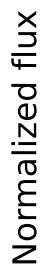


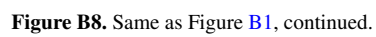
Figure B5. Same as Figure B1, continued.







**Figure B7.** Same as Figure B1, continued.



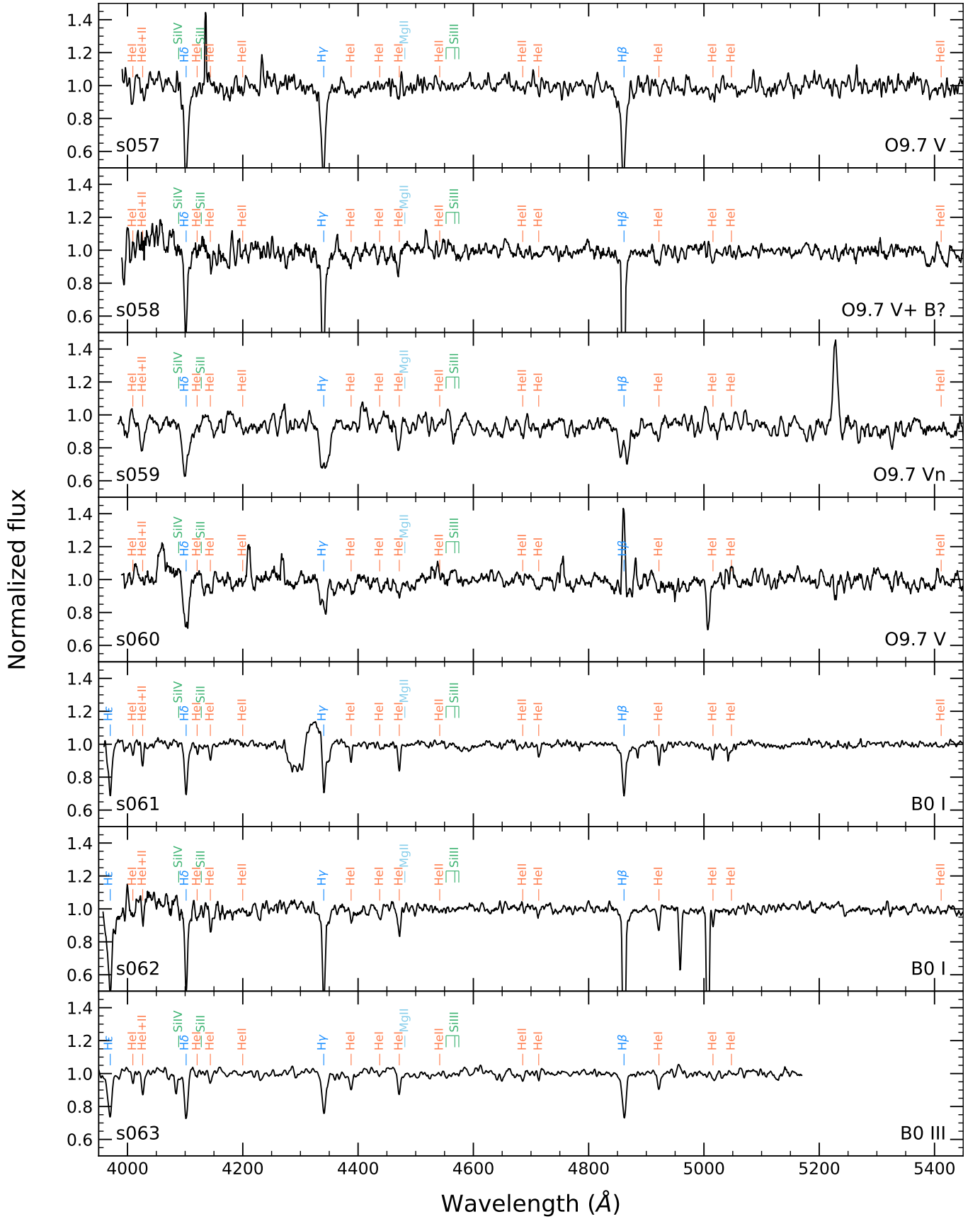
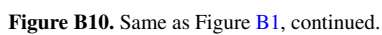
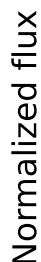


Figure B9. Same as Figure B1, continued.





**Figure B11.** Same as Figure B1, continued.



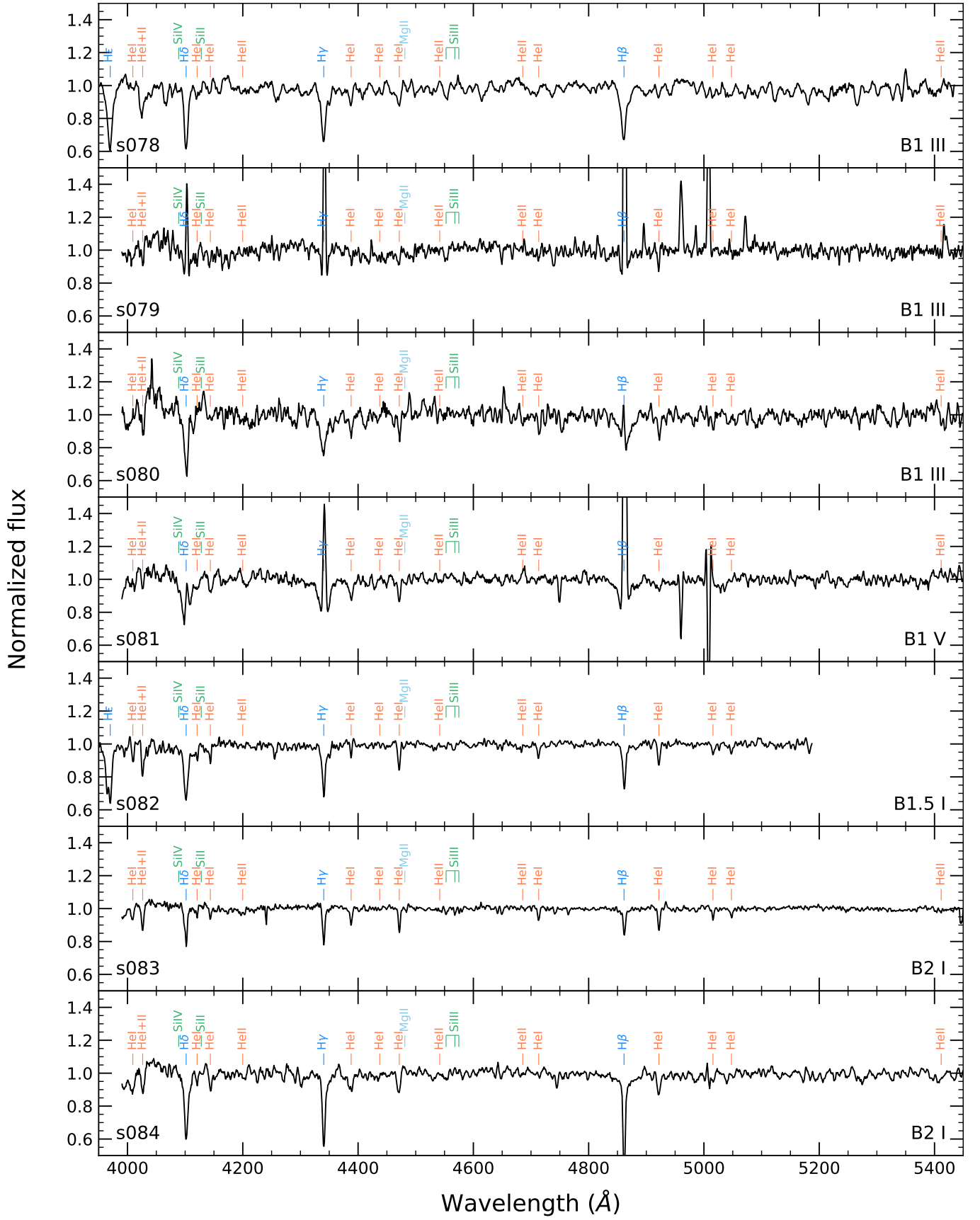


Figure B12. Same as Figure B1, continued.

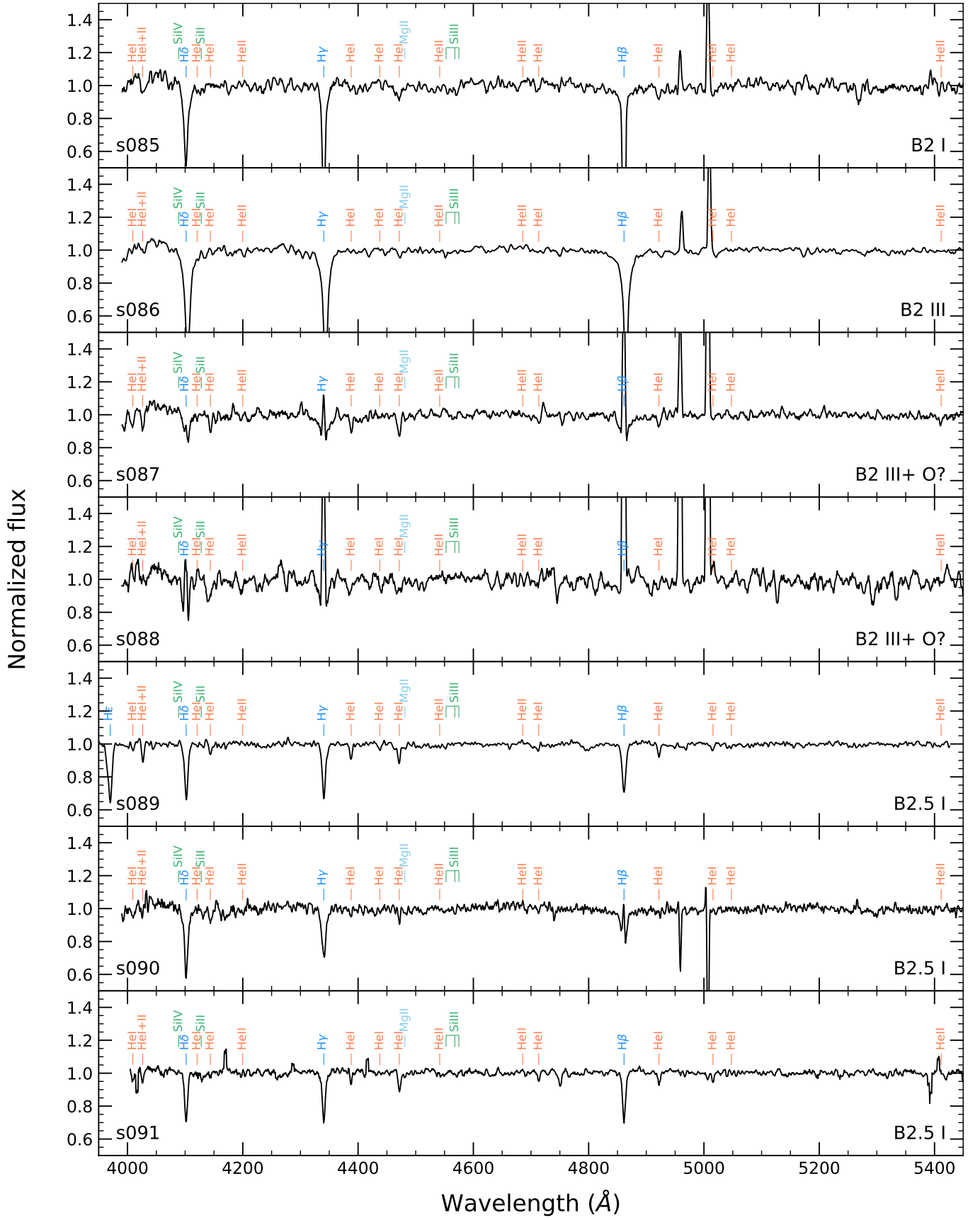


Figure B13. Same as Figure B1, continued.



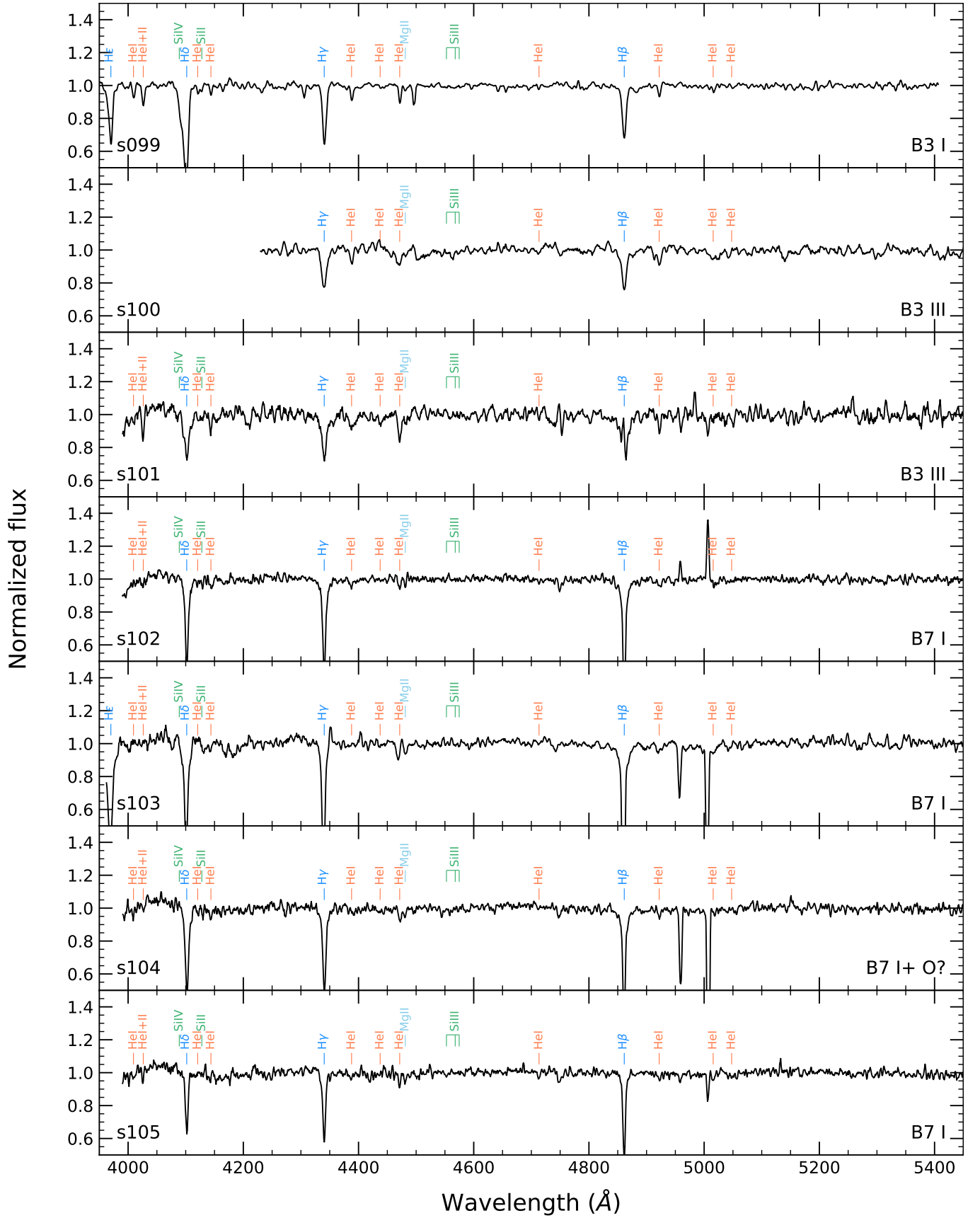


Figure B15. Same as Figure B1, continued.

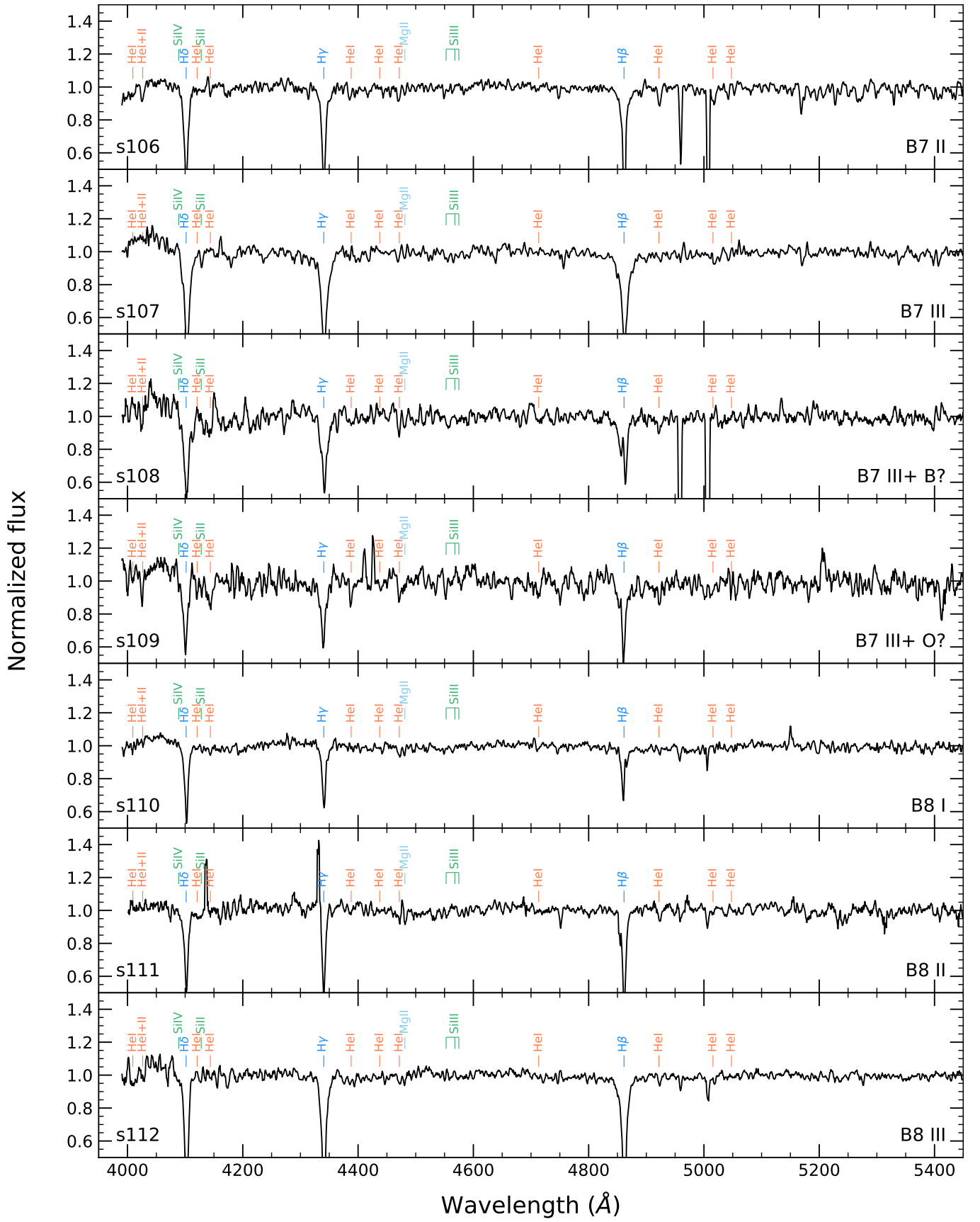
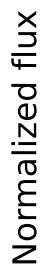
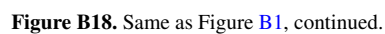


Figure B16. Same as Figure B1, continued.





**Figure B17.** Same as Figure B1, continued.



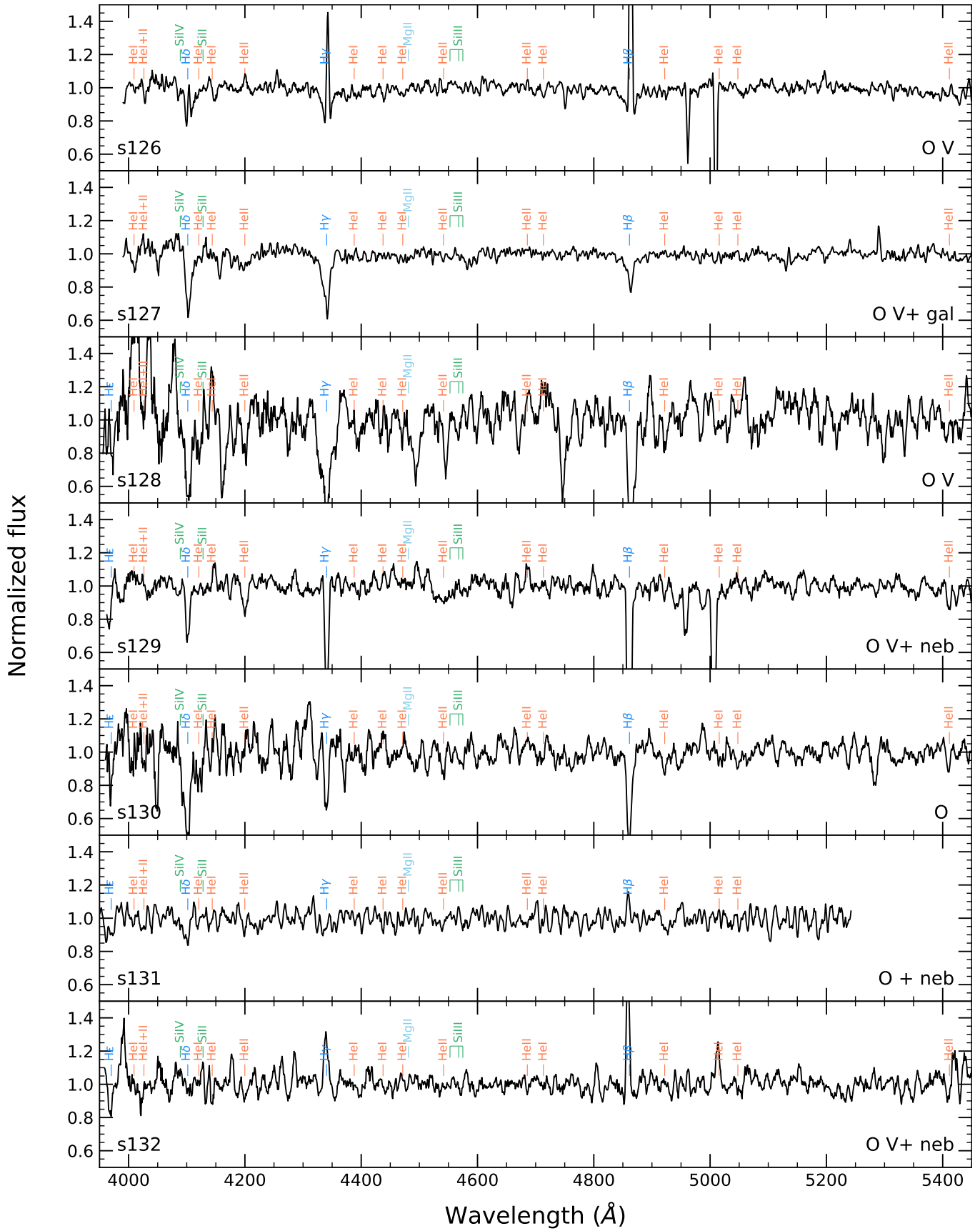


**Figure B19.** GTC–OSIRIS spectra of the sampled blue massive stars with no defined spectral subtype. The data have been corrected by heliocentric and radial velocity, and smoothed for clarity based on the S/N of the spectrum.

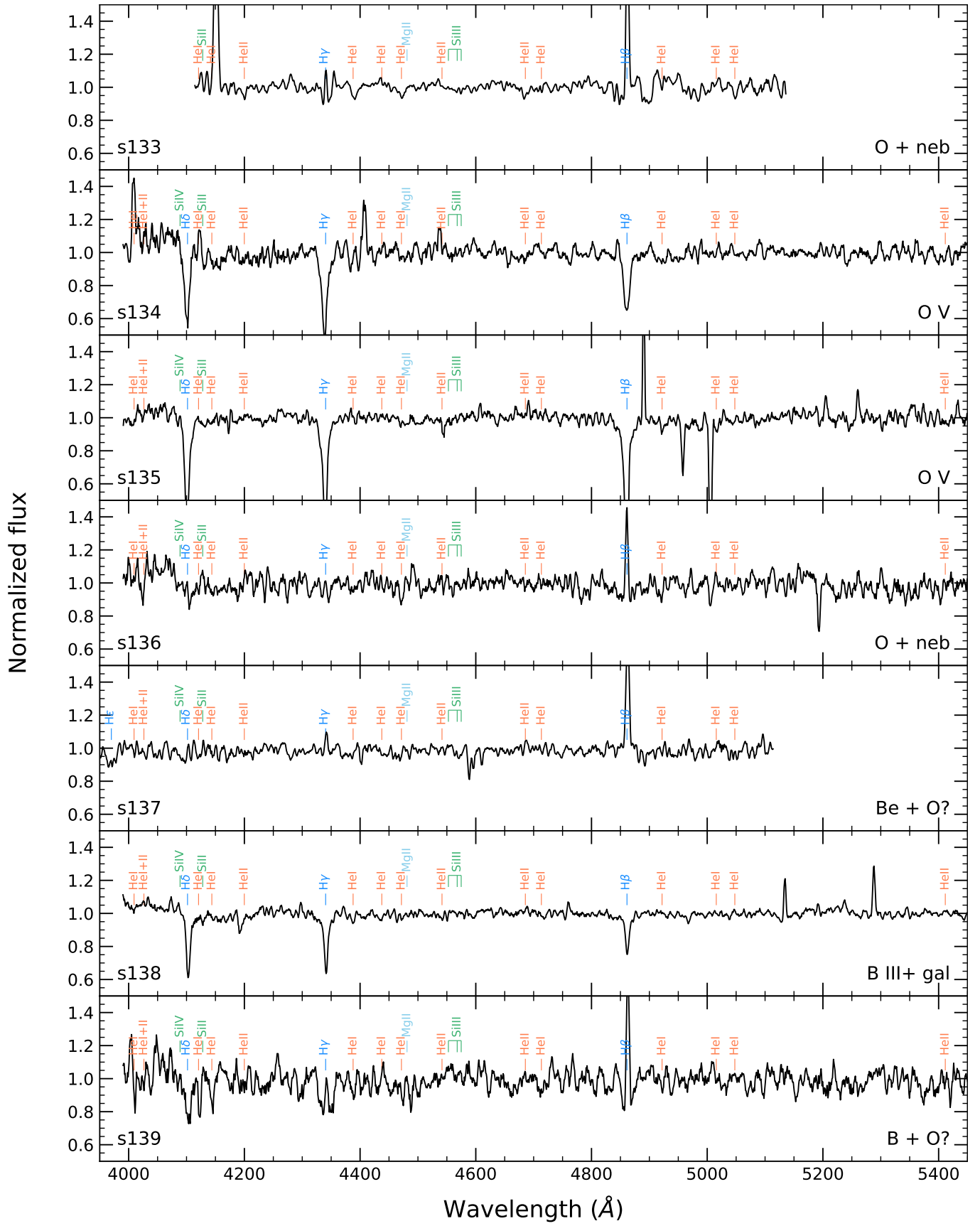


Figure B20. Same as Figure B19, continued.

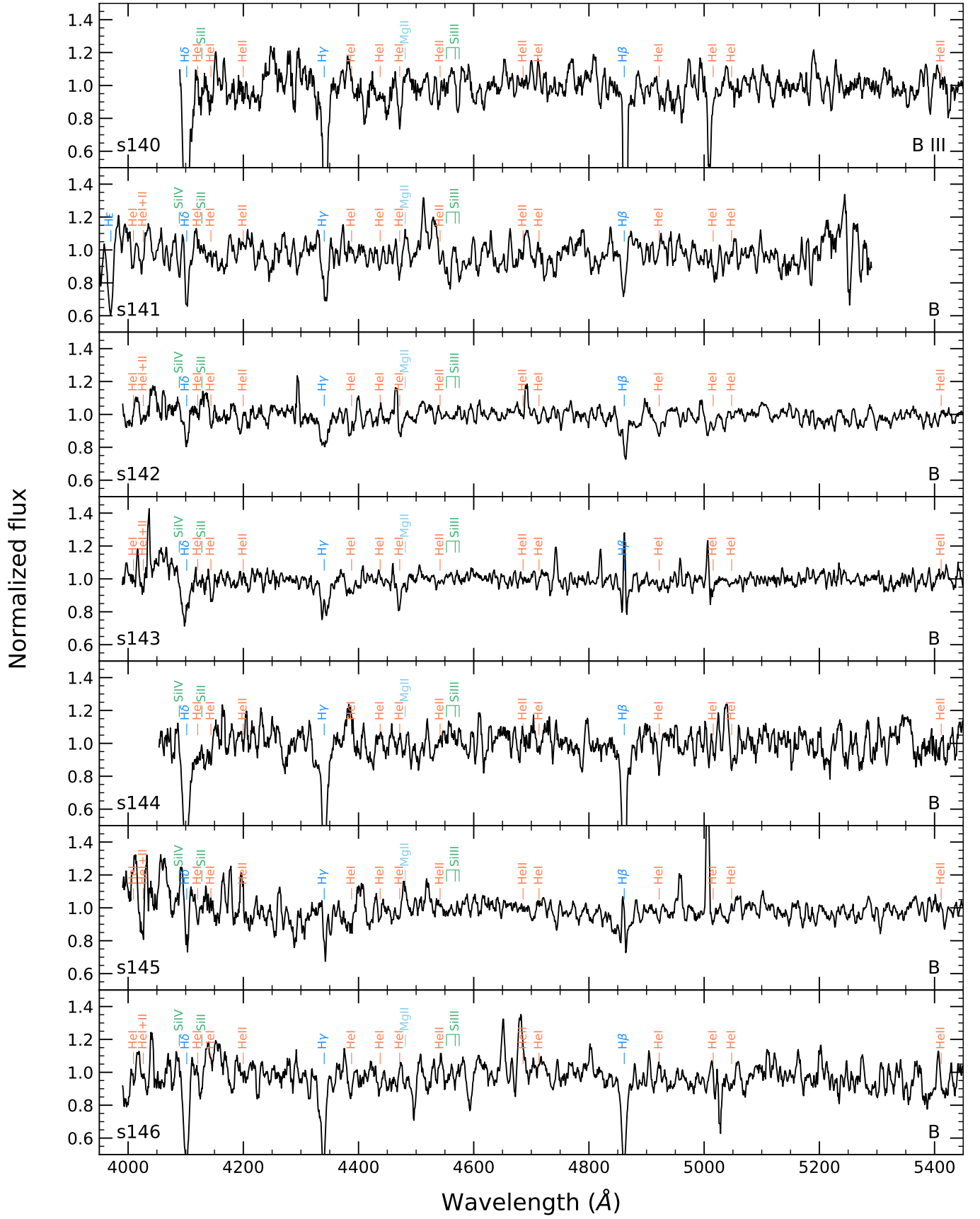
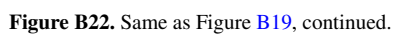
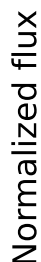


Figure B21. Same as Figure B19, continued.







**Figure B23.** Same as Figure B19, continued.

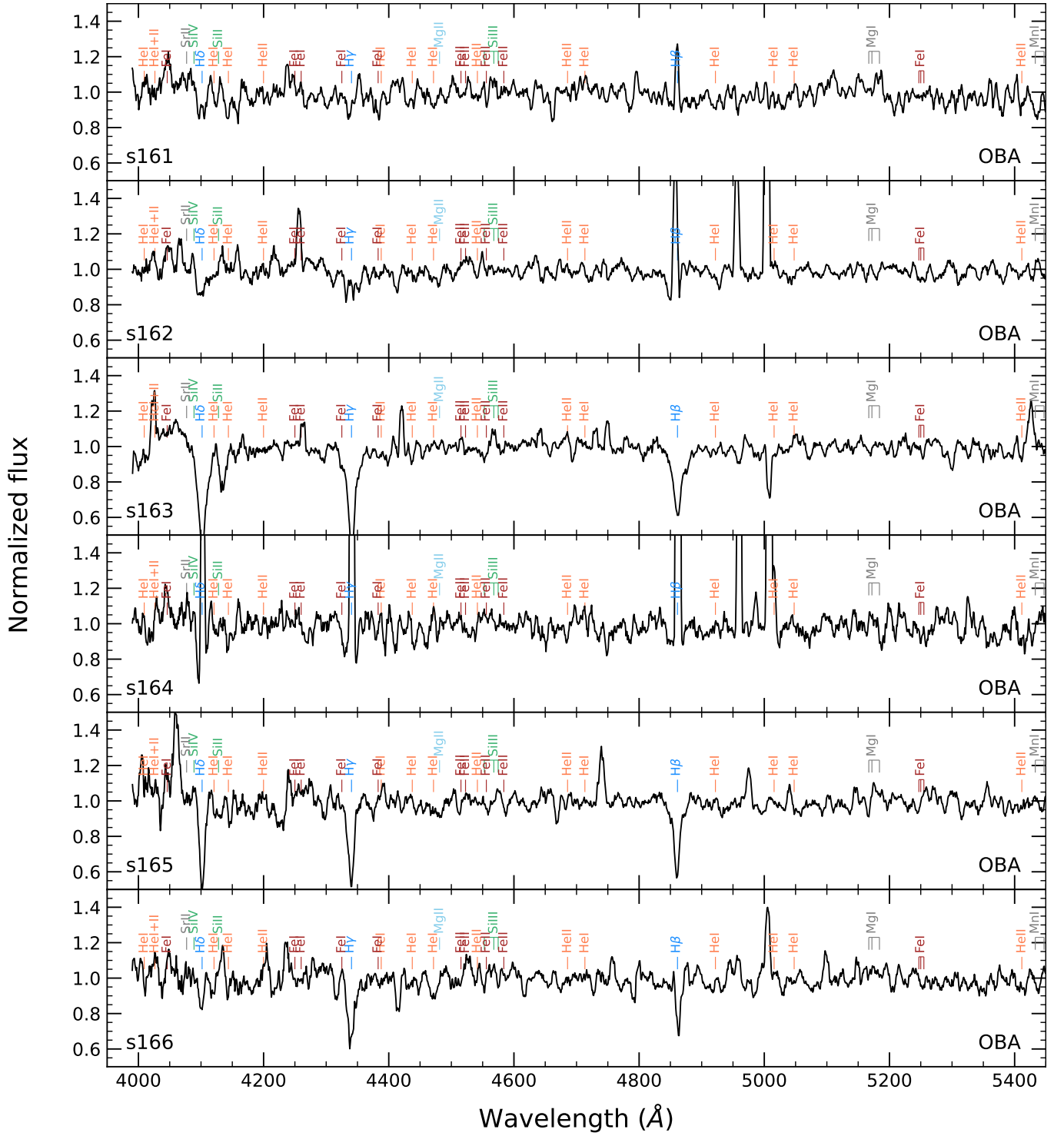
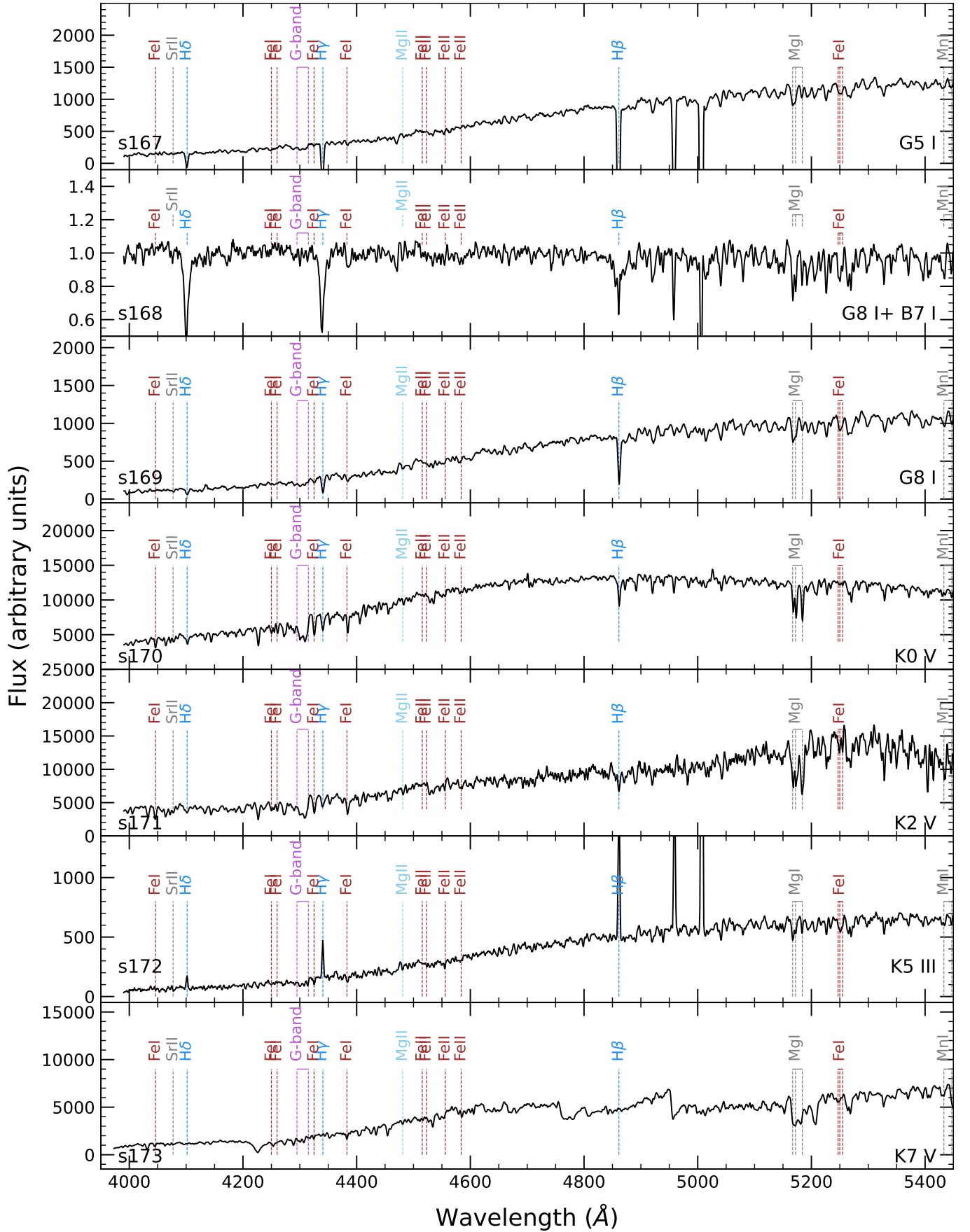
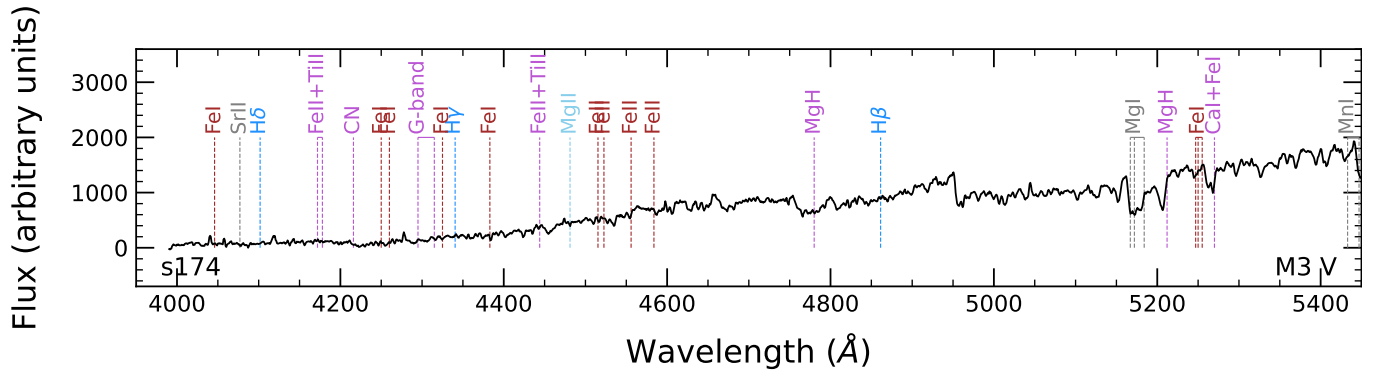


Figure B24. Same as Figure B19, continued.



**Figure B25.** GTC–OSIRIS spectra of the late type stars in the sample. The data have been smoothed for clarity, and corrected by heliocentric and radial velocity.



**Figure B26.** Same as Figure B25, continued.

## APPENDIX C: COMMENTS ON TARGETS

In this section, we provide information on individual stars regarding the observation and reduction procedure when it is needed to understand our spectral classification and the morphology of the given spectra. We also detailed the process of spectral classification when it is problematic or when the source presents interesting features.

## C1 Stars with a full classification

*s001 (O3.5 V):* The spectrum is dominated by nebular emission lines, although it displays stellar wings for the Balmer series. He II 4541 and He II 4686 are present, but we do not detect any He I lines. The star is classified as O3.5 V based on the tentative detection of N V 4604 in absorption. Class V is assigned based on the width of the Balmer lines. We also note that He II lines are weaker than expected, which may be due to the contamination from a nearby star that we detected at the reduction stage. The radial velocity was measured using He II lines, and we note the resulting value is not consistent with the core of the Balmer lines, hence we mark it as a possible binary.

*s002 (O4 Vz):* The spectrum displays high nebular contamination, He I 4471, He I 4920 and He I 5015 lines in emission and strong emissions at [OIII] 4363 Å, [OIII] 4959 Å and [OIII] 5007 Å, fitting the typical locus of the sky lines. It also presents strong absorption of He II lines. Since He I 4471 is hidden by the nebular contamination, we classify this star by comparing the depths of He II 4200, He I 4144 and He I 4121. As He II 4686 in absorption is stronger than He II 4541, we assigned Vz as its luminosity class.

*s003 (O3-O5 Vz):* This is star s2 in [Garcia et al. \(2019\)](#), who noted the broad He II lines and the absence of He I lines. The new reduction confirms the initial O3-O5 Vz spectral classification, further supported by the tentative detection of N III 4634, 4640–4642 in emission. The updated spectrum also shows H $\beta$  and H $\gamma$  in emission. However, a nebular or stellar origin cannot be discerned at the current resolution.

*s004 (O5 III):* This star was observed in two observing runs, MOS1 and MOS2, where no radial velocity variations were detected. The poorer S/N of the MOS2 observation prevented the co-addition of the two spectra. We reclassify the star with respect to [Garcia et al. \(2019\)](#) since the new reduction reveals stronger He II 4541. The luminosity class is reassigned to III based on the width of the Balmer lines, although He II 4686 is in strong absorption. We note the new classification makes the star even more underluminous for its spectral type than reported in [Garcia et al. \(2019\)](#).

We observe a  $v_{\text{rad}}$  mismatch between He I 4471 and He II 4541 in different observing blocks, and He I 4471 is not detected in OB03-OB06, so we mark the star as a possible binary.

*s005 (O5 V((fc))):* The spectrum presents an unidentified emission at 4375 Å, a very broad He II 4200 line and high nebular contamination shifted to the blue in the Balmer lines with respect to their cores. By comparing the strong absorption of He II 4541 with the He I 4471 line, we classify this star as O5. Nevertheless, this star might carry a later type since He I 4471 may be affected by nebular contamination. The very broad Balmer lines and the relative strength between He II 4686 and He II 4541 indicate a luminosity class of V. This star presents a counterpart in the UV which additionally

supports its O type. Lastly, due to the tentative presence of N III 4634 and C III 4647 in emission, we add the qualifier ((fc)).

*s006 (O6 I):* The star is classified as O6 due to the strong He II 4200 and He II 5411 lines. The spectrum is severely affected by nebular oversubtraction, which leads to a different radial velocity ( $v_{\text{rad}} = 300 \text{ km s}^{-1}$ ) for the Balmer lines and He I 4471 absorption. Since stellar Balmer wings are dominated by nebular oversubtraction and He II 4686 is not in absorption, luminosity class I is assigned.

*s007 (O6 V):* This source is the central star of one of the southeast bubbles of region-B. It was observed in a very short slit of MOS2, which made unfeasible the selection of sky boxes for *apall* background subtraction. The spectrum of one of the sky-slits was used instead, which results in a still incomplete nebular subtraction (see Balmer lines and He I 4471) and the loss of the bluest spectral range ( $\lambda \lesssim 4050 \text{ Å}$ ).

We detected a  $v_{\text{rad}}$  mismatch of  $\sim 70 \text{ km s}^{-1}$  between different OBs, corrected prior to co-adding the spectra. The main He II lines and some He I lines seem double in the raw spectra of Night-1, suggesting it could be a binary. However, we cannot discard that this may be due to central nebular contamination by incomplete nebular subtraction at the current resolution.

This star was also observed in run LSS2, which was used to recover the broader H $\delta$  profile, but it does not shed further information on the binary hypothesis.

*s008 (O6.5 V):* This source is a blend of two unresolved stars identified in [Bianchi et al. \(2012\)](#). The spectrum displays strong nebular contamination affecting the Balmer series and He I 4471. The He II lines are in strong absorption and their relative strengths with the He I lines (He I 4387 and He I 4144) suggest an O6.5 type. Since the Balmer series are broad, we assigned a dwarf luminosity class. The spectrum may be contaminated by nearby stars.

*s009 (O7 V):* This star was observed in two observing runs, MOS2 and LSS3. We did not detect any radial velocity variations, and we discarded the co-addition of the spectra since there was no S/N improvement. The spectrum is plotted with smooth equals to 3 for clarity purposes. Without it, the component of nebular oversubtraction can be cleaned from the He I 4471 core. This line is similar in strength to He II 4541, rendering type O7. Likewise, the feature around Mg II 4481 is revealed as an extremely wide absorption, unlikely to originate in a stellar spectrum, so it is not considered for classification. Luminosity class V is assigned based on the strong absorption of He II 4686, although the width of the Balmer lines suggests class III.

*s010 (O7 V):* The spectrum is very noisy and shows normalization issues. Spectral type of O7 is assigned based on the relative strength of He I 4471 and He II 4541. The adopted radial velocity is inconsistent with the Balmer series. He II 4686 in absorption suggest class V.

*s011 (O7.5 III + B0 I):* The spectrum shows strong He II lines, but also clear Si IV 4089 and perhaps Si III 4552 and Mg II 4481 lines. The target was observed in two different nights, but we have not detected changes in the spectral morphology or a radial velocity variation, hence we conclude that it is likely a blend of two stars. We assigned an O7.5 type to one of the stars based on the strength of its He II lines compared with FASTWIND models (Lorenzo et al. in prep.) and considering that the strong He I lines have contamination



from the other star. Since He II 4686 is present in absorption and its strength is similar to He II 4541, we assigned a giant luminosity class. Spectral type B0 I is assigned to the second star due to the presence of Si IV 4089 and its relative strength with respect to He I 4121.

*s012 (O7.5 III)*: This star was observed in a short slit with little room for the selection of sky boxes for sky subtraction. This problem is further exacerbated by the black column artefact from the adjacent slit. As a consequence, sky subtraction is very poor. We found that the best solution was to use only the spectrum observed during the second night. He I lines are wide, while He II lines are narrow, and their  $v_{\text{rad}}$  is slightly different. While it cannot be discarded that this is due to nebular oversubtraction, we mark the star as a possible binary. The spectral type was assigned on the premise that the He II lines are stellar.

*s014 (O7.5 III(f))*: This star shows indications of increased He abundance and strong winds (Camacho et al. 2016).

*s015 (O7.5 V + B?)*: The spectrum displays strong He II lines consistent with a radial velocity of  $v_{\text{rad}} \sim 225 \text{ km s}^{-1}$  and an O7.5 type. However, it also shows strong Si III 4552. In addition, the He I lines suggest a different radial velocity. Therefore, we mark the star as a possible SB2 with a possible B star companion.

*s018 (O8 III)*: The core of H $\beta$  and H $\gamma$  is dominated by over-subtracted nebular lines, which also affect the He I 4471 line.

*s019 (O8 III)*: This source is a blend of three stars included in the Bianchi et al. (2012)’s catalogue. We assign the photometry and ID of the brightest one. We clearly detect the Balmer series, some He I lines and strong He II lines. However, we note He I 4471 is affected by nebular contamination. We classify the star as an O8 type based on the ratio of He II 4541 and He I 4387, the strength of He II 4200 and the presence of He II 5411. We assign luminosity class III because of the similar strength of He II 4541 and He II 4686.

*s020 (O8 V)*: Strong nebular contamination affecting the Balmer series, He I 4471 and some other He I lines. The spectrum displays He II lines. The relative strength of He II 4541 with He I 4388 and He II 4200 with He I 4144 points to an O8 type. Since He II 4686 is present in absorption and the Balmer lines are wide, we assign a dwarf luminosity class.

Two spectra were taken for this star in two consecutive nights. The spectrum of the second night seems to lack the absorption of He II 4200 and He II 4541 (see Figure C1). Since the star is located in a crowded region we simply marked it as an SB2 candidate or blend. However, this could be a short period eclipsing binary. We do not detect radial velocity variations between observations.

*s021 (O8 V)*: This star was observed in a narrow 0.63’’ slit tilted from the N-S orientation by 3° in the MOS2 run. The slit was too short, compromising the selection of sky subtraction with *apall*. We used the sky spectrum of one of the sky-slits as it yielded better results. The star was also observed in the observing run LSS3, no radial velocity variations were detected between the two runs. We discarded the combination of the spectra since no improvement in the S/N on the resulting spectrum was detected.

This star is a UV bright source in Bianchi et al. (2012)’s catalogue with a nearby star undetected in the UV. Hubble Space Telescope resolves them fully at F555W, but Massey’s ground-based imaging

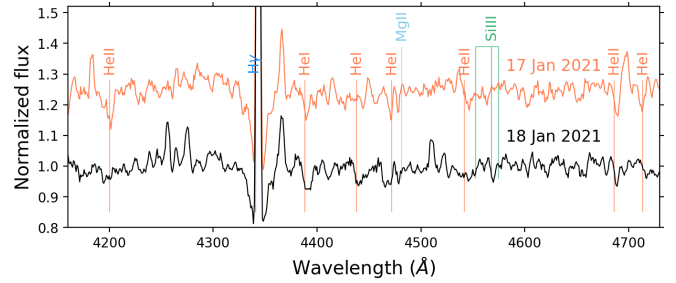


**Figure C1.** Observations of star s020 on two consecutive nights. We detect a change in the spectra features of the source. On the first night (in orange), He II 4200 is detected in strong absorption, while on the second night (in black) it appears extinct, suggesting a possible binary system.

could not separate them and provides one single detection for both. We included only the blue object in the slitlet, but some contamination is to be expected. In fact, the whole blend was included in the LSS3 run, and no significant difference is found between the spectrum of the MOS2 run and the blend, supporting the hypothesis that the source itself is also blended. There seems to be a mismatch between the radial velocities of He I and He II lines of  $\sim 80 \text{ km s}^{-1}$ , which could be caused by the blend or by nebular contamination at the core of the stellar lines.

*s022 (O8 V)*: This source was classified as O9.5 III-V by Camacho et al. (2016), but we reclassify it as an O8 V based on the strength of He II 4200 and He II 5411, consistently with the classification criteria of this paper. We note that the observed magnitude would instead suggest class I. HST photometry reveals this source is a blend of two stars identified in Bianchi et al. (2012).

*s023 (O8 V)*: Strong He II lines are detected. Since He I 4471 is in emission due to high nebular contamination, we based our classification on the strength of He II 4200, the presence of He II 5411 and the ratio of He II 4541 with He I 4388. The strong detection of He II 4686 and the lack of Si IV suggests a dwarf luminosity class. The spectrum could be contaminated by the nearby star s001.

*s024 (O8 V)*: Strong nebular contamination. The spectrum displays strong lines of He II. The relative strength of He II 4541 and He II 4200 with respect to He I 4471 and He I 4388 suggests an O8 type. We assign V as its luminosity class due to the broadening of the Balmer series and the presence of He II 4686 in absorption.

*s025 (O8 V)*: We detect He II lines. The relative strength of He II 4541 with He I 4471 and He I 4388, and the detection of He II 5411 points to an O8 type. Since He II 4686 is in strong absorption, we classify this star as dwarf.

*s026 (O8 V)*: This source is a blend of three stars identified in Bianchi et al. (2012)’s catalogue. We assign the photometry and ID of the brightest one. The spectrum displays strong, broad He II lines and extremely wide Balmer lines. The He I 4471 is strongly affected by nebular contamination. Based on the strength ratio of He II 4200 with respect to He I 4026, we classify the star as O8. We assign class V due to the broadening of the Balmer series and the strong He II 4686 absorption.

*s027 (O8 V)*: Noisy spectrum. We classify the star as O8 dwarf based on the strength of He II 4200 and He II 4686. However,

He II 4541 is absent. We also note that all He lines are very broad.

*s029 (O8.5 III):* This source is s03 in [Garcia et al. \(2019\)](#), but an updated reduction is presented in this work. The new spectrum shows an emission at 4450 Å due to a slit-ghost. He I 4471 seems double due to nebular contamination in some observing blocks but was not discarded in the classification, and He II 4541 is not seen in all the selected OBs. The target is marked as a possible SB1 since we detected radial velocity variations of more than 200 km s<sup>-1</sup> in He II 4541 between different OBs. These variations were corrected prior to co-adding the spectra of individual OBs. The updated spectrum exhibits HeII 4200 and HeII 5411, and narrower Balmer lines, hence the source is reclassified as O8.5 III.

*s030 (O8.5 III):* The slit was tilted by 7.1°, which results in moderate degradation of the spectral resolution. This star was observed in the same slit as s032. Targets are very close to each other, and some contamination is expected. The stars are located within an H II bubble and nebular subtraction was incomplete, as evinced by the core of the Balmer lines.

*s031 (O8.5 V):* This star was observed within a slit tilted by 8° to include also star s158. The inclination results in degraded spectral resolution. This star was close to the slit edge, and sky subtraction using a sky-slit provided better results than the other stars from the slit. Yet, nebular subtraction is not fully satisfactory, as demonstrated by the strong emission that overlaps the wide Balmer lines and the possibly nebular oversubtraction at the core of He lines. Spectral classification is further hindered by poor S/N as expected from the faint magnitude. The derived radial velocity is high, suggesting it may be a binary.

*s032 (O8.5 V):* This source encompasses two stars unresolved in [Massey et al. \(2007\)](#)'s catalogue, and it is possibly contaminated by s030, which is also in the same slit. The slit was tilted by 7.1°, which results in moderate degradation of the spectral resolution. For the second night, we found that the sky-slit provided better background subtraction, although that implies that  $\lambda < 4100$  Å can only be recovered from Night-1, and errors are larger. Despite this action, nebular subtraction is incomplete in the Balmer lines, and the He I lines display nebular oversubtraction at their cores.

*s033 (O8.5 V):* The spectrum shows strong nebular contamination. We assign an O8.5 type based on the relative strength of He II 4541 with He I 4471 and the presence of He II 5411. The detection of He II 4686 in absorption and the broad Balmer lines suggest a dwarf luminosity class.

*s034 (O8.5 V):* The spectrum displays He II 4541 that, compared with the He I 4471 line suggest an O8.5 type. He II 5411 is also detected. Based on the broadening of the Balmer series, we assign a luminosity class V, but we note that this is in contradiction with the absence of He II 4686 in absorption.

*s035 (O8.5 V):* At the assigned  $v_{\text{rad}}$  of 170 km s<sup>-1</sup>, we detect a strong absorption of He II 4541, partially affected by nebular oversubtraction. We classify the source as O8.5 due to the relative strength of He I 4144 and He II 4200. The Balmer series shows nebular contamination and seems inconsistent with the adopted  $v_{\text{rad}}$ .

*s036 (O9 I):* This star was observed in three observing runs, MOS2, LSS2 and LSS3. No variations in spectral features or radial

velocities were detected. In MOS2, it was included in a very short slit that hindered sky subtraction. In LSS2, the star was off-slit, and exposure times were shorter, yet the sky subtraction was slightly better. The He II 4541 transition is detected completely in emission in MOS2, but the stellar component is partially recovered in LSS2 and LSS3. After checking against the spectral lines, we co-added the spectra to increase the spectral S/N. We note that the He II 4541 line is lost in the co-added spectrum, but we used the LSS2 line strength for spectral classification. The strong absorption at 4650 Å is due to an artefact detected in MOS2 run, but not in the LSS2 or LSS3 runs.

*s037 (O9 I):* This star was observed in runs LSS1, MOS2 and LSS2. [Camacho et al. \(2016\)](#) classified this star, its OB623, as an O8 Ib. We detect no significant morphological or radial-velocity variations in the subsequent MOS2 and LSS2 runs. In MOS2, the spectrum was taken in a too-short slit that compromised the sky subtraction with *apall*. For the spectrum of the second night, with worse effective seeing, we instead used the sky spectrum from one of the sky-slits, although sky subtraction was incomplete. Sky subtraction in LSS2 is not fully satisfactory either. After checking against spectral variations, we co-added the LSS2 and MOS2 spectra to increase the S/N and discarded the LSS1 spectrum that only introduced noise in the co-addition.

The strong emission close to He II 4541 is remnant from the sky-spectrum and precludes the detection of He II 4541. This line is detected in absorption both in LSS1 and LSS2. Alternatively, He II 4200 is clearly observed in the co-added spectrum and He II 4686 is still neither detected in emission nor absorption, thus pointing to class I. Considering the strength of the He II 4200 and Si IV 4089 lines relative to He I transitions, we reclassify the star as O9 I.

*s038 (O9 I((f))):* This star was classified as O9.7 I((f)) by [Camacho et al. \(2016\)](#), who also noted indications of strong winds and increased He abundance. In this work, we reclassify the star as O9 I((f)) based on the strength of He II 5411 and He II 4200, more consistently with the current criteria.

*s039 (O9 III):* An unknown emission detected near He II 4200, at 4183 Å. The presence of He II 4541 and its relative strength with respect He I 4471 suggest an O9 type. The lack of He II 4686 points to a supergiant class, but the width of the Balmer series and the lack of Si IV suggest luminosity class III.

*s040 (O9 III + mid-B?):* The spectrum is noisy and presents significant nebular contamination. Because of the relative strength of He II 4200 with He I 4387, we assign an O9 type. The source also shows weak He II 4541 and He II 5411. The width of the Balmer lines and the relative strength of He II 4541 with He II 4686 points to the adopted class III, although the faint magnitude suggests class V. The Mg II 4481 and Si III 4552 absorptions would be consistent with a secondary component at  $v_{\text{rad}} = 300$  km s<sup>-1</sup> and mid-B spectral type. Space photometry from [Bianchi et al. \(2012\)](#) cannot resolve this source.

*s041 (O9.5 II):* This star was observed in two observing runs, MOS1 and MOS2, where no radial velocity variation was detected. The poorer S/N of the MOS2 observation prevented the co-addition of the two spectra.

*s042 (O9.5 III):* An emission at 4450 Å is only seen in the observing blocks taken in the first year (as in s029), and it may be

due to a slit-ghost. In addition, an anomalous sky line emission is detected at  $900 \text{ km s}^{-1}$  of H $\delta$  and H $\gamma$  in some observing blocks, which leads to an artificial broadening of the lines. He I 4471 was not considered for classification since it seems to be an artefact. Apart from the MOS1, the source was also observed in the LSS3 observing run, where He I 4471 has a much weaker absorption. No radial velocity variations were detected, but since the LSS3 spectrum has worse S/N and poorer spectral resolution, the spectra were not co-added. HST photometry reveals the source is a blend of two stars.

*s043 (O9.5 V):* The source is a blend of two unresolved stars identified in Bianchi et al. (2012). It was observed in the LSS2 and LSS3 observing runs, and we detected no radial velocity variation. Since the S/N of the LSS2 spectrum was poor, the data were not co-added. The spectrum shows strong lines of He I, perhaps He II 4200 and no metallic lines. The absorption found at  $\sim 4542 \text{ \AA}$  is an artefact of reduction. Based on the presence of He II 4200 and the width of the Balmer lines, we classify it as O9.5 V.

*s044 (O9.5 V):* He I 4471 is absent due to nebular contamination. We clearly detect the Balmer series, some He I lines, and He II 4541 and He II 4686 in absorption. We classify the star as an O9.5 dwarf due to the relative strength of He II 4541 with respect to He I 4387 and the width of the Balmer series. H $\gamma$ , H $\delta$  and He I 4471 show hints of a second component at higher radial velocity ( $\sim 600 \text{ km s}^{-1}$ ).

*s045 (O9.5 V):* The detection of He II 4200 and He II 4541 points to an O9.5 type. He I 4388 is anomalously broad. The star is classified as a dwarf because of the broadening of the Balmer wings. However, we note that this is in contradiction with the absence of He II 4686.

*s046 (O9.5 V):* This source is a blend of two unresolved stars identified in Bianchi et al. (2012). We classify it as O9.5 based on the relative strength of He II 4200/He II 4144 since He II 4541 seems to be affected by noise. Luminosity class V is assigned due to the width of the Balmer lines.

*s047 (O9.5 V):* We reclassify the star from an A5 II in Camacho et al. (2016) to an O9.5 V as we note the presence of He II 4686 and He II 4541.

*s048 (O9.5 Vn):* We classify the star as O9.5 based on the relative strength of He I 4471 and He II 4541. Luminosity class Vn is assigned due to the width of the Balmer lines.

*s049 (O9.7 I):* This source was observed in two observing runs, LSS2 and LSS3. We found a radial velocity variation of  $\sim 30 \text{ km s}^{-1}$  between the two runs. However, we did not co-add the spectra since we did not detect any improvement in the S/N. The spectrum shows He II 4541 and similarly strong Si III 4552, we assigned a compromise spectral type of O9.7 supergiant. HST photometry reveals this source is a blend of two unresolved stars identified in Bianchi et al. (2012).

*s050 (O9.7 I):* This star is OB321 in Camacho et al. (2016), where they assigned O9.7 I((f)). Since it is brighter than most of the MOS2 targets ( $V = 19.609 \text{ mag}$ ), it was observed in a narrow slit to increase resolution and constrain better its stellar parameters. The S/N of this spectrum is better than the LSS1 program, so we

replaced OB321 with this one in our database. N III 4634 does not exhibit emission in the improved quality spectrum, so we removed the ((f)) qualifier.

*s051 (O9.7 I):* This star was observed in LSS2 and MOS2 observing runs. We detect no radial velocity variations and discard the spectrum from the LSS2 run due to poor S/N.

*s052 (O9.7 I):* This star was observed together with in a very short slit. For the first night, we found that the subtraction of one of the sky-slits provided better results. For the second night, *apall* sky subtraction provided better results, but only one box was used (located in the middle of the slit). He II lines are clearly seen only in the spectrum of the second night, but we detected no apparent radial velocity variation between both nights.

*s053 (O9.7 I):* We detect radial velocity inconsistencies between different Balmer lines and different He I lines, which may be explained by nebular contamination. Adopting the systemic velocity of the galaxy, the presence of He II 4200 and lack of Si III 4552, Mg II 4481 and He II 4686 suggest an O9.7 I. The spectrum may be contaminated by the near star s070.

*s054 (O9.7 III):* The star was observed in both LSS2 and LSS3 runs. We did not detect radial velocity variations between the two observations, and we co-added the spectra to achieve higher S/N. Only He I lines are clearly detected. There might be hints of He II 4541, He II 4686 and Si IV 4089, hence we classify the star as O9.7. Luminosity class III is assigned due to the width of the Balmer series.

*s055 (O9.7 III):* The main star (J101053.90-044111.0) is contaminated by a nearby one with very blue  $Q$ -colour (J101053.94-044110.1) and only 0.2 mag fainter, slightly outside the slit. The selection of sky-boxes with *apall* was hampered by this source and, as a consequence, the nebular subtraction is incomplete, as seen clearly in the core of the Balmer lines, but also He II 4686. The emission at  $\sim 4540 \text{ \AA}$  that affects He II 4541 has an unknown origin and does not seem to be a cosmic ray.

*s056 (O9.7 V):* In the MOS2 run, this star was observed in a very short slitlet that severely handicapped sky subtraction (e.g. see the central nebular emission lines in Balmer and possibly He I oversubtraction). It was also observed in the MOS1 run, but nebular subtraction was similarly poor. Considering that the star is far from the large ionized structures of the galaxy, the strong nebular contamination is quite puzzling. Alternatively, the star could be an Oe star. After checking against spectral line or flux continuum level variations, we co-added the spectra for increased S/N. There is an absorption feature at  $\sim 4200 \text{ \AA}$  of unknown origin that is detected in the spectrum of both observing runs, making it unlikely for it to be an artefact. The subtracted sky spectrum was checked, and there are no features at those wavelengths. He II 4541 is present but weak, so the star is classified as O9.7. Luminosity class V is assigned based on the width of the Balmer lines. We note that He II 4686 should be strong in absorption in an O9.7 V but is missing in the spectrum of MOS2.

*s057 (O9.7 V):* This star was observed in LSS2 and LSS3 observing runs, where no radial velocity variations were detected. The spectra were co-added to improve S/N. We note the absence of He II 4686, in contradiction with the luminosity class Vn, indicated

by the Balmer wings.

*s058 (O9.7 V + B?):* Very noisy spectrum. The O9.7 type is assigned because of the presence of He II lines and Si III 4552. The strong He I lines at  $v_{\text{rad}} = 150 \text{ km s}^{-1}$  suggest a secondary component.

*s059 (O9.7 Vn):* This star is located in the galactic outskirts, and it is the farthest of the southern sources from the galactic centre. Contrastingly, it shows nebular lines at the core of the Balmer series and GALEX UV emission. We assign spectral type O9.7 based on the detection of He II 4686 in absorption. The modifier "n" is used because of the abnormally broad Balmer lines.

*s060 (O9.7 V):* Possible blend, which hampers the determination of its radial velocity. The target does not show He II 4541, but it presents He II 4200 and He II 4686 in absorption. The relative strength of He II 4200 with respect to He I 4144 indicates an O9.7 type. Due to the broadening of the Balmer series and He II 4686 in absorption, we assign class V. The broad He I lines would be consistent with the source being a blend or an unresolved binary.

*s061 (B0 I):* The spectrum presents a deep depression at  $4320 \text{ \AA}$  due to a defect in the CCD. The star seems to have N and O.

*s063 (B0 III):* Si IV 4089 is affected by an artefact and therefore cannot be used for classification. Since there are no He II lines except for He II 4686, and Si III 4552 is very weak, type B0 is assigned. The relative He II 4686 to He I 4713 line ratio indicates luminosity class III.

*s064 (B0 III):* This star was observed in two runs, MOS2 and LSS3, where no radial velocity variations were detected. We discarded the combination of the observations and used only the MOS2 observation since we did not find S/N improvement in the co-addition. In this observing run, the star was observed in a very short slit, and sky subtraction was compromised. The wavelength of the core of the Balmer lines and the strongest He I lines is consistent with the systemic velocity of the galaxy ( $v_{\text{rad}} = 325 \text{ km s}^{-1}$ ). An instrumental defect at  $\sim 4700 \text{ \AA}$  prevents any conclusion on He II 4686 and He I 4713. There could be a second component at  $v_{\text{rad}} \sim 625 \text{ km s}^{-1}$  showing Si III 4552 and He II 4541.

*s065 (B0 V):* The wings of the Balmer series are abnormally broad, hinting it may be a binary star. The component with the quoted  $v_{\text{rad}} \approx 100 \text{ km s}^{-1}$  would be consistent with the blue wing of the Balmer lines and would show He I lines, but no metallic lines. We note the detection of He I 4471 and Mg II 4481 is hampered by artefacts. We tentatively classify this star as a B0 V. A second component with  $v_{\text{rad}} \approx 700 \text{ km s}^{-1}$  would be consistent with the red wing of the Balmer lines and Si III 4552. The emissions lines at  $\sim 4230 \text{ \AA}$  and  $\sim 4480 \text{ \AA}$  are reminiscent of the Be star VFTS 822 from Evans et al. (2015).

*s068 (B0.5 I):* This source is a blend of two stars, as revealed by HST photometry (Bianchi et al. 2012). It was observed in two consecutive nights with observations separated 19 hours. The spectra are very different, so we treated them as different stars (s068 and s093). This component is consistent with  $v_{\text{rad}} \approx 0 \text{ km s}^{-1}$  and spectral type B0.5 I because of the absence of Mg II 4481 and the relative strength of Si III 4552 with respect to He I 4387. We note the abnormally broad Balmer wings that can be caused by the blend.

*s069 (B0.5 II + O?):* This star was observed in the LSS3 and MOS2 runs, and no radial velocity variations were detected. The co-addition of the spectra do not improve the S/N, so we only use the MOS2 observation. The detection of Si III 4552 and the strength of the He I lines suggest B0.5 spectral type, although the possible presence of He II 4200, He II 4541 and N V 4603, 4620 hints an early-O component at roughly the same  $v_{\text{rad}}$ .

*s070 (B0.5 III):* This star is OB524 from Camacho et al. (2016) and it was also observed within a tilted slit of MOS1 and in the LSS3 run. We obtained a deeper, higher-resolution spectrum in the LSS3 observing run, which will be used from now on. No significant radial velocity variations have been detected, although the MOS1 spectrum could show Mg II 4481. We reclassified the star from B0 to B0.5. Lines He II 4200 and He II 5411 exhibit abnormal profiles and were discarded for the classification.

*s071 (B1 I):* This source was observed in MOS1 and LSS3 observing runs. We detected a radial velocity variation of  $\sim 100 \text{ km s}^{-1}$ , indicative of an SB1 system. The poor S/N of the LSS3 data prevented us from co-adding the spectra, and we only use the MOS1 observation. In this observing run, the star was observed in a slit tilted  $49^\circ$  from the North-South axis, which translates into decreased spectral resolution. If all the spectra of this source are co-added, the He and Si lines show an additional absorption at the blue part of the line core. Therefore, we applied radial velocity shifts to the individual OBs used, aligning them with respect to He I 4471.

*s072 (B1 I):* This source was observed in three observing runs, MOS1, MOS2 and LSS1 (here as OB421 in Camacho et al. (2016)). We detect radial velocity variations of  $\leq 60 \text{ km s}^{-1}$  between runs and between the observing blocks of the MOS1 run, executed more spread over time than the MOS2 and LSS1. We do not find spectral type variations between observations, hence we mark the source as an SB1 candidate.

Since this source was brighter, we used a  $0.63''$  slit in MOS2. However, we could not benefit from the increased spectral resolution due to the comparatively poorer S/N, and we convolved the spectrum to a lower resolution. The poorer S/N could be due to the very short slitlet that, together with a bad column artefact on the right, may have led to problematic nebular subtraction. We co-added the data shifting the spectra to the restframe velocity (adopting the  $v_{\text{rad}}$  of the MOS2 spectra).

The deep depression at  $\sim 4200 \text{ \AA}$  is due to a defect in the CCD. It is detected in both MOS1 and MOS2 observing runs since the star was observed in the same position of the CCD (MOS1 and MOS2 use the same pre-imaging). It is remarkably rich in oxygen based on the strength of O II 4651, considering the star is in the outskirts and far from all the regions of active star formation.

*s073 (B1 I):* The lack of He II lines and the presence of only weak Si III 4552 points to a B1 type. The width of the Balmer series suggests a supergiant luminosity class.

*s075 (B1 I + O?):* The spectrum shows lines at different radial velocities and very broad Balmer wings. At  $v_{\text{rad}} \sim 200 \text{ km s}^{-1}$ , He I 4471, Si IV 4089 and Mg II 4481 are detected and indicate type B1. Luminosity class I is assigned based on the Si IV 4089/He I 4121 ratio. The broad Balmer wings suggest a second component at  $v_{\text{rad}} \sim 500 \text{ km s}^{-1}$ , which would be consistent with He II 4200 and He II 4686 lines. However, we cannot discard the star has luminosity class III at this S/N.



*s076 (B1 I):* We note the anomalous profile of He I 4471, which may be due to unknown nebular overabundance or the low S/N of the spectrum. The lack of Mg II 4481 and Si IV 4089 points to a B1 type. Since the Si III 4552 is weaker than He I 4388, we classify this star as a supergiant. In addition, we expect some contamination from the nearby star, .

*s077 (B1 III):* This source was observed in two observing runs, LSS1 and LSS3, and we detected a possible radial velocity variation of  $50 \text{ km s}^{-1}$ . The poorer S/N of the LSS3 observation prevented us from co-adding both spectra. HST-WFPC2-F555W images reveal the source is a blend.

*s078 (B1 III):* This star was observed in two observing runs, MOS2 and LSS3, where no radial velocity variations were detected. We do not combine the data since we do not find S/N improvements and use only the observation of the MOS2 run. In this observing run, there is a nearby red star that should be blocked by the mask. We discard that the absorption at  $4486 \text{ \AA}$  is caused by Mg II 4481.

*s079 (B1 III):* Spectrum of two unresolved stars that may be causing inconsistencies in the measurement of the radial velocity. At the systemic radial velocity of the galaxy, we observe He I lines and strong Si III 4552, but no Si IV 4089, Si II 4128 or Mg II 4481, hence we assign B1 type. The relative strength of He I 4387 and Si III 4552 points to luminosity class III.

*s080 (B1 III):* The lack of Si II 4129 and Mg II 4481 suggests it is a B1. We assign class III, although this is inconsistent with the abnormally broad wings of H $\beta$ . We expect some contamination from the nearby stars s142 and s121.

*s081 (B1 V):* This source is a blend of two unresolved stars, which may explain the broad Balmer series profiles. Although the extraction failed to resolve the blend, we classify the dominant component as B1 due to the presence of Si III 4552 and the strong He I lines. Luminosity class V is assigned based on the relative strength of Si III 4552 with He I 4388.

*s082 (B1.5 I):* The star was observed in a very short slitlet, and the selection of the sky-box for *apall* subtraction was further hindered by the bad-column artefact from the neighbouring slit hosting star s066. For the second night, the subtraction of a sky-slit was preferred. There is an artificial emission at  $\sim 4350 \text{ \AA}$ . The star could show O II absorption lines (see e.g. red wing of H $\gamma$ ).

*s083 (B2 I):* This source was observed in the LSS1 observing run, corresponding to OB222 in Camacho et al. (2016)'s catalogue, and in the LSS3 run on the night of the 17th of January of 2021. Between the two observations, we detected a significant radial velocity variation of  $115 \text{ km s}^{-1}$ , but no difference in its spectral features, which indicates an SB1 system. We co-added the spectra after correcting the radial velocity variation to achieve higher S/N. We reclassify the target from B1 to B2 because of the strength of Mg II 4481 and Si II 4128.

*s084 (B2 I):* The weak Mg II 4481 and the relative strength of Si II 4128 with respect to Si III 4552 and He I 4121 suggests a B2 type.

*s085 (B2 I):* This source was observed in the LSS1 observing

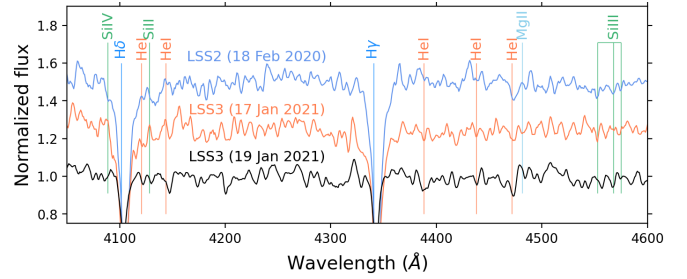


**Figure C2.** Observations of source s086 on three different dates. We measure radial velocity shifts of  $100 \text{ km s}^{-1}$  for the spectrum taken on the night of 17 January 2021 (in orange) and  $50 \text{ km s}^{-1}$  for the one taken on 19 January 2021 (in black) with respect to the observation of 18 February 2020 (in blue), which points to an SB1.

run, corresponding to OB222 in Camacho et al. (2016)'s catalogue, and in the LSS3 run on the night of the 17th of January of 2021. Between the two observations, we detected a significant radial velocity variation of  $115 \text{ km s}^{-1}$ , but no difference in its spectral features, which indicates an SB1 system. We co-added the spectra after correcting the radial velocity variation to achieve higher S/N. We reclassify the target from B1 to B2 because of the strength of Mg II 4481 and Si II 4128.

*s086 (B2 III):* This source was observed in the LSS2 observing run and in two nights of the LSS3 run. We find consistent radial velocities variations of  $\sim 100 \text{ km s}^{-1}$  between the LSS2 spectrum (18 February 2020) and the LSS3 observation of the night of 17 January 2021. However, the LSS3 spectrum of 19 January 2021 shows a radial velocity different by  $\sim 50 \text{ km s}^{-1}$ , suggestive of an SB1 system. We shifted all of them to the restframe velocity and co-added the spectra, shown in Figure C2.

Si III 4552, He I 4471 and other He I lines are present. There could be some Mg II 4481 which, together with its relative strength compared with Si III, indicates B2. We assigned class III based on the width of the Balmer lines, although we note that the existence of a second component could also contribute to a broader profile.

*s087 (B2 III + O?):* This source is a blend, as revealed by HST imaging. The relative strength of He I 4471 and Mg II 4481 points to a B2 type. We tentatively assign class III because of the broad wings of the Balmer lines. However, this broadening could also be explained by a nearby O dwarf, which would also contribute the He II 4200 and He II 5411 lines to the blended spectrum.

*s088 (B2 III + O?):* The star is classified as B2 because of the presence of Si III 4552 and the ratio of He I 4471 and He I 4387. We note that the He I lines are broad and consistent with a second component at  $v_{\text{rad}} \sim 100 \text{ km s}^{-1}$  which could also show He II 4200. Because of the broad Balmer wings and faint absolute magnitude ( $M_V = -3.987 \text{ mag}$ ), we assign class III.

*s089 (B2.5 I):* This star was observed with a slit tilted by  $-25^\circ$  from the North-South axis, which translates into poorer spectral resolution. We reclassify the star with respect to Camacho et al. (2016) from a B0 type to a B2.5 type due to the ratios of Mg II 4481/Si III 4552 and Si III 4552/Si II 4128, and marked it as a binary candidate due to this change in spectral features. We assign class I based on the wings of the Balmer lines, and its absolute magnitude ( $M_V = -6.430 \text{ mag}$ ) is consistent.

*s090 (B2.5 I):* This source is a blend of two unresolved stars. B2.5 spectral type is assigned based on the relative strength of He I 4471 with Mg II 4481. We note the He I lines are abnormally weak.

*s091 (B2.5 I):* The star was observed in two observing runs, LSS1 and LSS3, where no radial velocity variations were detected. The poorer S/N of the LSS3 observation prevented us from co-adding both spectra.

*s092 (B2.5 I):* Its spectrum only displays clear lines of He I and the Balmer series. Although Si III 4552 and Mg II 4481 are very weak, their relative line strength implies a B2.5 type. Lacking indicators for luminosity class, since the Balmer lines seem heavily contaminated by nebular oversubtraction, we assign class I based on its absolute magnitude ( $M_V = -5.714$  mag).

*s093 (B2.5 I):* This source is a blend of two stars, as revealed by HST photometry. It was observed in two consecutive nights with observations separated 19 hours. The spectra are very different, so we treated them as different stars (s068 and s093). This observation is consistent with a B2.5 supergiant and a radial velocity of 450 km s<sup>-1</sup>. We note the abnormally broad Balmer wings that can be caused by the blend.

*s094 (B2.5 I + O?):* The Balmer series and He I lines are consistent with the restframe velocity of the galaxy and we classify the main component as B2.5 I. However, He II lines are tentatively detected at  $v_{\text{rad}} = 650$  km s<sup>-1</sup>. This component could also show N V and N III lines. Therefore, we mark the source as a possible binary.

*s095 (B2.5 III):* We classify this star as a B2.5 type due to the presence of Mg II 4481 and its relative strength with respect to Si III 4552. We assign luminosity class III due to the width of the Balmer lines.

*s096 (B2.5 III):* Noisy spectrum showing the Balmer series. The relative strength of Mg II 4481 and Si III 4552 suggests B2.5 type. Due to the width of the Balmer lines, we assign luminosity class III.

*s097 (B3 I):* We classify the star as B3 supergiant based on the relative strength of He I 4471 and Mg II 4481, and the width of the wings of the Balmer lines. We note that no Si lines are detected in the spectrum.

*s098 (B3 I):* This star presents Mg II 4481 and Si III 4552. The relative strength of Si III 4552 with Mg II 4481 is consistent with a B3 type.

*s099 (B3 I):* The left wing of H $\delta$  is affected by an artefact that prevents using Si IV 4089 for spectral classification. No lines of Si III, or He II are seen. We assign B3 because of the absence of Si III 4552 and the relative strength of Mg II 4481 and He I 4471. Lacking indicators for luminosity class, since the Balmer lines seem affected by nebular oversubtraction, we assign class I based on the absolute magnitude.

*s100 (B3 III):* The spectrum shows the Balmer series, He I lines, and no clear Si or He II lines. Type B3 was assigned based on the Mg II 4481/He I 4471 ratio. The luminosity class is assigned based on the width of Balmer lines.

*s101 (B3 III):* Its spectrum only displays clear lines of He I, Mg II and the Balmer series. We classify this star as a B3 giant based on the relative strength of He I 4471 with respect to Mg II 4481 and the width of its Balmer lines.

*s102 (B7 I):* We classify the star as B7 because of the relative strength of Mg II 4481 with respect to He I 4471 and Si II 4128 with He I 4121. Due to the width of the Balmer lines, we assign a supergiant luminosity class, which is consistent with its apparent magnitude.

*s103 (B7 I):* This source is a blend of two identified stars in [Bianchi et al. \(2012\)](#).

*s104 (B7 I + O?):* The *apall* extraction indicated that the star could be a blend. The relative strengths of Si II 4128 with He I 4121 and of Mg II 4481 with He I 4471 indicate a B7 type. The spectrum also shows He II 4541 consistent with a secondary component.

*s105 (B7 I):* This object was observed in LSS3 and off-slit LSS2. We did not register radial velocity variations and decided to use only the LSS3 observation since no S/N improvement was achieved in the co-addition. The most prominent spectral features are the Balmer series, He I 4026, and He I 4471, although their profiles are dominated by the oversubtracted nebular components. On the other hand, He I 4144 and He I 4920 seem to be mostly stellar. We classify the star as B7 supergiant based on the relative strength of Mg II 4481 and He I 4471.

*s106 (B7 II):* The source was observed in the LSS1 run with a radial velocity of  $\sim 335$  km s<sup>-1</sup>. It was also included in the LSS3 run where we register a different radial velocity of  $\sim 250$  km s<sup>-1</sup> thus we marked it as SB1. We keep the latter spectrum, because of the better S/N and reclassify the target as B7 II. In addition, HST photometry reveals the source is a blend of two stars.

*s107 (B7 III):* The strong absorption of the Si II 4128 and the relative strength of He I 4471 and Mg II 4481 suggest a B7 type. We note, however, there are some radial velocity inconsistencies. We assigned class III based on the broadening of the Balmer lines.

*s108 (B7 III + B?):* This star was observed in the LSS2 run and in 2 observing blocks of LSS3, no significant velocity variation was detected. Only the spectrum with the highest S/N was used (LSS3). Spectral type B7 was assigned based on the relative strength of Mg II 4481 with respect to He I 4471. The width of the Balmer lines suggests class III. There could be a second component at  $v_{\text{rad}} \sim 450$  km s<sup>-1</sup> showing Si III 4552.

*s109 (B7 III + O?):* The source is classified as B7 based on the relative strength of He I 4121 with respect to Si II 4128 and the ratio of Mg II 4481 to He I 4471. The broad Balmer lines suggest a giant luminosity class. The spectrum shows strong He II 5411 and possibly He II 4686 in absorption, hence we mark it as an SB2 candidate.

*s110 (B8 I):* The relative strengths of Si II 4128 with He I 4121 and of Mg II 4481 with He I 4471 indicate a B8 type.

*s111 (B8 II):* [Camacho et al. \(2016\)](#) proposed that the absolute magnitude of this star suggests it may be a central star of a



planetary nebula (CSPN) still in a low-excitation phase.

*s112 (B8 III)*: The equal depth of Mg II 4481 and He I 4471 points to a B8 type. The broad Balmer lines signal a giant luminosity class.

*s113 (B8 III)*: Noisy spectrum. The strong presence of Si II 4128 and the similar depths of Mg II 4481 and He I 4471, along with a broad Balmer series, indicate a B8 giant.

*s114 (B8 III)*: The source is classified as B8 based on the relative strength of He I 4471 to Mg II 4481.

*s115 (B9 I)*: Since the Mg II 4481 line is strong, and He I lines are weak but present, we classify this star as a B9. The luminosity class is assigned based on the width of its Balmer lines.

*s117 (B9 III)*: Due to the relative strength of the Mg II 4481 with He I 4471 lines and the broad Balmer series, we classify this star as a B9 giant.

*s118 (B9 V)*: The spectrum is very noisy. We classify it as B9 due to the detection of Mg II 4481 and Si II 4128. The broad Balmer wings suggest class V, although we note this is inconsistent with the observed  $V = 21.98$  magnitude.

*s120 (A2 I)*: We detect Fe II and Si II lines slightly stronger than the A0 II star s119 (see also Hosek et al. (2014)) and we assign an A2 type. The star is classified as a supergiant because of its absolute magnitude ( $M_V \sim -6.5$  mag). The star was observed in the first two observing nights of LSS3 and no radial velocity variations are detected.

*s121 (A2 I)*: We detect Fe II lines and Si II lines consistent with s120, hence we classify it as A2 I type.

*s122 (A2 I)*: Similar spectrum to s121.

*s123 (A2 III)*: Noisy spectrum. Classified as A2 based on resemblance to star s120.

*s124 (F5 I)*: This star was observed in two observing runs, LSS1 (as OB621) and LSS3. We did not detect radial velocity variations, and we co-added the spectra to increase the S/N. The star is also included in Kaufer et al. (2004)'s catalogue where they classify the star as an F hypergiant.

*s167 (G5 I)*: This star is identified as Sextans A 6 in Britavskiy et al. (2019), where it was classified as late G – early K I. It is located in region–B, where ionized hydrogen is abundant, and the Balmer lines show sky over subtraction in our spectrum. The radial velocity and absence of parallaxes and proper motions of the star further support that the star belongs to Sextans A. We reclassified the star as G5 I based on the relative strength of the  $G$ -band compared to Fe I 4325.

*s168 (G8 I + B7 I)*: At the time of spectral extraction, we noticed that the FWHM of the source was wider than the PSF of the instrument, which suggests the source may be a blend. This is actually seen in the observed spectrum. At  $\lambda > 4800 \text{ \AA}$ , the spectrum is consistent with a G8 I. At bluer wavelengths, the spectrum displays strong lines of Si II 4128 and Mg II 4481 at  $v_{\text{rad}} = 250 \text{ km s}^{-1}$ , and their relative strength with He I 4121 and He I 4471, respectively, points a B7 type.

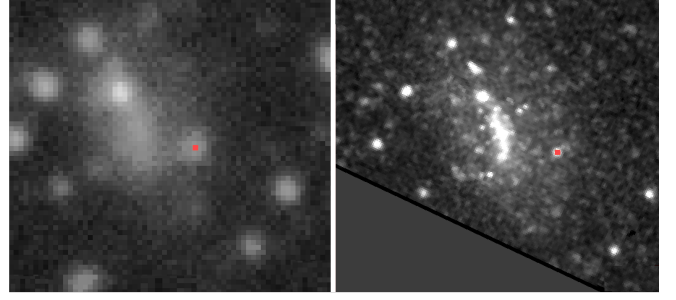


**Figure C3.** Images in the  $V$ -band by Massey et al. (2007) (left panel) and HST-WFPC2-F555W-band from Proposal ID 5915, Cycle 5, PI E. Skillman (right panel). The red square marks the location of s127.

*s169 (G8 I)*: This star is identified as Sextans A 4 in Britavskiy et al. (2019), where it was classified as K1-3 I. It is located in region–B, where ionized hydrogen is abundant, and Balmer lines show sky over subtraction in our spectrum. Its radial velocity and lack of parallaxes and proper motions further support the star belongs to Sextans A. We reclassified the star as G8 I based on the relative strength of the  $G$ -band compared to Fe I 4325.

*s172 (K5 III)*: This star is located in region–B, where ionized hydrogen is abundant. The presence of nebular emission lines and the radial velocity of the star supports that the star belongs to Sextans A. The star is classified as K5 III based on the strength of the  $G$ -band, although we note that H $\gamma$  can not be used for comparison because it is filled with nebular emission.

*s173 (K7 V)*: The extreme flux loss at  $\lambda > 5000 \text{ \AA}$  is likely due to the star being slightly off-slit.

## C2 O stars

Here we report stars for which He II lines are detected.

*s126 (O V)*: HST photometry reveals the source is a blend of three unresolved stars identified in Bianchi et al. (2012). The tentative presence of N V 4603, N V 4620 and C IV 4441 would correspond to an O2 type (see e.g. star 30 Dor/P871 in Walborn et al. (2002)). However, we note the weak emission of He II 4686 and the absence of He II 4541, which may be due to nebular contamination. On the other hand, He II 4200 displays strong emission, unseen in typical spectra of early O stars. We assign luminosity class V because of the broad Balmer lines, although this is in contradiction with He II 4686 in emission or filled.

*s127 (O V + gal)*: This star overlaps with the projection of a background galaxy, which may explain why its colours are not compatible with the adopted spectral type. HST imaging is consistent with this source being a star from Sextans A (see Fig. C3).

The spectrum shows high S/N, although He II lines are weak (which may be caused by the continuum dilution by the background galaxy) and He I lines are absent due to nebular contamination. Class V is assigned based on the width of the Balmer lines, although we note the absence of He II 4686, which should exhibit strong absorption at this class.

*s128 (O V)*: This star is very faint and was not registered

by Massey et al. (2007)’s catalogue, although Bianchi et al. (2012)’s HST catalogue provides a source in that location with  $V = 22.67$  mag.  $H\beta$  and  $H\gamma$  are strong in absorption, and there are absorption features at the expected location of He II 4200 and He II 4541. The latter would be stronger than He I 4471. Therefore we classify the star as a potential O dwarf.

*s129 (O V + neb)*: Noisy spectrum dominated by nebular features. The only He lines unambiguously detected are He II 4200, He II 5411 and He II 4922. The relative strength of these features suggests a mid- to early-O type star. Considering the visual magnitude of the star, we assign a conservative O V classification, although we note the narrow, nebular over-subtracted Balmer lines.

*s132 (O V + neb)*: The spectrum shows very poor S/N resulting from the off-slit allocation of this  $V = 21.35$  mag star. It is dominated by nebular emission lines. Yet, it shows some absorption features. The radial velocity was estimated from He II 4686. Other absorption features, most notably He II 4200, concur with this radial velocity.

*s133 (O + neb)*: This star was observed in a very short slit that prevented the use of local sky boxes for sky subtraction with *apall*. We used the sky spectrum from the sky slits, which resulted in the loss of the extremes of the spectral range. He II 4200 and He II 4686 are strong. He II 4541 is not detected but could be filled by nebular emission. We note that the He II lines, and also He I 4471 are broad as well. This star is far from the optical centre of the galaxy and the most prominent diagnostics of star formation.

*s134 (O V)*: Very noisy spectrum. We detected the Balmer series and tentatively the He I lines and He II 4686. There may be contamination from a nearby star. There is an unknown emission at 4403 Å.

*s135 (O V)*: The spectrum might present possible contamination from the adjacent stars in the slit, and s043. There is a strong He II 4541 line, although it shows inconsistent radial velocity.

*s136 (O + neb)*: We classify this star as O based on the He I lines and He II 4686 in absorption.

### C3 B stars

Here we report stars for which He I lines are detected.

*s137 (Be + O?)*: This spectrum displays strong emission at  $H\beta$ ,  $H\gamma$  and  $H\delta$ . The star is located far from the H II-rich regions, and  $H\gamma$  and  $H\beta$  are wider than the expected width of nebular lines, suggesting a stellar origin. The Balmer series and He I lines are consistent with the systemic radial velocity of the galaxy. There may be a secondary component showing He II and Si lines at 0 km s<sup>-1</sup>.

*s138 (B III + gal)*: This source spatially overlaps a background galaxy (see Fig. C4), which contributes to its total flux (see e. g. redshifted lines of  $H\beta$  and [O III]). The shown spectrum exhibits stellar Balmer lines and very weak He I lines, probably due to the dilution of the stellar flux. We classify the star as a B giant based on the width of the Balmer lines.

The target was observed in two different nights within the LSS3 run. The spectra of the second night were discarded since they were taken at worse seeing conditions and suffer from a larger contribution of

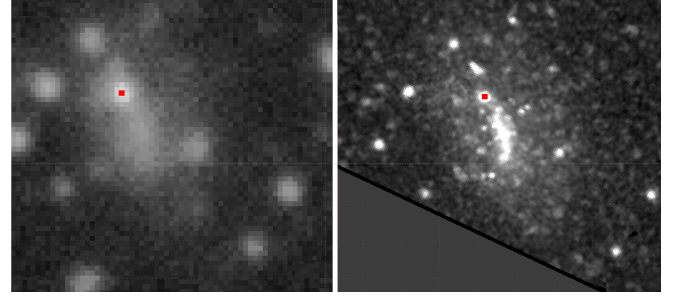


**Figure C4.** Images in the V-band by Massey et al. (2007) (left panel) and HST-WFPC2-F555W-band from Proposal ID 5915, Cycle 5, PI E. Skillman (right panel). The red square marks the location of s138.

the background galaxy. We note, however, that we detect a radial velocity variation at the Balmer lines of  $\sim 150$  km s<sup>-1</sup> between nights.

*s139 (B + O?)*: The extremely broad Balmer lines, together with a tentative detection of He II lines at  $v_{\text{rad}} \sim 400$  km s<sup>-1</sup> suggest a possible O-type component.

*s140 (B III)*: Off-slit star. He I 4471 and other He I lines are clearly detected. Si III 4552 could be present. Luminosity class III is assigned as a trade-off between the width of the Balmer lines and its visual V magnitude.

*s141 (B)*: Faint star, not intended in the survey, and off-slit. Its trace is lost at red wavelengths ( $\lambda > 5300$  Å) during the extraction.

*s144 (B)*: Very faint ( $V = 21.535$  mag), off-slit star. Balmer lines show broader wings with cores affected by nebular oversubtraction. Some He I lines and possibly Si III 4552 are detected.

*s145 (B)*: Very noisy spectrum. Balmer lines and some He I lines are detected. There may be contamination from a nearby star.

*s146 (B)*: Very noisy spectrum, only the Balmer series, Si II and some lines of He I are detected.

*s147 (B)*: Very noisy spectrum. The Balmer series is detected, together with some He I lines, and perhaps Si II 4128 and Mg II 4481.

### C4 OB stars

Here we report stars for which He I lines and tentatively He II lines are detected.

*s148 (OB)*: The spectrum could show He II 4200 and broad lines of He I 4387 and He I 4920.

*s150 (OB)*: The spectrum may show He II 4541.

*s151 (OB)*: This spectrum is a blend of three unresolved stars.

*s152 (OB)*: Balmer lines, some He I lines and perhaps He II 4200 are detected. There may be contamination from a nearby star.

*s154 (OB)*: We clearly detect the Balmer series, some He I lines and perhaps He II 4541.

*s156 (OB)*: This star is very faint and it was not registered by Massey's catalogue, although Bianchi et al. (2012)'s HST catalogue provide  $V = 22.18$  mag. Its spectral S/N is poor as expected for such a faint star.

The Balmer lines seem to be relatively broad with the core affected by nebular oversubtraction, which would be offset in the  $v_{\text{rad}}$  space from the broader stellar component. The radial velocity differs by  $\sim 200 \text{ km s}^{-1}$  from the galaxy's systemic velocity, but after this correction we detect He I lines at their restframe wavelengths. He II 4541 is not detected but He II 4200 is. On the other hand, there is no clear Si III 4552 but there seem to be Si absorption by the wings of H $\delta$ .

## C5 OBA stars

Here we report stars for which only the Balmer series is clearly observed.

*s158 (OBA)*: This star was observed within a slit tilted  $8^\circ$  to include also star s031. The inclination results in degraded spectral resolution. The signal to noise ratio is extremely poor.

*s159 (OBA)*: This source is a blend of two unresolved stars based on HST photometry.

*s161 (OBA)*: Noisy spectrum with strong nebular contamination. Only H $\delta$  is clearly detected.

*s162 (OBA)*: There may be contamination from a nearby star.

*s163 (OBA)*: There may be contamination from a nearby star.

*s165 (OBA)*: We assigned the systemic velocity of the galaxy.

This paper has been typeset from a  $\text{\LaTeX}$  file prepared by the author.